공학박사 학위논문

# Advanced segmentation algorithms using numerical model and graph theory

– Application to the lung images–

# 수치 모델과 그래프 이론을 이용한 향상된 영상 분할 연구

–폐 영상에 응용–

2016 년 2 월

서울대학교 대학원

협동과정 바이오엔지니어링 전공

배장표

A thesis of the Degree of Doctor of Philosophy

# 수치 모델과 그래프 이론을 이용한 향상된 영상 분할 연구

– 폐 영상에 응용–

# Advanced segmentation algorithms using numerical model and graph theory

– Application to the lung images–

February 2016

Interdisciplinary Program for Bioengineering
Graduate School,
Seoul National University
Jang PyoBae

# Advanced segmentation algorithms using numerical model and graph theory

by
Jang PyoBae

This Dissertation is approved for the Degree of Doctor Philosophy in Interdisciplinary Program for Bioengineering Graduate School at Seoul National University

February 2016

Approved by Thesis Committee:

Professor Jin Mo Goo Chairman
Professor Hee Chan Kim Vice chairman
Professor Namkug Kim
Professor Jaesoon Choi
Professor Jung Chan Lee

# ABSTRACT

This dissertation presents a thoracic cavity segmentation algorithm and a method of pulmonary artery and vein decomposition from volumetric chest CT, and evaluates their performances. The main contribution of this research is to develop an automated algorithm for segmentation of the clinically meaningful organ. Although there are several methods to improve the organ segmentation accuracy such as the morphological method based on threshold algorithm or the object selection method based on the connectivity information our novel algorithm uses numerical algorithms and graph theory which came from the computer engineering field. This dissertation presents a new method through the following two examples and evaluates the results of the method.

The first study aimed at the thoracic cavity segmentation. The thoracic cavity is the organ enclosed by the thoracic wall and the diaphragm surface. The thoracic wall has no clear boundary. Moreover since the diaphragm is the thin surface, this organ might have lost parts of its surface in the chest CT. As the previous researches, a method which found

the mediastinum on the 2D axial view was reported, and a thoracic wall extraction method and several diaphragm segmentation methods were also informed independently. But the thoracic cavity volume segmentation method was proposed in this thesis for the first time. In terms of thoracic cavity volumetry, the mean±SD volumetric overlap ratio (VOR), false positive ratio on VOR (FPRV), and false negative ratio on VOR (FNRV) of the proposed method were 98.17±0.84%, 0.49±0.23%, and 1.34±0.83%, respectively. The proposed semi-automatic thoracic cavity segmentation method, which extracts multiple organs (namely, the rib, thoracic wall, diaphragm, and heart), performed with high accuracy and may be useful for clinical purposes.

The second study proposed a method to decompose the pulmonary vessel into vessel subtrees for separation of the artery and vein. The volume images of the separated artery and vein could be used for a simulation support data in the lung cancer. Although a clinician could perform the separation in his imagination, and separate the vessel into the artery and vein in the manual, an automatic separation method is the better method than other methods. In the previous semi-automatic

method, root marking of 30 to 40 points was needed while tracing vessels under 2D slice view, and this procedure needed approximately an hour and a half. After optimization of the feature value set, the accuracy of the arterial and venous decomposition was 89.71 ± 3.76% in comparison with the gold standard. This framework could be clinically useful for studies on the effects of the pulmonary arteries and veins on lung diseases.

---

**Keywords:** chronic obstructive pulmonary disease (COPD), computed tomography, multi-organ segmentation, thoracic cavity, pulmonary artery and vein decomposition, two level minimum spanning tree constructions

**Student number:** 2010-30263

# CONTENTS

# LIST OF TABLES

## Chapter 1



## Chapter 2



## Chapter 3

# LIST OF FIGURES

## Chapter 2



## Chapter 3

# CHAPTER 1

# General Introduction

## 1.1 Image Informatics using Open Source

The concept of Open Source software (OSS) promotes the development and sharing of software source code under special licensing agreements that protects author's copyrights while maintaining the distribution of free and open derivative work based on the original code. The most successful example is Linux operating system.

Numerous Open Source initiatives in medicine leading to innovate and cost effective information systems supporting electronic patient record applications and medical imaging and PACS have emerged in the recent years. Recent reports showed that adoption of computerized medical records and medical informatics in medicine have significantly lagged behind expectations due to three major barriers: excessive cost, the transience of vendors, and the lack of command standards and adequate models many authors suggested. However Open Source software reduces these barriers by reducing ownership and development costs and facilitating the adaptation of customized tools for clinical practice[1].

The impact of open source is even greater in specialized areas of medicine such medical imaging[2]. The Visualization Toolkit or VTK[3] is well recognized and widely adopted software library that runs on multiple platforms and has been used for numerous scientific and medical applications so far[4]. The recent adjunction of the Insight Toolkit or ITK[5], mostly funded by the US National Library of Medicine as part of the Visible Human Project, adds a wealth of additional rendering and image processing tools for medical applications.

Quantitative assessment of lung structure along with indices of parenchymal pathology are taking on increased roles in the detection and tracking of pulmonary disease. To date the focus has largely been on airway morphometry and indices of parenchymal destruction, and air trapping. The parenchymal analysis has, in large part, focused on the use of the density histogram within the lung field to identify voxels falling below a given density threshold to define volumes of emphysema-like lung or air trapping. Some work has shown that texture measures can provide more accurate detection and quantification of pathology not limited to enlargement of peripheral air spaces[6]. Based on ITK and self-built in

libraries, MIRL of Asan medical center developed AView solution as quantitative tools for the assessment of the lung parenchyma, and used this solution in a number of large multi-center studies.

## 1.2 History of the segmentation algorithm

In Pre-1980 to 1984, the term "medical image analysis" was not yet in common use. However, a variety of meetings had included work related to the analysis of medical and biomedical images. A particular characteristic of most of the work during these years was that researchers were primarily thinking in terms of analyzing two-dimensional image datasets[7].

In mid-to-late 1980s, to some extent, research in the classic problems of boundary finding, 2D image matching, and ideas related to pattern recognition-driven, and computer-aided diagnosis continued. It is important to note that during the later part of this time frame, deformable models were discovered and then introduced into the field[8]. The concept of scale space theory to the problem was applied in negotiating the segmentation of complex medical image data by the type of scale-space hierarchies of intensity extrema[9]. Image texture

also was pursued as a feature useful for grouping and measurement in image analysis during this period, especially with respect to ultrasound image data[10].

In 1992 to 1998, the analysis of fully 3D images became a key goal and more mathematical-model-driven approaches became computationally feasible. Especially, deformable model methods were now coming into their own for medical applications, as different groups developed fully 3D "snakes" that could be run on volumetric image datasets[11]. In addition, approaches that incorporated shape priors were also extended into 3D, and another line of research pursued by Cootes et al. reported novel ways of introducing priors using point sets[12]. An interesting alternative to objective function-based deformable contours also emerged in this time frame in the name of level set algorithm[13]. Despite the successes noted above, it is fair to say that, as the 1990s draw to a close, no one algorithm can robustly segment a variety of relevant structure in medical images over a range of datasets.

Currently, methods for segmentation of medical images are divided into three generations, where each generation adds an additional level of algorithmic complexity[14]. The first

generation is composed of the simplest forms of image analysis such as the use of intensity thresholds and region growing. The second generation is characterized by the application of uncertainty models and optimization methods, and the third generation incorporates knowledge into the segmentation process. There are so much algorithms of variety technology for segmentation work where specific classification of segmentation algorithms is needed. Table 1-1 shows the classification summary of segmentation algorithms.

TABLE 1-1. Classification model summary

| Generation | Region-based | Boundary Following | Pixel Classification |
|---|---|---|---|
| 1st | •Region growing | •Edge tracing | •Intensity threshold |
| 2nd | •Deformable models<br>•Graph search | •Minimal path<br>•Target tracking<br>•Graph search<br>•Neural networks<br>•Multiresolution | •Statistical pattern recognition<br>•C-means clustering<br>•Neural networks<br>•Multiresolution |
| 3rd | •Shape models<br>•Appearance models | | •Atlas<br>•Rule-based |

| | | | |
|---|---|---|---|
| | •Rule-based<br>•Coupled surfaces | | |

The proposed method for thoracic cavity segmentation corresponds to the Rule-based method of 3rd and region-based method. This method extracts the special surface from the rib information. This extraction comes from the rule that the rib is in the boundary of the thoracic cavity. The pulmonary vascular segmentation and classification of arteries and veins matches to Graph search of 2nd and Region based. As separation using the shortest path algorithm is based on the graph theory, this algorithm corresponds to this category. But since the pulmonary vascular decomposition method uses the graph theory for the application of the interactive program, this algorithm must also be classified as interactive segmentation algorithm.

## 1.3 Goal of Thesis Work

Image segmentation is one of the most interesting and challenging problems in computer vision generally and medical imaging applications specifically. Segmentation partitions an

image area or volume into nonoverlapping, connected regions, which are homogeneous with respect to some signal characteristics. Medical image segmentation is of considerable importance in providing noninvasive information about human body structures that helps radiologists to visualize and study the anatomy of the structures, localize pathologies, track the progress of diseases, and evaluate the need for radiotherapy or surgeries. For these reasons, segmentation is an essential part of any computer-aided diagnosis (CAD) system, and functionality of the system depends heavily on segmentation accuracy. Moreover, this thesis has a further application in the improved imaging biomarker development through the segmentation software development specified on the thoracic region and pulmonary vessels.

Chapter 2 proposed the advanced segmentation algorithm for the thoracic cavity, and Chapter 3 argues the semi-automatic algorithm for decomposition of the artery and vein. These two segmentation methods were based on the volumetric chest CT.

# CHAPTER 2

# Thoracic cavity segmentation algorithm using multi-organ extraction and surface fitting in volumetric CT

## 2.1 INTRODUCTION

The thoracic cavity is the chamber of the human body that is protected by the thoracic wall and includes important organs such as the heart and lung. Quantification of the volumes of various features of the thoracic cavity, especially the amount of regional thoracic fat (fat within the inner thoracic cavity), would be of high clinical value because research over the past two decades shows that this fat may contribute to an unfavorable metabolic and cardiovascular risk profile[15, 16] and chronic obstructive pulmonary disease (COPD)[17]. For example, the levels of thoracic fat, which includes both epicardial and extra-pericardial fat, correlate strongly with pericardial fat levels (typically $r > 0.85$)[18]. Since subcutaneous fat and visceral fat associate with different metabolic risks, this means that the amount of fat in the thoracic cavity may be an important risk factor for heart disease[19]. In addition, muscle amount in the thoracic cavity could be important index for some cardiovascular diseases, because they represent volume of major vessels and heart[1]. In lung disease, the amount of visceral fat associates with low-

grade systemic inflammation, the severity and changes in emphysema and task-related metabolic demands[3,] [20-22]. In patients of COPD, the amount of visceral fat, muscle and calcification together may be a more accurate risk factor than the amount of visceral fat, as only the tissue close to the heart and the lung can be considered. These observations indicate that intra-thoracic tissue composition assessments in patients with COPD may be clinically useful. The presence of calcified plaque in vessel also associates with heart disease and COPD, and inflammation.

However, the fact that the thoracic cavity contains various organs significantly complicates its segmentation. As a result, manual thoracic cavity segmentation is a labor intensive and time-consuming task and inter-observer reliability cannot be guaranteed, especially for longitudinal studies and large-scale screening. To reduce the manual burden and improve reliability, automated computerized methods for segmenting the thoracic cavity region are needed. The present study describes the semi-computerized method that we developed for this purpose. This method involves a multi-organ extraction approach. To ensure that all the tissue inside the inner thoracic

cavity is included in the segmentation, the inner thoracic cavity is modeled by using the inner surface of the ribs. To segment the diaphragm, the diaphragm surface is modeled by using the bottom surfaces of the lung. To further improve the accuracy of diaphragm segmentation, additional segmentations of the heart and its surrounding tissue are performed. In addition, since the accurate extraction of mediastinum tissue is one of our clinical goals, the lung is subtracted from the thoracic cavity for clinical evaluation. In the present study, this proposed thoracic cavity segmentation method was tested in patients with COPD against the gold standard, namely, manual segmentation by two experts that was verified by an expert thoracic radiologist. It was also compared to three state-of-the-art thoracic cavity organ segmentation methods.

## 2.2 RELATED STUDIES

The organs in the thoracic cavity are the rib, lung, heart, and diaphragm. Most of previous studies on thoracic cavity segmentation focus on segmentation of only one of these organs. Moreover, few focus on the volumetric accuracy of the

segmentation. The studies on thoracic cavity segmentation include that by Zhang *et al.*, who proposed a segmentation algorithm of the mediastinum region that involved calculating four marginal points that constructed the mediastinum contour. However, this method did not accurately consider the diaphragm surface[23]. Chittajallu *et al.* proposed an optimal surface-detection method to identify the inner thoracic cavity and the inner points of the rib for the surfaces[24]. Many studies have sought to extract the diaphragm in chest CT[25-27], including the study by Xiangrong *et al.*, who proposed a method to extract the upper surface of the diaphragm[25]. They estimated the position of the diaphragm by deforming a thin-plate model that matched the bottom surface of the lung. Li *et al.* proposed a graphcut-cut method with a multi-column structure that allowed terrain-like surface estimation[28]. Yalamanchili *et al.* used this method to segment the diaphragmand adopted the cost function calculated on the basis of prior conditions to guide the surface into the target location[26]. Rangayyan*et al.* proposed a method for automatically delineating the diaphragm by modeling using the linear least-squares procedure, which extracted the initial

diaphragm model from the voxels of the base of the lungs. In addition, each dome of the diaphragm was modeled as a quadratic surface.

Although most previous studies on heart segmentation focused on segmenting the heart chambers[29], several also studied volumetric whole heart segmentation[30, 31]. Funka-Lea *et al.* proposed an isolation algorithm of the heart that used a particular means of initiating and constraining the graph-cut technique[30]. In the initiating step, an ellipsoid is grown progressively from the entry point to the heart wall. In the energy equation of the graph-cut, the blob constraint is added to make cuts that look like spheres[30]. Zheng *et al.* proposed a heart segmentation method that uses optimal shape initialization. In this method, the optimal mean shape is initialized in the location of the heart. The mean shape is then aligned with the detected pose, followed by boundary refinement using a learning-based boundary detector. That paper insisted that this algorithm is more accurate and faster than the graph-cut based method[31].

Our proposed method is a shape prior level set-based the heart segmentation method. This method uses a sphere as

the shape prior. The initial shape grows while maintaining the shape prior until this shape meets the stopping condition[32].

## 2.3 THE PROPOSED THORACIC CAVITY SEGMENTATION METHOD

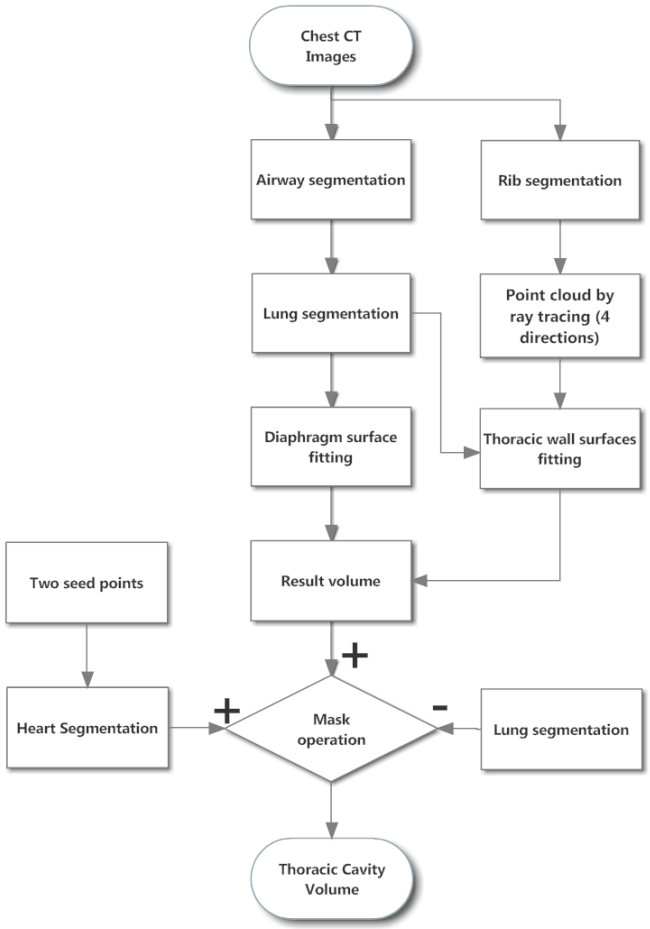


Figure 2-1. Schematic depiction of the steps in the proposed

thoracic cavity segmentation method.

In our method, airway segmentation, lung and heart segmentations and rib detection are performed first. After this, the thoracic cavity region is segmented by finding the five surfaces that enclose the thoracic cavity. The inner thoracic cavity is modeled by four surfaces along different directions from the inner points of the ribs. In addition, the diaphragm surface is approximated by the base voxels of the lung. These five terrain-like surfaces are approximated by a 3-dimensional (3D) surface-fitting method. Supplementary segmentations of the heart and its surrounding tissue are performed to improve the accuracy of diaphragm segmentation. For heart segmentation, two seed points are needed. Figure 2-1 shows a flow chart that schematically depicts our method.

### 2.3.1 Airway and lung segmentation

In our method, airway and lung segmentation are performed by using a thresholding method. The airway region is removed from the lung segment to differentiate the left and right lungs. From the seed point ($SP_1$) that is automatically

marked on the top of the airway region, a seeded region-growing method is performed to search for 3D connected regions below −924 Hounsfield Units (HU). This value was selected empirically on the basis that air is at approximately −1000 HU while soft tissues range of −100 to 200 HU[33]. The $SP_1$ in the airway can be at any point in the airway. Therefore, moving from the top slice to the bottom slice, we search the first slice for exactly three connected components with a specific size. $SP_1$ is determined by the center of inertia of the third largest connected component, because two other connected components would be the left and right lungs. As leakage may have occurred during region growing in airway segmentation, explosion-controlled region growing was performed[34].

In our method, to segment the lung, initial lung segmentation using a threshold value of −474 HU is performed. Previous studies have selected predetermined thresholds that range from −450 to −550 HU[35, 36]. In the present study, −474HU was chosen empirically to be the threshold value on the basis of the characteristics of our chest CT scans. The final lung is generated by subtracting the airway from the initial lung.

To differentiate the right and left lungs, connected components analysis on the final lung region is performed by selecting the two largest connected components. If the lung is not split after removing the airway region, the lung-split algorithm is performed[37]. This algorithm performs iterative eroding until the lung is split. Finally to smooth the lung boundary, the rolling-ball filter implemented by the ITK Toolkit[38] is applied; for this, the radius of the kernel is set to 4.

### 2.3.2 Surface-fitting method

The *gridfit* function, which was developed by using MATLAB R2012a (Mathworks Inc., Natick, MA, USA), is a surface modeling tool that fits a terrain surface (x,y,z) from scattered data[39]. Since the *gridfit* function is an approximant, not an interpolant, it uses the least-squares approximation to calculate the ill-conditioned solution in a linear algebra problem. The problem is described in the following equation:

$$Ax = y \quad (2-1)$$

where the number of data points is *t*, the number of the grid nodes is *s,* A is a $t \times s$ matrix, x is a $s \times 1$ matrix, and y is a $t \times 1$ matrix. x and y are point arrays, and x is an unkown

quantity. Matrix 'A' represents geometric relations between x and y. Four grid nodes constitute a rectangle where the approximation of the z value can be evaluated by a triangle interpolation. However, since the input data points are not evenly distributed, there are only a limited number of rectangles for calculating the z value. To determine the relationship between neighboring grid nodes, the regulator was suggested. In the gradient regulator, the following relationship must be satisfied at an arbitrary rectangle vertex V(x, y):

$$V(x-1,y)-2V(x,y)+V(x+1,\mathrm{y})=0 \quad (2-2)$$

$$V(x,y-1)-2V(x,\mathrm{y})+\mathrm{V}(\mathrm{x},\mathrm{y}-1)=0 \quad (2-3)$$

This relation is expressed by the following equations.

$$Bx=0 \quad (2-4)$$

where B is a $2s\times s$ matrix. Equations (2-1) and (2-4) are combined as follows:

$$\begin{pmatrix} A \\ \lambda B \end{pmatrix} x = Cx = \begin{pmatrix} y \\ 0 \end{pmatrix} \quad (2-5)$$

where $\lambda$ controlls the smoothness of the surface and C is a $(\mathrm{t}+2\mathrm{s})\times \mathrm{s}$ matrix. The solution could be provided by following equation[40].

$$x = \left(C^T C\right)^{-1} C^T \begin{pmatrix} y \\ 0 \end{pmatrix} \quad (2-6)$$

The equation was solved in the meaning of the minimum mean square root method[40].

### 2.3.3 Inner thoracic cavity surfaces

Inner wall of thoracic cavity are modeled by four partial surfaces. These surfaces are fitted by terrain-like surfaces from the point cloud of inner rib voxels. First, ribs were extracted as regions where the pixel intensities were larger than the value of 120 HU. Among the segmented regions, only a largest connected component was selected as the rib region. The sternum or breastbone is a flat bone that lies in the middle front part of the rib cage. As the inaccurate segmentation of the sternum could make the curved horizontal fitting surface in the sternum region, the selection of the threshold was important. In general, HU value of the sternum is slightly lower than the other bone. There was a trade-off between the inclusion of the sternum and the occurrence of the noise in determining HU value.

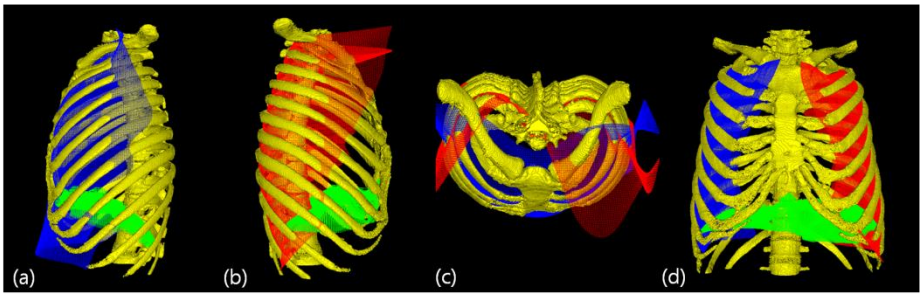


Figure 2-2. Five fitted surfaces. (a) The anterior left thoracic surface (blue), (b) The posterior right thoracic surface (red) (c) The dorsal view of the surfaces of (a) and (b) without the diaphragm (d) The left and right thoracic surfaces (red and blue, respectively) with the diaphragm surface (green)

The inner wall of thoracic cavity is found by anterior-posterior(AP) on the upper and lower ribs and radial ray projection on the left and right ribs[41]. AP rays are projected from the line crossing the centers of the left and right lungs while radial rays are projected from the centers of each half lung. The 3D surface-fitting are the points where the projection rays first touch the rib. To exclude points belonging to different bones such as scapular, the Euclidean distance field from the boundary of the lungs is generated by a volume-based method[42, 43] and the point cloud outside the 20 distance offset is removed.

Four point clouds are converted into terrain-like

surfaces by the *gridfit* algorithm. As described in section III.B, this algorithm approximates the 3D grid points by solving a linear algebra equation with a gradient regulator[39]. The resulting four surfaces are shown in Figure. 2-2. The*gridfit* function with 3mm by 3mm cells is performed and the fitting result is interpolated into the original volume spacing.

### 2.3.4 Diaphragm surface modeling

The diaphragm is a thin and double-domed muscle that separates between the thoracic and abdominal cavities. It is located below the lungs and forms the floor of the thoracic cavity on which the heart and lungs rest[26]. The similar appearance of the organs surrounding the diaphragm and the poor resolution of non-contrast CT scans makes the automatic segmentation of the diaphragm less accurate than inner thoracic cavity surface segmentation.

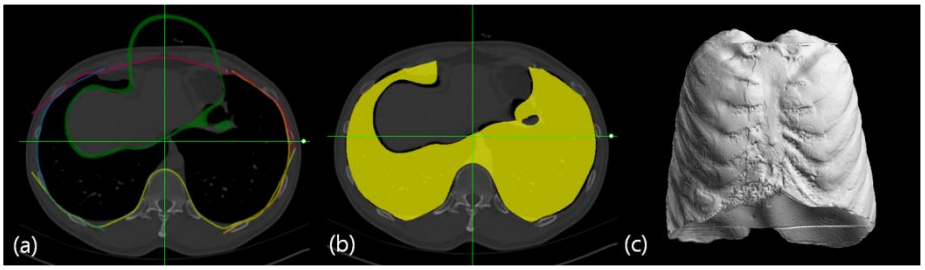


Figure 2-3. Extracting the thoracic cavity volume. (a) Five thoracic surfaces. The surfaces are depicted in red, magenta, light green, and blue, and the diaphragm is depicted in dark green as shown in the legend to FIG. 2-2. (b) Thoracic cavity volume (yellow) (c) Three-Dimensional display of the tissue inside the final thoracic cavity

The lower parts of the lung surfaces could be the initial left and right diaphragmatic surfaces. Zhou *et al.* extracted these diaphragm surfaces by considering the surface normal direction[25]. To calculate the surface normal direction, we must convert the volume into the surface composed of meshes by a marching cube algorithm[44]. Therefore, 3D ray projection from the lower position is easier than extracting the surface normal direction. In our method, the diaphragm surfaces are extracted by the 3D ray projection method from the two centers of the bottom of each lung along the half-sphere direction. The x and y positions of the starting point of ray

projection are calculated from the mass center of each half lung in the axial slice of the lung containing the liver dome. In addition, the z position is selected from the bottom slice containing the lung. The ray projection is performed along the half-sphere. To remove the noise voxels that are not the diaphragm, only the voxels below the liver dome are selected and the connected components whose voxel counts are below 1000 voxels are removed by labeling operator.

The diaphragm surface is located below the heart and above the liver in the central region. Therefore, for 3D surface fitting, the initial left and right diaphragmatic lung surfaces are input point cloud. The *gridfit* function is used for this fitting. Figure 2-3a shows the axial view that contains the inner thoracic cavity surfaces and the diaphragm surface.

In the present study, three state-of-art methods for modeling the thoracic cavity were implemented and compared with our proposed method. The Thin plate spline (TPS) method was developed on the basis of the TPS deformation method of Zhou *et al.*[25]. The base surface of each lung was considered as the diaphragm candidate with which the plate was deformed by using TPS deformation. To find the optimal surface of the

diaphragm segment, Li *et al.* and Yalamanchili *et al.* applied the graph-cut algorithm to the diaphragm segmentation[12, 28]. Finally, the *gridfit* method, as explained in section III.B, approximates the surface between the base surfaces of each lung by using the *gridfit* function. Comparison of the *gridfit* method to our proposed method will show the effect of adding the heart and its surrounding tissue. Since the *gridfit* method yields a similar diaphragm shape as the TPS method, the addition of the heart and its surrounding tissue to the TPS result should improve the segmentation.

### 2.3.5 Heart segmentation

We performed two-stage level set method to extract the heart and the pericardial fat from volumetric chest CT. In the first stage, the heart segmentation was performed by the level set method with a sphere as a shape prior. In the second stage, the surrounding pericardial fat was segmented with shape of the heart as a shape prior which was the segmentation result of the first stage. As pericardial fat is located around the heart, we performed the pericardial segmentation with the boundary of the heart as the starting position. Because the

diaphragm exists between the heart and the liver, the segmentation of the heart and its pericardial fat is needed to enhance diaphragm segmentation result.

In our method, the operator places two manual points on the heart, namely, on the upper and lower points of the heart on the sagittal plane that crosses near the center of the heart. From these seed points, the center ($c_h$) and the estimated radius ($r_e$) of the heart are calculated as follows:

$$c_h = \frac{1}{2}(p_1 + p_2), r_e = \frac{1}{2}(p_1 - p_2) \quad (2-7)$$

where $p_1$ and $p_2$ are the manually selected points. The level set method using a sphere as the shape prior is used to segment the heart. The initial shape for the level set is the sphere that uses the manually predetermined $c_h$ as its center and 0.6* $r_e$ as its radius; it is located on the sagittal plane of the center of the heart. The speed function is based on an edge potential map with user-defined masking to prevent leaking in the following equation[45, 46]:

$$k_I(x, y, z) = \begin{cases} \dfrac{1}{1 + |\nabla G * I(x, y, z)|} & \text{if } I(x, y, z) \geq u \\ 0 \text{ if } I(x, y, z) < u \end{cases} \quad (2-8)$$

where u is set by 0 HU, $k_I$ is a voxel of speed image, and I(x,y,z) is an image voxel. Generally, the user-defined value is set to prevent leakage across the edges.

This shape prior level set method is implemented by modifying the GeodesicActiveContourShapePriorLevelSetImageFilter in ITK Toolkit[38]. This filter adopted the level set method using a shape prior from Leventon *et al.*'s paper[32]. In this algorithm, the function of a shape prior was used to restrict the evolution of the level set surface considering the shape prior. The reason for heart segmentation is enhancement of diaphragm segmentation which would be hard to delineate correct especially below the heart. Compared with original filter implementation, shape and pose prior terms are changed for optimization purpose[32]. The shape prior term was replaced by using a Limited memory Broyden Fletcher Goldfarb Shannon (LBFPS) optimizer. This optimizer can restrict the search space. The pose prior was not used because the shape prior is a sphere[47]. This optimizer had four parameters: the radius, and the x, y and z positions from the center of the heart. The restricted search ranges of the optimizer are as follows: radius

($0.4*r_e$ ~ $1.4*r_e$), and the x, y and z positions from the center of the heart (−10 ~ 10 mm).

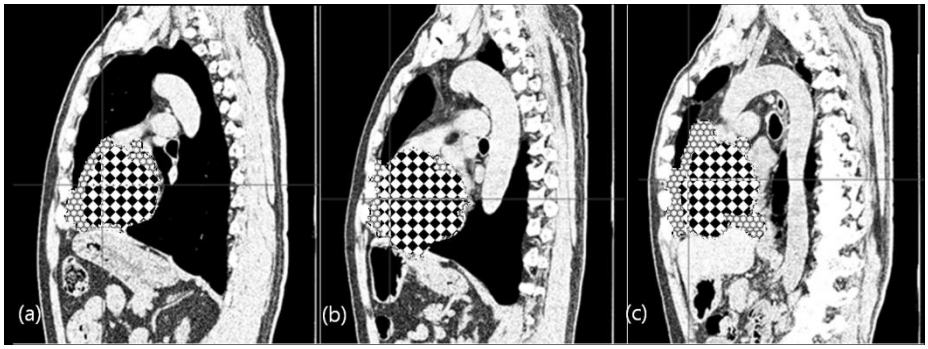


Figure 2−4. Segmentation of the heart and its surrounding tissue. (a−c) The result of segmentation of the heart and the surrounding tissue in three adjacent three sagittal planes. The heart is red and the surrounding tissue is blue.

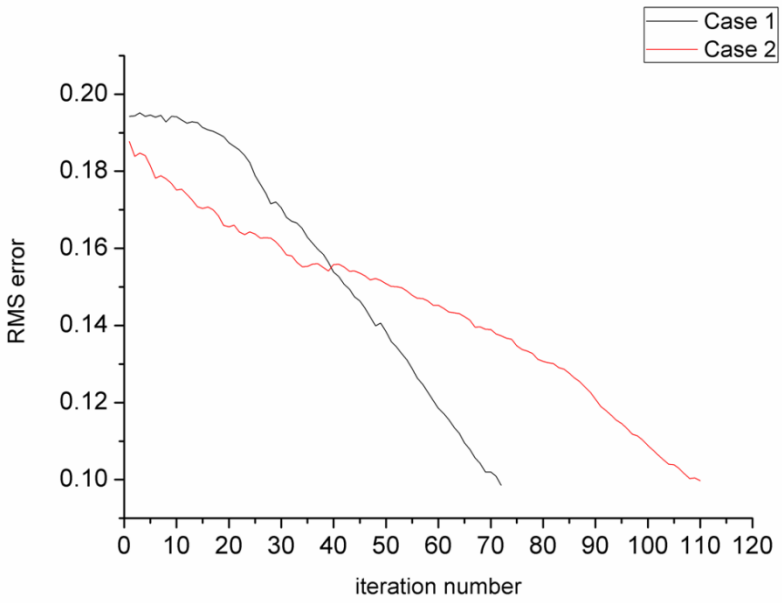


Figure 2−5. The convergence rate graph of the heart

segmentation of two cases (max RMS error : 0.1, max iteration : 250).

After heart segmentation, the surrounding region of the heart is also segmented by a level set method. The initial shape is the result of the previous heart segmentation. To calculate the speed function of $k_I$, u is set as 0 where the voxel value is between −400 and 0HU, while the other region is set as described by the equation (2−8). This level set method is implemented by using the ShapeDetectionLevelSetImageFilter in ITK Toolkit [38]. The segmentation of the heart and its surrounding tissue segmentations are performed on resampled volume with 2−mm iso−cubic voxels to improve the execution speed. The results of segmentation of the heart and its surrounding tissue are shown in Figure 2−4a−c. Figure 2−5 shows the convergence rate and termination conditions of level set algorithms using two example cases.

### 2.3.6 Extraction of thoracic cavity volume

The volume of the thoracic cavity can be evaluated on the basis of the five thoracic cavity surfaces by using Algorithm

2-1. The result of thoracic cavity segmentation is shown in Figure 2-3b. The final thoracic cavity volume is modified by adding the segmentation result of the heart and its surrounding tissue to decrease the false negatives. This method was used for the evaluations described in the Results section. The 3D view of the final thoracic cavity volume is shown in Figure 2-3c. In addition, the modified diaphragm surface can be extracted from the final thoracic cavity volume by boundary extraction and surface selection of the diaphragm surface. As described in section III.C, four surfaces are extracted to model the inner thoracic wall surface. These surfaces construct the point cloud designated as PC. PC is converted into a k-d tree for nearest neighbor searching by using Approximate Nearest Neighbor (ANN) Library[48]. The boundary point whose distance from PC is shorter than 10 mm is considered to be the inner thoracic wall, while the point that is more than 10mm from PC is considered to be the diaphragm surface. This method can divide the boundary surface into the thoracic wall and the diaphragm surface in Section III.F. However, the upper part of the thoracic cavity remains undelineated, especially because the four fitted surfaces do not provide the exact boundary line of the

mediastinum in the upper part. Therefore, in the apex of the lung, we interpolate the region of the left lung, right lung and airway with the rolling ball algorithm using a 40 mm−sized kernel. The result volume is used to extract the upper boundary of the thoracic cavity. In addition, to quantify the fat levels only, the pulmonary vessel structure is excluded from the mediastinum region by using morphological closing after deleting the lung region from the thoracic cavity region.

Algorithm 2−1. Pseudo algorithm for extracting thoracic cavity volume mask.

**Function** Thoracic cavity volume mask extraction

**Input**: lung mask $L_v$, the z range (a, b) of $L_v$, surfaces $S_i$, i = 1,2,⋯,5

**Output**: thoracic cavity mask $T_V$

Set an empty mask $M_1$.

Convert surfaces to volume mask and add them to $M_1$.

$M_2 = \sim M_1$

**for** $k$ = a +0.05*( b− a ) to b

Perform connected component analysis on $M_2(\cdot,\cdot,k)$

Calculate the overlapping area (OA) of each connected component with $L_V$.

Find the connected components of OA to remove the small size component.

Add these connected components to $T_V$.

**end for**

## 2.3.7 EVALUATION METRICS AND STATISTICAL ANALYSES

To evaluate the performance of our thoracic cavity

segmentation algorithm, it was compared to three conventional methods, namely, the TPS, graphcut, and *gridfit* methods. The manually segmented results of two expert radiographers and a thoracic radiologist were regarded as the gold standard. The gold standard of thoracic cavity segmentation includes the heart, the lung, the diaphragm, the pulmonary trunk, major vessels, and the esophagus in the mediastinum region. An expert manually delineated the diaphragm surface with −150 to 50 HU WWL, with which the diaphragm could be seen directly. The thoracic cavity segmentation was performed by finding the five surfaces enclosing thoracic cavity. The three conventional methods can extract the only diaphragm surface among the five enclosing surfaces. To test the three conventional methods correctly, we used the same four surfaces with the proposed method for thoracic wall. Six evaluation metrics were calculated: volumetric overlap ratio (VOR), the false positive ratio in VOR (FPRV), the false negative ratio in VOR (FNRV), average symmetric absolute surface distance (ASASD), average symmetric squared surface distance (ASSSD), and maximum symmetric surface distance (MSSD) [49]. In the present study, the boundary surface of the result volume mask was segmented

into two surfaces by the procedure described in Section III.F. In addition, three surface distance metrics ASASD, ASSSD, and MSSSD were calculated for both the inner thoracic wall and the diaphragm surface. To compare our algorithm to the three conventional algorithms, SPSS 17.0 (Armonk, New York, USA) was used to generate descriptive statistics and perform paired t-tests. The significance levels were set to 0.05, 0.01, and 0.001.

## 2.4 EXPERIMENTAL RESULTS

### 2.4.1 Subjects

In total, 50 patients with COPD underwent volumetric CT scans in the department of radiology, Asan Medical Center, South Korea. The CT scans were obtained by using a 16-multi detector row CT scanner (Siemens Sensation 16, Erlangen, Germany) with 0.75mm collimation, a smooth kernel (B30f), and 0.75mm slice thickness. The two radiographers with more than 5 years of experience delineated the rib cavity boundary by modifying the result of the proposed segmentation method.

An expert thoracic radiologist with more than 10 years of experience further modified these result and confirmed their validity as gold standard results.

## 2.4.2 Results

TABLE 2-1. Accuracy of the four thoracic cavity segmentation algorithms relative to the gold standard

| | TPS method | Graph-cut method | Gridfit method | Proposed method |
|---|---|---|---|---|
| VOR (%) | 97.28±1.41*** | 96.41±0.29*** | 97.40±1.48*** | 98.17±0.84 |
| FPRV (%) | 0.28±0.15 | 2.76±2.10*** | 0.28±0.16 | 0.49±0.23 |
| FNRV (%) | 2.45±1.41*** | 0.82±0.47 | 2.32±1.49*** | 1.34±0.83 |
| ASASD for thoracic wall (mm) | 0.33±0.17*** | 0.57±0.35*** | 0.33±0.19*** | 0.28±0.12 |
| ASSSD for thoracic wall (mm) | 1.59±0.86*** | 2.82±1.66*** | 1.65±0.96*** | 1.28±0.53 |
| MSSD for thoracic wall (mm) | 27.33±9.68*** | 39.38±14.54*** | 27.11±10.12** | 23.91±7.64 |
| ASASD for | 3.15±1.72*** | 4.25±3.29*** | 2.98±1.78*** | 1.73±0.91 |

| | | | | |
|---|---|---|---|---|
| diaphragm (mm) | | | | |
| ASSSD for diaphragm (mm) | 6.16±2.80*** | 7.16±4.83*** | 6.16±2.95*** | 3.92±1.68 |
| MSSD for diaphragm (mm) | 32.64±11.35*** | 36.15±15.38** | 30.95±10.68*** | 27.80±10.63 |

All p values derive from paired t-tests comparing our method with each of the three conventional methods. * $p< 0.05$, ** p<0.01, *** p<0.001.
VOR: volumetric overlap ratio; FPRV: false positive ratio in VOR; FNRV: false negative ratio in VOR; ASASD: average symmetric absolute surface distance; ASSSD: average symmetric squared surface distance; MSSD: maximum symmetric surface distance

Every metric of volumetry accuracy was evaluated using the result of each method and the gold standard. Evaluation results of these metrics were shown in Table 2-1 and pair-wisely compared among our proposed method and three other state-of-art methods including TPS, graphcut and *gridfit* methods described in Section III.D. As the accuracy of inner thoracic surface was higher than that of the diaphragm surface, we focused on the accuracy of diaphragm segmentation and compared the performances of our method and other diaphragm segmentation methods with the same inner thoracic

surface extraction algorithm. In the evaluation, the lung volume of thoracic cavity was not excluded to reduce ambiguity in the pulmonary vessel region.

Relative to the gold standard, our proposed method was significantly more accurate than the three conventional methods, in terms of most metrics, especially the surface distance metrics. The TPS and *gridfit* methods had significantly lower FPRV values than our method ($p<0.001$). While the graph-cut method yielded a significantly better FPRV than our method, it was associated with a significantly lower FNRV ($p<0.001$). As shown by the ASASD and ASSSD values, three methods and our method all modeled the inner thoracic surface markedly better than the diaphragm surface ($p<0.001$).

The *gridfit* method approximates the surface by using a gradient regulator. This regulator makes a curved surface in the upper direction between the bases of the left and right lungs. Therefore, the *gridfit* method yielded a relatively high rate of false negatives and a low rate of false positives. If the regulator were the spring, the approximated surface would be similar to a flat surface. Since addition of the heart and its surrounding tissue increases the resulting volume of the thoracic cavity, the

addition of the heart and its surrounding tissue could increase VOR by reducing the false negatives.


Figure 2-6. The segmentation results of two cases by the gold standard method (a-c and g-i) and the proposed algorithm (d-f and j-l). The columns show the axial, sagittal, and coronal images of the cases from left to right. For the first case (a-f), the thoracic cavity volumetry metrics VOR, FPRV, and FNRV of our method relative to the gold standard were 99.37%, 0.22%, and 0.41%, respectively. The ASASD, ASSSD, and MSSD for the

thoracic wall were 0.10 mm, 0.51 mm, and 11.13 mm, respectively while the ASASD, ASSSD, and MSSD for the diaphragm surfaces were 0.49 mm, 1.33 mm, and 16.02 mm, respectively. For the second case (g-l), the VOR, FPRV, and FNRV were 94.27%, 0.31%, and 5.43%, respectively. The ASASD, ASSSD, and MSSD for the thoracic wall were 0.75 mm, 3.44 mm, and 50mm, respectively while the ASASD, ASSSD, and MSSD for the diaphragm surfaces were 6.12 mm, 11.45 mm, and 56.38 mm, respectively.

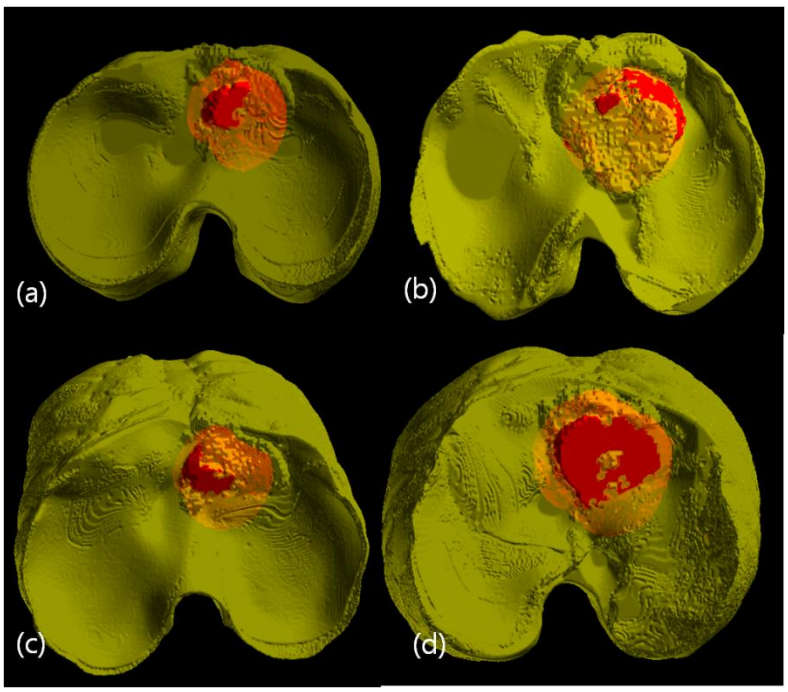


Figure 2-7. The 3d display of segmentation results of four cases (yellow : thoracic cavity, red : heart) (a)~(b) The 3d display for two cases of Figure 6 (c)~(d) The 3d display for two additional cases

The segmentation result of two cases was shown in Figure 2-6 in Multi-Planar Rendering view. The gold standard, convergence graph of the heart segmentation (Fig. 2-5), and the 3D display of the diaphragm (Fig. 2-7a and b) were also provided. To present more information about the diaphragm segmentation, we added the diaphragm segmentation result figures of two additional cases (Fig. 2-7c and d).

## 2.5 DISCUSSION

There could be a gap between the surface of the lung and the thoracic cavity surface. To evaluate the total fat composition of the thoracic cavity, the tissue in this gap should be included in thoracic cavity segmentation. Therefore, we used the inner surface of the ribs to model the thoracic cavity surface. This could be a more robust method for measurements in patients with various lung diseases.

Since the heart is sometimes attached to the liver, its boundaries are not clear in volumetric CT. Therefore, there could be leakage into the liver in this attached region. To prevent severe leakage, level set segmentation using a sphere as the shape prior was used for the heart segmentation in our

method.

As mentioned in the introduction, measuring the intra-thoracic tissue composition of patients with COPD could be useful for risk stratification. When making the mask for the fat quantification, we exclude the lung from the thoracic cavity region. In this case, the thoracic cavity region for a tissue composition analysis can be ambiguous, especially in the upper part of lung and around the airway. Moreover, it is difficult to determine how to consistently exclude the pulmonary vessel structure. Therefore, a systematic method of thoracic cavity definition and segmentation that permits reliable and accurate fat quantification is needed. The present paper proposed such a method. This method could also be used to evaluate the tissue outside the thoracic cavity, and the heart segmentation component could be used to automatically differentiate and measure epicardial fat. As far as we know, this is the first study on thoracic cavity segmentation in volumetric CT.

The present study showed that our method delineated the thoracic wall more accurately than the diaphragm surface. This reflects the fact that it is very difficult to identify the diaphragm surface accurately, especially around the backbone,

because of the fat between the diaphragm and the lung (Fig. 2-5h and k). Supporting this is two studies that reported DICE similarity coefficients of the inner thoracic wall and diaphragm surfaces of 0.985±0.005 and 0.942±0.010, respectively[24, 26].

When our method was compared to the conventional TPS, *gridfit*, and graph-cut methods, The TPS and *gridfit* methods had a significantly lower FPRV ($p<0.001$). The TPS and *gridfit* methods also missed significant amounts of inter thoracic tissue, which explains why their FNRV values were significantly higher than that of our proposed method ($p<0.001$). The graph-cut method did not accurately detect the thin diaphragm surface around the sternum, which resulted in a significantly higher FPRV compared to our method ($p<0.001$). The graph-cut method did not use the regulator but limit the difference between the z positions of grids by the inclined edge of the graph. Therefore the divergence sometimes occurred in a different direction, when information from the image could not guide the surface accurately.

This study had several limitations. It was based on a limited number of CT scans, only studied patients with COPD,

and used the same CT parameters. In addition, our method did not segment the diaphragm and heart with sufficient accuracy. The heart segmentation could be leaked into the liver through the vague boundary between the heart and the liver, although the shape prior information restricts this leakage. In addition, the segmentation result does not guarantee the smooth diaphragm surface due to discontinuity between the added region and the original thoracic volume. Moreover, our method needs two manual seeds on the heart, which means that fully automated thoracic cavity segmentation is still not possible. Additional studies will be performed to improve the heart segmentation method. For this, the method of Funka-Lea *et al.* will be used[30]. His method is more robust with regard to the location inside the heart in which the seed point should be placed. We will also improve the robustness of our proposed method with regard to CT reconstruction using various parameters. In addition, the diaphragm segmentation should be improved by using the upper boundary of diaphragm muscle, not the lower boundary of the lung. Finally, we will use our method to quantify the fat inside and outside the thoracic cavity, and determine the ratio between these quantities, in different

clinically important conditions, including diffuse interstitial lung disease, pulmonary tuberculosis, diabetes mellitus, sleep apnea, angina pectoris.

## 2.6 CONCLUSION

The composition of the tissue in the thoracic cavity region is regarded as being clinically important. However, it remains difficult to accurately segment the thoracic cavity region in volumetric CT because this region involves many organs and the diaphragm surface is unclear. In this paper, we proposed a semi-automated thoracic cavity segmentation method in which multiple organs, namely, the rib, lung, heart and diaphragm, are extracted, thus permitting delineation of the five surfaces that enclose the thoracic cavity. Our method was significantly more accurate relative to manual segmentation and delineation than three state-of-art methods. This study could be used as a framework to analyze the tissue composition of the thoracic cavity in various diseases.

# CHAPTER 3

# Semi-automatic decomposition method of pulmonary artery and vein using 2-level minimum spanning tree constructions in nonenhanced volumetric CT

# 3.1 INTRODUCTION

Quantitative assessments of the pulmonary vascular tree structures are important for analyzing vascular morphology and the effects on lung diseases [50]. Exact structural analyses of the pulmonary vasculature are difficult because each vascular tree contains a mixture of arterial and venous trees [51]. Moreover, partial volume effects and motion artifacts can make such analyses particularly problematic[52].

Especially for patients with chronic obstructive pulmonary disease (COPD), this quantification is becoming more and more important [53-55]. Matsuoka *et al.* recently reported a correlation between small pulmonary vessel areas and pulmonary function test (PFT) results [53]. Uejima *et al.* reported a correlation between vascular alterations (measured using cross-sectional area and airflow impairment) and normal pulmonary function in nonsmokers [54]. Estepar *et al.* also evaluated small-vessel volumes that were normalized to the total blood-vessel or nonvascular-tissue volumes in smokers [55]. The small-vessel volume was calculated using lobe-specific measurements, and vessels < 5 $mm^2$ were considered

small. In our group, the distributions of the pulmonary arteries and veins were separately evaluated in order to clarify the effects on lung diseases with inner offset surfaces at 5-mm intervals from the distal pulmonary structures [56].

In general, the automated extraction of accurate 3D pulmonary vascular structures from non-contrast CT images is difficult. Furthermore, explicit classification of the pulmonary arterial and venous subtrees is typically unsuccessful, although satisfactory segmentation can be performed. To solve this problem, the automatic decomposition of the pulmonary arteries and veins needs to be developed. Park *et al.* tried to perform this decomposition by constructing minimum spanning trees (MST) with 3 vertex weights and edge weights on whole-vessel volumes [52]. However, this method was based on manually placing the seeds with the label and, moreover, must be performed on whole-vessel voxels, which increases the running time for MST construction.

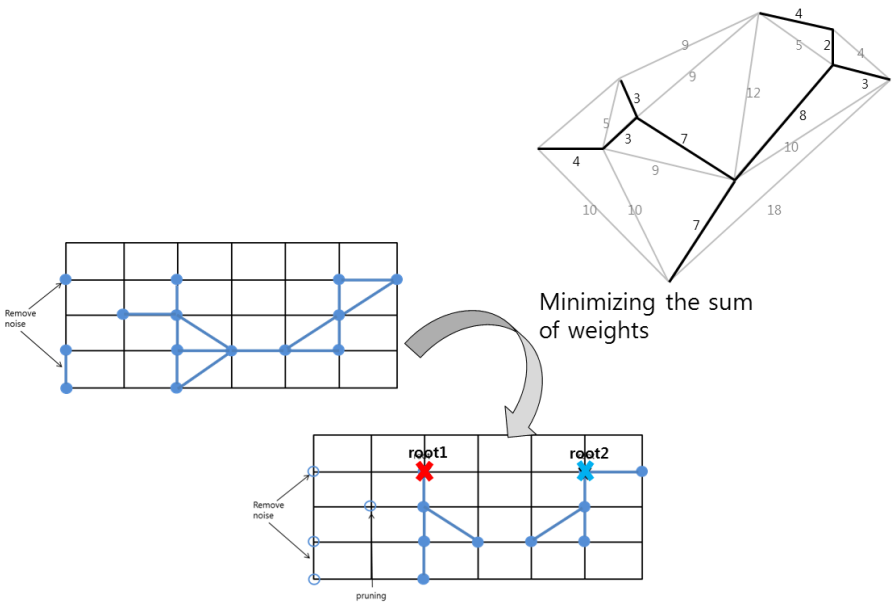


Figure 3-1. Multi-root minimum spanning tree construction theory.

The Dijkstra algorithm is a well-known, shortest path-finding algorithm used for constructing MSTs [57-59]. The Dijkstra algorithm is extended to construct MSTs by adapting multiple source inputs, which are defined as MDijkstra (Multi-root Dijkstra algorithm) [38, 60] (Figure 3-1). Since the execution time for MST construction under the whole-vessel voxels is long, 1 MST construction was divided into 2-level MST constructions. The MST construction for the first level was made in the preprocessing step, and in the interactive

decomposition processing time only the second-level MST construction was performed to reduce execution time. Since manually placing the seeds of the arterial and venous trees is time-consuming work, an automatic method of finding roots is an important part for automating vessel decomposition, especially for the second-level MST construction. Herein, we propose a method for automatically finding roots by filtering the morphological and spatial features of the vesselsand detecting important subsets of vessel skeleton-subtrees. Automatic root-finding will be combined with 2-level MST constructions in order to make an interactive program. This framework was designed to maximally reduce additional manual operations for split and merge operations.

In our present report, related studies are summarized in Section 2, the arterial and venous decomposition method is presented in Section 3, the statistical analysis method for the feature value set and efficient manual editing method are described in Section 4, decomposition evaluations are proposed in Section 5, and conclusions are presented in Section 6.

## 3.2 RELATED STUDIES

There are several studies on the separation of pulmonary arterial and venous subtrees on CT. Buelow *et al.* and Yonekura *et al.* previously proposed arterial and venous separation algorithms based on airway segmentation that used the specific anatomical features of the pulmonary arterial and venous trees [61, 62]. However, if the attachments between the artery and vein trees were severe, these methods could yield inaccurate separation. Lei *et al.* developed a separation method for arterial and venous trees based on magnetic resonance angiographic imaging data with fuzzy connectedness [63]. Although the use of fuzzy connectedness with given seeds is valid, that study was restricted to just the single separation of arterial and venous trees. Saha *et al.* proposed that multiscale topomorphological openings could be used to separate arteries and veins using 2 sets of seeds for arterial and venous trees, along with fuzzy distance transformation and fuzzy connectivity [64]. This research modified the fuzzy connectedness idea into a multiscale concept. In that approach, the user had to spend 2–3 minutes performing 1 separation. Although this group developed a local, updated procedure to improve the execution

time [65], the fundamental solution was not provided.

Park *et al.* proposed an automatic classification method for pulmonary arteries and veins that uses MDijkstra and weights to construct MSTs [52]. However, this method requires the conversion from volume data to a 3D point set, manual seed points by an expert, and a long operating time. Bemmel *et al.* suggested a level set-based arterial and venous separation method [66]. In this approach, the voxels are labeled as arterial or venous based on the arrival time at their respective surface. Propagation is governed by external forces related to the feature images and internal forces related to the geometry of the level sets. This evolution was initialized by the central arterial axes and central venous axes of the 2 surfaces, and this initialization is similar to our proposed method because our method uses the skeleton and mapping table to extract the whole-vessel volume. Chowriappa *et al.* proposed a 3-dimensional vascular skeleton extraction and decomposition method [67]. The decomposed structures were classified to identify aneurysm sacs for computer-aided detection [68]. They differentiated the vascular tree based on convex decomposition with approximate weights and a 3D shape index

analysis that was invariant under the natural deformations, which were composed of rigid and non-rigid deformations without a topology change.

Several methods have been proposed for vessel skeletonization. In medial axis transformation, a maximally inscribed sphere is used to track the centerline, which can be used for skeletonization. Although this method is an advanced skeleton extraction method that uses the average outward flux [69], for small vessels with < 2 voxels it is not possible to exactly extract the thin centerline. In this study, the 3D thinning algorithm was used to extract the vessel skeleton, especially including small-diameter vessels with topology preserving aspect and simple gradual peeling. [70].

To reconstruct the vascular trees, Szymczak *et al.* proposed a forest to connect the persistent maxima with the short edges and improve the forest by applying simple geometric filters that trim short branches, fill gaps in blood vessels, and remove spurious branches from the vascular tree [71]. The simple geometry method filters and trims short branches based on Kruskal's MST algorithm. That method constructed the minimum forest that uses the edges to connect

the points in a 3D point set that are shorter than the given threshold. Figueiredo *et al.* performed geometrical reconstructions using points, especially curved reconstructions for planar cases [72]. The point set can be separated into clusters by removing atypically long edges from the MSTs. This paper proposes 2 heuristic criteria for determining when an edge is too long. One is a global criterion, which removes the edges in order of decreasing length. The other is a local criterion, which removes edges that are much longer than the average length of the neighboring edges.

## 3.3 ARTERY AND VEIN DECOMPOSITION

### 3.3.1 Overall workflow

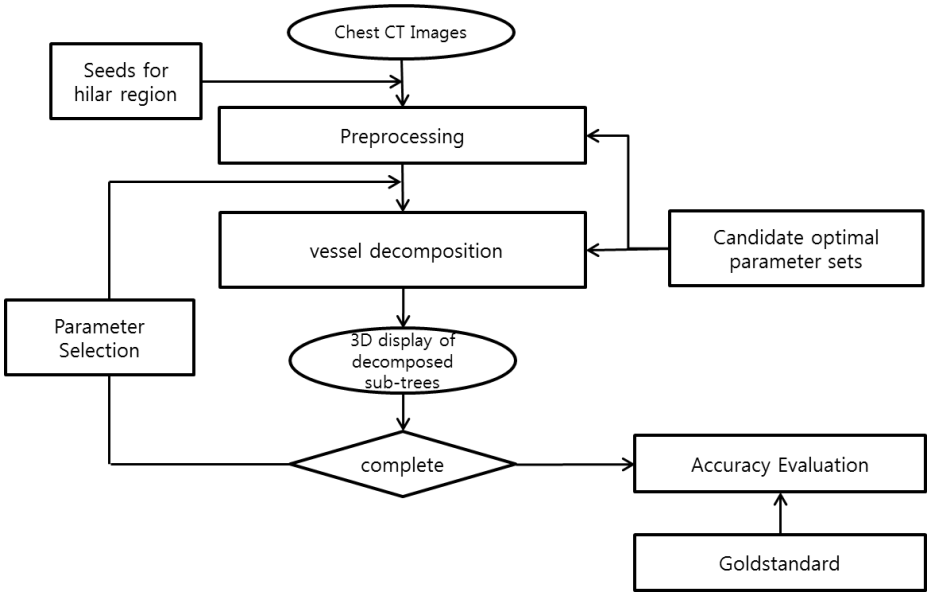


Figure 3-2. Flow chart of the overall procedure.

The overall procedure is shown in Figure 3-2, which included following parts: preprocessing, automatic vessel decomposition with roots automatically found for MST construction, accuracy evaluation on decomposed result by automatic classification through volumetric overlap with goldstandard. If the decomposed sub-trees were not complete, the vessel decomposition procedure was tried again with new parameter set. Although the hilar region could be detected

automatically, the detection of rough boundary of the hilar region frequently needs four or five candidate points around hilar region manually selected in 2D view.

### 3.3.2 Preprocessing

For pulmonary artery and vein decomposition, the preprocessing procedure included the following 4 major steps: 1) vessel segmentation; 2) initial tree construction; 3) statistical evaluation of the trees; and 4) construction of the first-level MST.

#### 3.3.2.1 Vessel segmentation

The vessel segmentation method was explained in a previous study [52]. Since the purpose of vessel decomposition is to quantify the separated arterial and venous subtrees, the simple threshold method was used to preserve the geometric features of the CT images.

The vessel structure was separately assessed for the left and right half-lungs. Airway segmentation and left-vs-right lung splits were performed using a previously described method [73-75]. Each half-lung was eroded in 3D with 2 pixels in

order to efficiently remove lung boundary noise because the intersecting objects between the lung mask and the vessel mask near the lung boundary could be included as noise under a given threshold. To segment the pulmonary vessels, an efficient approach that uses a threshold-based method with −750 Hounsfield Units (HU) on non-enhanced CT was used for the eroded lung region.

### 3.3.2.2 Initial tree construction

The vessel skeleton was extracted using the 3D thinning method. The vessel skeleton was created based on the spacing of the original image in order to prevent data loss. Since the threshold for the vessel segmentation was −750 HU, 3D thinning could be performed on the binary mask to extract the skeleton. In a later experiment, the skeleton threshold (SKTh) for extracting the subset from the vessel mask was selected based on the decomposition accuracy. After the skeleton was constructed using 26 connected neighborhoods, an undirected graph with nonnegative edge weights was constructed to evaluate their connectivity. Edges with 26 connectivity—composed of the center voxel and the neighboring voxels with a

distance weight—were linked if the vertexes of the edge were included in the skeleton mask. This edge construction was also computed on whole-vessel voxels. Edges were linked if the vertexes of the edge were included in the vessel mask. Two kinds of initial undirected graphs were used for statistical calculation and 2-level MST constructions.

The vertex weights of the initial undirected graph were calculated based on the previous study [52]. The weight is the average of 3 kinds of different weights: the attenuation intensity, the distance from the boundaries, and the Laplacian of the distance field. The normalization method was also performed on each weight in order to make the resulting value reside between 0 and 1. In this study, 2 types of MSTs were made for the skeleton vertexes and the whole-vessel voxels, which were compared with only 1 type of MST that was constructed using whole-vessel voxels in the previous study [52].

### 3.3.2.3 Subtree statistics

The radius was estimated by identifying the nearest neighboring boundary points of the vessel surface from the

skeleton, which could include ≥ 1 nearest points [76]. Therefore, a distance transformation was performed to estimate the vessel radius. The direction of each skeleton vertex was calculated based on the difference vector between the parent and current vertex. Estimating the radius and direction of each skeleton vertex is an error-prone process due to the discreteness of each skeleton vertex, so a smoothing procedure along each branch was performed to yield a more robust evaluation of the radius and directional data.

To distinguish each branch, a breadth-first search (BFS) was performed on each constructed skeleton MST. This search allowed the skeleton-subtrees to be divided into separate branches. In addition, the initial skeleton MST was constructed from the initial graph, and BFS was executed on this skeleton MST and the average values of the radius and direction of each skeleton vertex were calculated. After extracting the branch ID of each skeleton vertexes, the average values of radius and direction could be calculated.

### 3.3.2.4 The first level MST construction

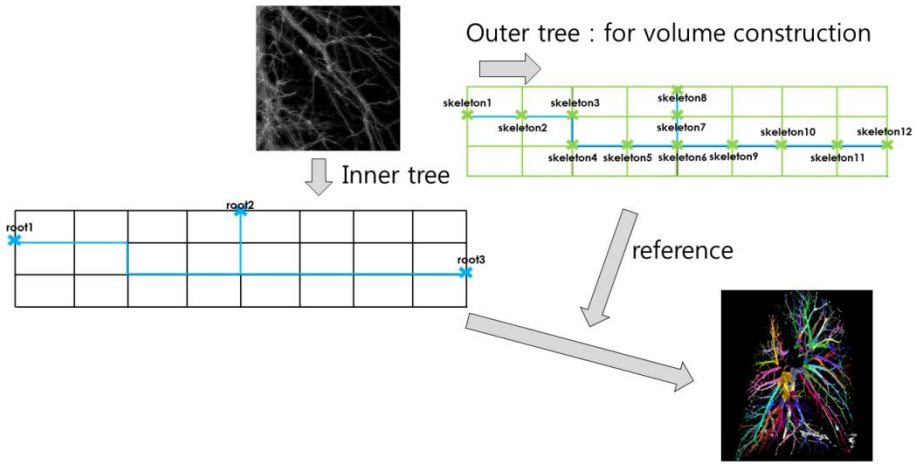


Figure 3-3. Two level minimum spanning tree constructions

Decomposition of the vessel subtrees was performed by 2-level construction of the MSTs. The construction of the MST with the skeleton vertexes as the target roots decomposed the vessel voxels into small fragments in the first level. In the second level, after constructing the MST on the skeleton graph with the automatically found roots, the decomposed small fragments of each skeleton vertex were combined based on the constructed second skeleton MSTs (Figure 3-3). The mapping table from the skeleton vertexes to either the surface or volume composed of the 3D points linked the skeleton vertexes to the small decomposed fragment of volume or surface.

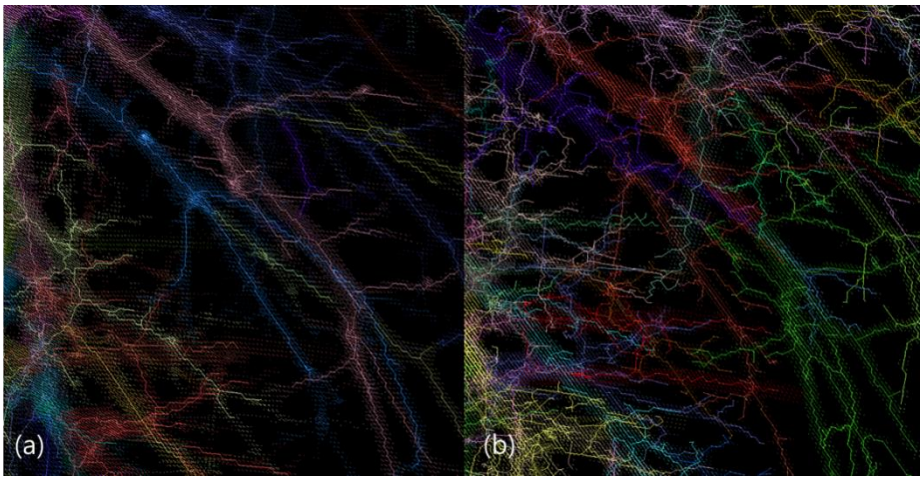


Figure 3-4. The skeleton graph and surface points mapped to that skeleton vertexes. (a) A part of pulmonary vessel region in the skeleton threshold of -550HU (b) The same vessel region with left figure in the skeleton threshold of -750HU.

When such data were available, a colored, textured vessel surface could be drawn. The surface points are shown in Figure 3-4, and the points of several colors represent points that were mapped using this procedure. The vertexes of the skeleton tree illustrated in Figure3-4 have corresponding surface points or volume points that were identified using this procedure. By identifying the voxels attached to a specific skeleton vertex, this map could be used for display, vessel selection, and the reconstruction of the vessels of selected

group IDs.

Cylinder construction around a vessel skeleton with a proper radius could be used to map the skeleton vertexes and vessel volume points. However, it can be difficult to identify the appropriate group for those voxels around a surface with a complex topology or bifurcating points. Importantly, the mapping table was made using MDijkstra, and this algorithm has strong characteristics for constructing the maps with such complex geometry. In addition, to determine the edges attached to a specific vertex, an incidence table was also used.

### 3.3.3 Root finding

The root-finding algorithm is important because the generation of the second-level MST would depend on the number and locations of the roots. To automatically identify roots in a given graph, the criteria to divide the graph must be considered. First, the connectivity of the graph could be used as a deciding factor for identifying root locations. This is, however, not enough because there could be unwanted connections. Among the pulmonary vessels, several vessels exist in 1

connected voxel object, while generally the vessel can be perceived from the morphology of the vessel’s structure. Therefore, a method for controlling this connectivity was proposed by filtering the edges. Unwanted roots can be removed using the proper filters with the optimal feature value set. The characteristics of the filter were made by considering vessel geometry and morphology, including vessel radius range, erosion number (ER) of the vessel mask, and additional thresholding on the vessel mask, which need to be optimized to control the connectivity of the graph and produce the proper roots. Additional size filtering of the connected object was performed to remove small objects using the total branch length (TBL). The number of the optimized feature value set in terms of filters, therefore, was 4.

The root-finding procedure includes edge filtering, size filtering of the connected object, and finding the roots from the connected object. To run this algorithm, a sequence of updated functions was performed as follows: 1) create an initial graph from the skeleton data; 2) filter the edges of the initial graph according to the selected features; 3) find the group; 4) filter the connected object based on TBL; 5) find the roots from the

important subset of vessel skeleton subtrees identified by filtering; and 6) run MDijkstra using the selected roots.

Size filtering worked in a different way in comparison with filtering the other features using the root-finding procedure. Figure 3-5 (e) shows skeleton trees that were filtered by size filtering. Figure 3-5(d) are the result of applying edge filtering with 3 selected features. Between procedures (2) and (4), there is "find group" procedure. After edge filtering for selected features, the groups for each skeleton-subtree were identified according to connectivity information. Figure 3-5(f) shows skeleton trees filtered by TBL. From these skeleton trees, the roots were calculated from the root candidate points, which were manually given.

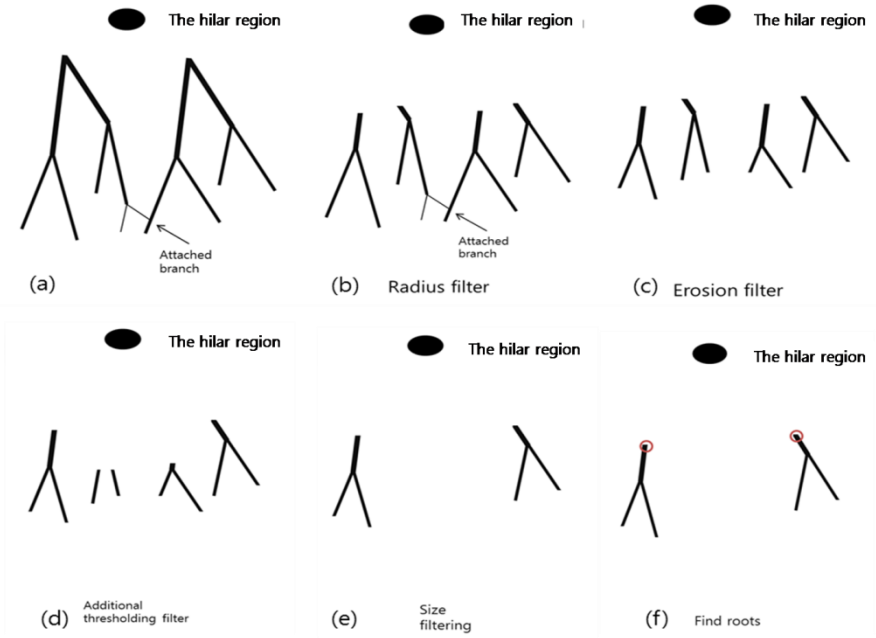


Figure 3-5. Sub-trees with distal branch attachment and automatic root finding procedure (a) Initial skeleton tree (b) skeleton trees after radius filter (c) skeleton trees after erosion filter (d) skeleton trees after additional thresholding filter (e) skeleton trees after size filtering (f) Root finding from the important subsets

The connected components of the dense voxels that label the resulting vessels are represented as $S_R = \{R_1, R_2, R_3, \ldots, R_{nR}\}$, and the root candidate points are represented as $RC = \{PC_1, PC_2, \cdots, PC_{nc}\}$. The distances between the point $R_x$ and the RC set were calculated by identifying the minimum point from the RC

point set. The point with the shortest distance from the RC point set among points $R_x$ was considered to be the root of the resulting vessel (Figure 3-5(c)). Basically, the root candidate points could be set as the hilar region points since the roots of the trees reside near the hilar region. But, especially, by using the manual split procedure, the root candidate points were set as the dividing skeleton vertexes since the split trees were made from the dividing points.

To more effectively tune the feature value set, an empirically selected feature value set could be given and a specific feature value set might be preferred based on the decomposition strategy.

### 3.3.4 Multi-root Dijkstra algorithm

The Dijkatra algorithm finds the MST for a weighted undirected graph [59]. Dijkstra algorithm's object grows from 1 source vertex into a tree of any size by adding vertices that are extracted from the priority queue, which can be used to divide the region into several parts based on the arrival timing of spanning tree construction under the given weight.

The connected objects of different groups could meet at 1

vertex. When this happened, MDijkstra removed the collided opposite edges to stop the growth of the opposite group object. The MDijkstra algorithm includes the collision detection algorithm by adding a line code (* in Figure 3-6) to solve this issue. This collision detection algorithm was brought from the mono-oriented group-growing algorithm[38]. This code searches for edges, including endpoints, and removes the identified edges from the maxHeap. Because the edges attached to the 1 vertex could be found by the incidence table, this line code could be executed without sequential searches. Since the binomial heap could perform combinations of insert, pop, and erase operations in O(nlogn) time ( 'n' is the object number) [58], the execution time of MDijkstra was bound to 3-4 minutes for the entire volume.

```
function MultiRootDijkstraAlgorithm(graph, source array,
 graph')
        group : -1 data array on each v
        parent : -1 data array on each v

        add sources to maxHeap.

        while maxHeap is not empty:
                pop edge e1 from maxHeap
                parent of e1.startpoint = e1.endpoint
                group[e1.endpoint] = group[e1.startpoint]
                add e1 to graph'

                remove edges including e1.endpoint from maxHeap *
                add unvisited neighbor e2 of e1.endpoint to maxHeap

        end while
        return graph'
end function
```

Figure 3-6. Multi-root Dijkstra algorithm. The input parameter *graph* is the initial graph of the vessels constructed using 26 connectivity. The input parameter *graph'* shows the vertexes structure without edges. NOTE * : code for considering multi-root.

The construction formula for MST can be found in Park *et al.*' s paper. In this paper, we redefined the construction formula for MST as a minimization problem in order to obtain a tree structure, T' = (V, E), that connects all of the vertices in V and whose construction energy (or cost) is minimized as Equation (3-1).

$$T' = \min_{T} C(T) \quad (3-1)$$

Because the set of vertices V is already given in this case, the construction energy is only affected by the connections of the edges. C(T) is then defined as the summation of the connecting energies of the edges, as shown as Equation (3-2).

$$C(T) = \sum_{(i,j)\in E} C(i,j) \qquad (3-2)$$

The construction energy of each edge connecting the *i-th* and *j-th* vertices is defined by Equation (3-3).

$$C(i,j) = \frac{\left\| v_j - v_i \right\|}{\alpha + \beta w_j + \gamma e_{ij} + \eta p_j} \qquad (3-3)$$

where, C(i,j) is the construction energy of each edge connecting the *i-th* and *j-th* vertices, $v_i$ and $v_j$ are the vertex position vectors, $w_j$ is the weight of vertex j, and $e_{ij}$ is the direction weight of edge(i,j) to a local orientation vector of vertex j. $p_j$ is the penalty weight of vertex j. $\alpha, \beta, \gamma, \eta$ (> 0) are positive real-value constants defined by the user, especially $\alpha$ must have a denominator $\neq 0$, and we set $\alpha = 1/5$, $\beta = 3/5$, $\gamma = 1/5$, and $\eta = 3/5$ for the skeleton vertexes used in the second level MST construction. In the first level MST construction case, we set $\alpha = 1/5$, $\beta = 3/5$, $\gamma = 0$, and $\eta = 0$.

The weight of the edge’s direction and the penalty weight were additionally adapted for the skeleton MST construction. The weight of the edge’s direction was calculated by the dot product of the average direction and the local edge direction. The penalty weight was calculated as the distance of the current vertex from the nearest points of the important subsets. This weight was made by MAX(0,1−dist/30 mm). This weight was the penalty that prevented a far point from the important subsets from being reached earlier by MDijkstra than a near point. The weight of the edge’s direction and the penalty weight were combined with the total weight by multiplication with the proper constants in Equation (3−3).

## 3.4 AN EFFICIENT DECOMPOSITION METHOD

For skeleton generation and a root−finding method, the candidate optimal feature value set could reduce the time and yield a more consistent feature value set.

### 3.4.1 Finding a candidate optimal feature value set

The automatic vessel decomposition procedure shown in Figure 3-2 was performed using a root-finding method and 2-level MST constructions. The vessel decomposition required 5 features and, since the lower radius limit (LR) was fixed at 0, the 5 optimal values of the 5features—including the upper radius limit (UR) for the vessel radius, TBL to remove small tree off, ER of the vessel mask, the additional threshold (ATh), and skeleton threshold (SKTh)—were tried by the grid-search method. Two features of the vessel, radius range and TBL, are related to the global shape of the skeleton of the vessel. Since the radius of the vessel tree decreases from the root to the distal branch, the radius range with LR of 0 value is an effective feature for tree decomposition. ER and ATh are the local shape features of the vessel skeleton since these features are not directly related to the change in the length of the vessel tree.

The optimal value was searched with LR, UR, TBL, ER and ATh under SKTh of -550HU by a particle swarm optimizer[74] of 10 particles and 10 iterations. For the prior knowledge, experiments were performed to find initial variables and a

search order. In these experiments, the optimal value for the optimizer to find was [0±0 mm, 1.70±0.55 mm, 13.83±10.80 mm, 1.1±0.85, and −176.42±151.17 HU for LR, UR, TBL, ER, and ATh respectively]. The optimal accuracy and decomposed vessel number of the pulmonary vessels were 89.34 ± 5.55% and 130 ± 107.42, respectively. In this experiment, the mean and standard deviation values of the decomposed vessel number were high. In addition, the local shape features showed large variance values compared with the global features. If the search-dimension of the particle swarm optimizer were large, the optimality of the search would be decreased.

In the field experiment, TBL and ATh were initially assumed to be 10 mm and −550 HU, respectively. To flexibly determine the feature values, a particle swarm optimizer with 10 particles and an iteration number of 10—which imitated interactive selection by the program operator—was used. If the grid number of the found axis were defined as *gn*, and the particle swarm optimizer was executed by the number of 10 x 10 x *gn* since the particle was 10 and the iteration was 10. The total test number of proposed grid search per each half-lung was 1908 times. This value could be calculated by summation

of 5x100(step 1), 6x100(step2), 5x100(step3), 3x100(step4), and 8(step5).This grid search proceeded in the following order: UR(step1), SKTh(step2), TBL(step3), ER(step4), and ATh(step5). For the optimizer's operation, the range of the feature values of ER and ATh were restricted between 0 and −750HU, and 2 and −100HU, respectively. Two local feature values could be varied at the same time, or only ATh could be varied by the optimizer for the grid−search time of ER.

A deterministic optimizer, such as the quasi−Newton method, could not be used to calculate the stable optimal value because the gradient value was not useful for evaluating the vessel decomposition algorithm. Therefore, a stochastic algorithm, which simulates the social behavior of a "flock of birds" or "school of fish", was used. The cost function of this optimizer minimizes the error value of arterial and venous decomposition.

### 3.4.2 Comparison with previous method

Park *et al*'s method was executed with the proposed automatic root−finding method to compare performance. The decomposition accuracies of Park *et al*'s method and this

proposed method were compared. These 2 methods have the same vertex weights. For comparison, SPSS 17.0 (Armonk, New York) was used to generate descriptive statistics and perform paired *t* tests with 2 tails.

## 3.5 EVALUATION

### 3.5.1 Accuracy evaluation

Let $T_a$ and $T_v$ denote the true segmentations of the arterial and venous subtrees, respectively, in the 20 half-lungs of the 10 patients with COPD. $S_a$ and $S_v$ denote the segmentations of the arteries and veins, respectively, that were computed using the current method. Since the decomposition results of the proposed method contain no classification information for the separated subtrees, the subtree was automatically classified as the arterial or venous subtree using the gold standard in order to calculate the decomposition accuracy. The automatic classification criterion is the area that overlaps with $T_a$ and $T_v$ in each subtree. After that, $S_a$ and $S_v$ can be calculated (Figure 3-7).

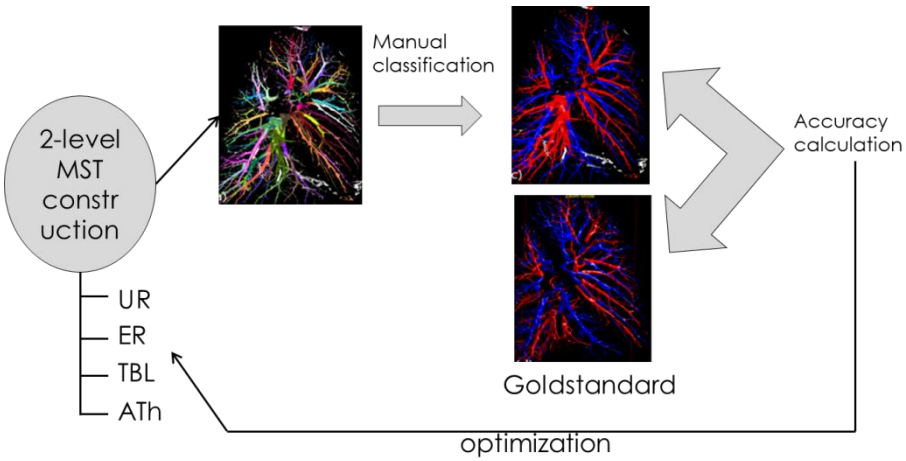


Figure 3-7. Accuracy evaluation of decomposition under optimization procedure

The gold standard mask used in our current report was generated using a sub-millimeter-thick, non-contrast, volumetric chest CT (the patient's breath was held at full inspiration) for the 10 patients with COPD. The hilar region was manually removed to separate the arteries and veins. An expert with > 10 years of experience generated the gold standards for the arterial and venous vessels for these 10 patients. Descriptive statistics of the arteries and veins of the gold standards were as follows: the mean and standard deviations of the lower radius, upper radius, lower distance, and upper distance were 0.33 ± 0.01 mm, 3.13 ± 0.55 mm, 14.59 ±

3.00 mm, and 180.75 ± 17.96 mm, respectively. The upper range value of the radius was relatively low because the gold standard did not contain the hilar region.

The accuracy and error of the computerized decomposition of the artery and vein were defined as follows.

$$Accuracy = \frac{(T_a \cap S_a) \cup (T_v \cap S_v)}{T_a \cup T_v} \qquad (3-4)$$

and

$$Error = \frac{(T_a \cap S_v) \cup (T_v \cap S_a)}{T_a \cup T_v} \qquad (3-5)$$

Since the gold standard was made by removing the hilar region, the resulting vessel mask is different from the gold standard, and the hilar region also was excluded from the accuracy calculation.

### 3.5.2 Determining the pseudo-optimal feature value set

In Table 3-1, step 1 shows the averaged decomposition results of the 20 half-lungs under the optimal UR searched by varying the UR value from 1 mm to 3 mm in 0.5-mm steps. In each half-lung case, after the optimal value and its

corresponding error (or accuracy) value were recorded, the recorded values were averaged over 20 half-lungs. The grid-search results show that when the upper radius value was low, the accuracy was high but the decomposed vessel number was high. In the grid-search experiment, we found that the value between 1.5 mm and 2.0 mm was optimal. Therefore, in the next grid-search step, 1.75 mm was used as the UR. In step 2, the optimal SKTh value was searched by varying a value from -500 HU to -750 HU in 50-HU steps. SKTh was used to determine the length of the vessel skeleton. With a high threshold value, the constructed vessel skeleton is shorter and contains the core part of the vessel. Figures 3-4 (a) and (b) compare the skeletons made with thresholds of -550 HU and -750HU. In the grid-search experiment, -550 HU was determined as the best SKTh value. For step 3, the optimal TBL was found by varying TBL from 10 mm to 30 mm in 5-mm steps with the grid search. If TBL increases, the decomposed vessel number decreases. Fifteen millimeters was used as the optimal TBL value. Step 4 is to find the optimal ER by varying it from 0 to 2 in 1 step. In this experiment, 1 was the optimal parameter. Finally, in step 5, the optimal ATh was

searched by varying ATh between −100 HU and −750 HU. The optimal parameter set was [0 mm, 1.75 mm, 15 mm, 1, −100HU, and −550HU for LR, UR, TBL, ER, ATh, and SKTh, respectively]. In this optimal set, the optimal accuracy and decomposed vessel number of the pulmonary vessels were 89.71 ± 3.76% and 75.1 ± 15.12, respectively. This value could be compared with the methods of the other steps (Table 3−1). The other methods, except the second method of step 1, were significantly more accurate ($p< 0.001$) in comparison with the optimal method in terms of accuracy and error terms. However, all other methods demonstrated significantly larger vessel numbers ($p< 0.05$) in comparison with the optimal method.

TABLE 3−1. Sequential grid search results from steps 1-5. The determined optimal values for each step are underlined. Each row shows the averaged decomposition results of the 20 half−lungs of 10 CT scans for the given 6 feature values. One or 2 of the possible values for the erosion

number and the additional threshold have flexibility to vary by an optimizer from steps 1–4.

| **Step** | **$N_{sep}$** | **Accu (%)** | **Error (%)** | **LR (mm)** | **UR (mm)** | **TBL (mm)** | **ER** | **ATh (HU)** | **SKTh (HU)** |
|---|---|---|---|---|---|---|---|---|---|
| **1** | 140.60±44.50*** | 93.36±2.49*** | 6.64±2.49*** | 0 | **1.5** | 10 | 0.65±0.67 | -241.12±119.46 | -550 |
| **1** | 98.20±31.29*** | 90.79±4.00 | 9.21±4.00 | 0 | **2** | 10 | 1.65±0.59 | -210.04±137.05 | -550 |
| **2** | 116.5±43.64*** | 92.34±2.88*** | 7.66±2.88*** | 0 | 1.75 | 10 | 1.84±1.03 | -221.74±134.14 | **-550** |
| **3** | 89.3±32.43* | 91.26±3.28*** | 8.74±3.28 | 0 | 1.75 | **15** | 0.85±0.75 | -214.76±135.73 | -550 |
| **4** | 93.1±32.49** | 91.25±3.22*** | 8.75±3.22*** | 0 | 1.75 | 15 | **1** | -217.31±144.02 | -550 |
| **5** | 75.1±15.12 | 89.71±3.76 | 10.29±3.76 | 0 | 1.75 | 15 | 1 | **-100** | -550 |

Note: $N_{sep}$, separated vessel number; Accu, accuracy; LR, lower radius; UR, upper radius; TBL, total branch length; ER, erosion number; ATh, the additional threshold; SKTh, the skeleton threshold

All $p$ values are derived from paired $t$ tests comparing the method of step 5 with the methods of the other steps.

*$p < 0.05$, **$p < 0.01$, ***$p < 0.001$.

The execution time of the second-level MST construction with the automatic root-finding procedure was found to be 3.58 ± 0.65 seconds using native voxel spacing. Additionally, the creation time for the mapping table between the skeleton vertexes and volume voxels was 234.55 ± 90.87 seconds with native voxel spacing. This was the execution time for the first level MST construction. This program was executed using an Intel Core i7 computer with 16-GB memory on a 64-bit Microsoft Windows 7 operating system.

### 3.5.3 Comparison with previous method

For the feature value set of [0 mm, 1.75 mm, 15 mm, 1, -100 HU, -550 HU], the decomposition accuracy and decomposed vessel number of pulmonary vessels of Park *et al*'s method were 83.77 ± 5.22% and 75.1 ± 15.12, respectively (Table 3-2), in comparison with 89.71 ± 3.76% and 75.1 ± 15.12 using the proposed method, thereby demonstrating significantly better accuracy ($p < 0.001$).

Table 3-2. Average decomposition results of the 20 half-lungs of 10 CT scans between the proposed method and the previous method

| Var (HU) | $N_{sep}$ | Accu (%) | error (%) | LR (mm) | UR (mm) | TBL (mm) | ER | ATh (HU) | SKTh (HU) |
|---|---|---|---|---|---|---|---|---|---|
| **Proposed** | 75.1±15.12 | 89.71±3.76 | 10.29±3.76 | 0 | 1.75 | 15 | 1 | -100 | -550 |
| **Previous** | 75.1±15.12 | 83.77±5.22*** | 16.23±5.22*** | 0 | 1.75 | 15 | 1 | -100 | -550 |

Note: $N_{sep}$, separated vessel number; Accu, accuracy; LR, lower radius; UR, upper radius; TBL, total branch length; ER, erosion number; ATh, the additional threshold; SKTh, the skeleton threshold

All $p$ values were derived from paired $t$ tests comparing the previous method with the proposed method.

*$p$ < 0.05, **$p$< 0.01, ***$p$< 0.001.

## 3.5.4 Four half-lung cases

Figures 3-8 and 3-9 show decomposition examples of 4 half-lungs. These results came from the feature value set [0 mm, 1.75 mm, 15 mm, 1, -100 HU, -550 HU]. This optimal value set did not need interactive adjustment and could be

applied directly for vessel decomposition. The second column of both figures shows the classified results from the decomposition results. The comparison between the second and third columns could give the perception of this algorithm's accuracy. The second half-lung of Figure 3-9 shows the worst case among 20 decomposed half-lungs.

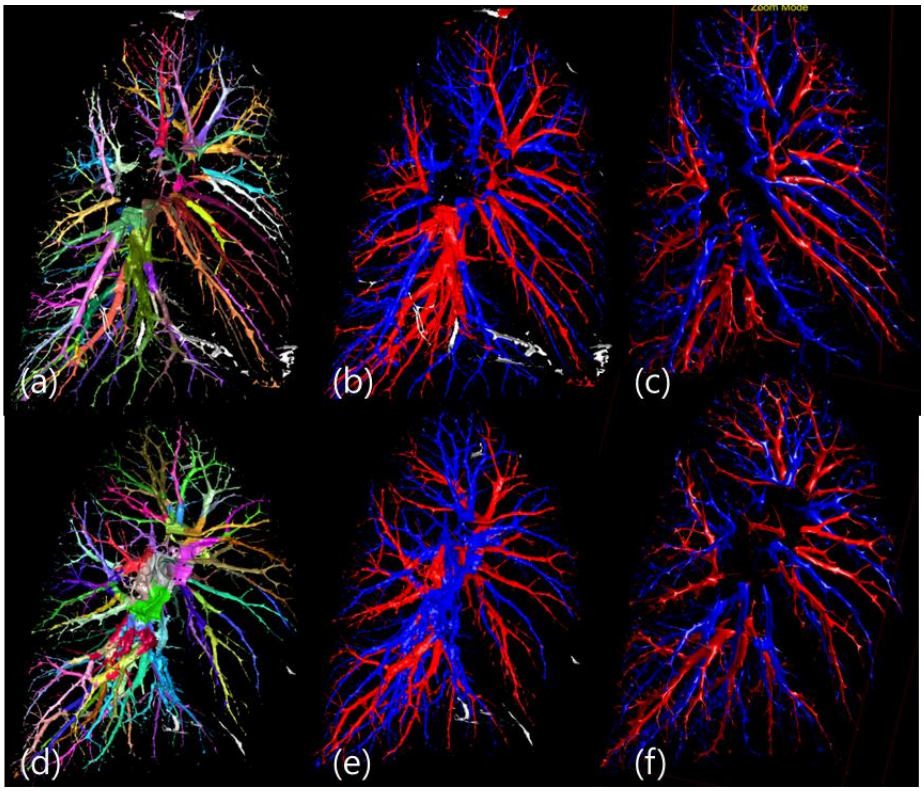


Figure 3-8. Two examples of decomposition of two half-lungs. Arteries are shown in blue and veins are shown in red. (a) Decomposition result of the first half-lung (b) The classified artery and vein result after classification of decomposition result

with goldstandard (Accuracy = 96.16%) (c) Goldstandard (d) Decomposition result of the second half-lung (e) The classified artery and vein (Accuracy = 93.89%) (f) Goldstandard

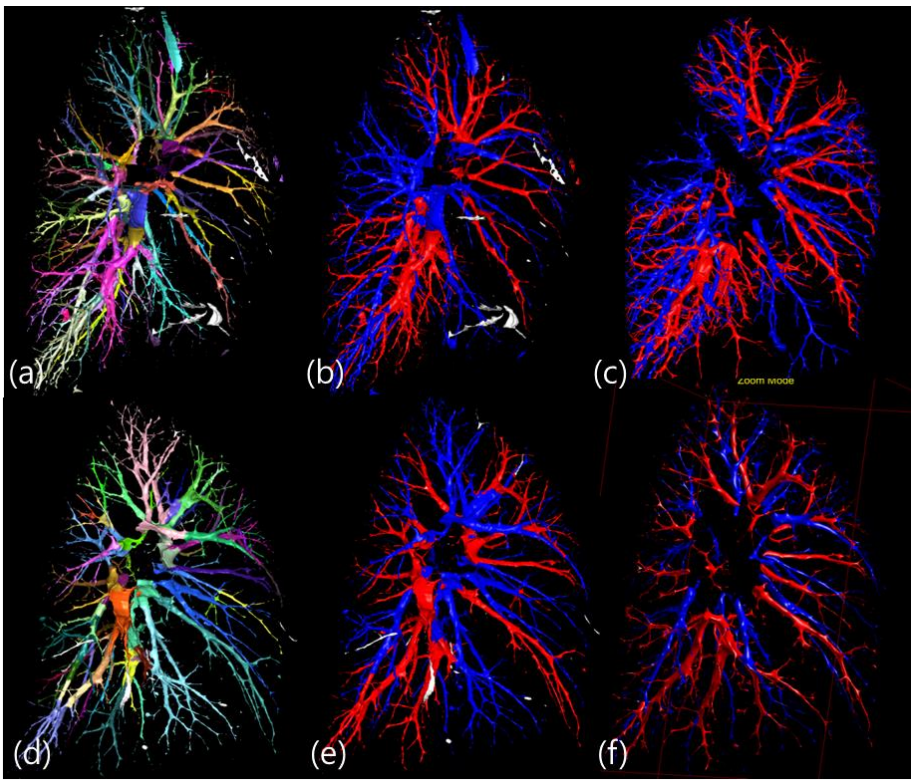


Figure 3-9. Two examples of decomposition of two half-lungs. Arteries are shown in blue and veins are shown in red. (a) Decomposition result of the first half-lung (b) The classified artery and vein result after classification of decomposition result with goldstandard (Accuracy = 92.03%) (c) Goldstandard (d) Decomposition result of the second half-lung (e) The classified artery and vein (Accuracy = 79.54%) (f) Goldstandard.

## 3.6 DISCUSSION AND CONCLUSION

We developed and validated the semiautomatic decomposition framework based on 2-level MST constructions for non-enhanced volumetric chest CT. This decomposition framework adapted the automatic root-finding method through 2 filters composed of edge filtering and size filtering. Through the experimental analysis of 5 features, the pseudo-optimal feature value set was determined for the automatic execution of decomposition. This decomposition framework could be used to differentiate the pulmonary arterial and venous subtrees with high accuracy and efficiency.

Quantification based on the classification of the arteries and veins could give us a tool for the development of imaging biomarkers for lung disease, which would be more important due to its noninvasiveness and relatively low economic cost. In addition, using this method, automatic differentiation of the pulmonary arteries and veins could be developed based on various features of the morphological and topological analyses of the pulmonary skeleton-subtrees.

It was challenging to determine the degree of invasion by

any branch into another tree and quantify the decomposition accuracy of the vessels, if it was dealt without the automatic classification under the artery and vein gold standards. However, it was also difficult to make gold standards only for decomposition. Saha *et al.* quantified the classification accuracy using the same strategy as our method [64]. However, their method put the seed with the label of the artery and vein. Therefore, the method did not need the classification procedure. In contrast, because our method adapted the automatic root-finding procedure, there was no information about the arterial or venous label. Therefore, automatic classification under the gold standards needed to be performed to calculate the decomposition accuracy. We quantitatively evaluated the decomposition accuracies of the vessels based on the gold standards, which would be useful for the further development of arterial and venous differentiation algorithms.

Although it yielded a satisfactory results, with an accuracy of around 90%. By interactively selecting feature value sets, our method could provide better results. The accuracy of 89.71% could be significantly increased if 2 local features were optimized for each half-lung. In the specific case of feature

value set optimization, the worst accuracy of the half-lung case with the final feature value set was 79.54% with a decomposed vessel number of 53 (the second case of Figure 3-9). But this half-lung case's accuracy could be increased to 89.14% with a decomposed vessel number of 113 when the feature value set was changed from [0 mm, 1.5 mm, 10 mm, 1, -100 HU, -550 HU] to [0 mm, 1.5 mm, 10 mm, 1, -285 HU, -550 HU]. Therefore, we need to develop a more robust optimization scheme.

In addition, extending the feature settings to the other features of the pulmonary vessel morphology and topology could improve the accuracy of the decomposition. Furthermore, we need more quantitative criteria to validate the decomposition results.

In conclusion, our proposed semiautomatic decomposition framework based on 2-level MST constructions could differentiate the arterial and venous subtrees with high efficiency. In the future, this algorithm could be clinically useful for the automated classification of the pulmonary arteries and veins.

# REFERENCES


1. Caban, J.J., Joshi, A., and Nagy, P. (2007). Rapid development of medical imaging tools with open-source libraries. Journal of Digital Imaging *20*, 83-93.
2. Erickson, B.J., Langer, S., and Nagy, P. (2005). The role of open-source software in innovation and standardization in radiology. Journal of the american college of radiology *2*, 927-931.
3. (2015). The Visualization Toolkit (VTK). (http://pulbic.kitware.com/VTK/(url)).
4. Bitter, I., Van Uitert, R., Wolf, I., Ibanez, L., and Kuhnigk, J.-M. (2007). Comparison of four freely available frameworks for image processing and visualization that use ITK. Visualization and Computer Graphics, IEEE Transactions on *13*, 483-493.
5. (2015). The Insight Toolkit (ITK). (http://www.itk.org).
6. Xu, Y., Sonka, M., McLennan, G., Guo, J., and Hoffman, E. (2006). MDCT-based 3-D texture classification of emphysema and early smoking related lung pathologies. Medical Imaging, IEEE Transactions on *25*, 464-475.
7. (1982). Medical Imaging and Interpretation (ISMII). In Proc. Int'l Symp. pp. 1-607.
8. Kass, M., Witkin, A., and Terzopoulos, D. (1988). Snakes: Active contour models. International journal of computer vision *1*, 321-331.
9. Koenderink, J.J. (1984). The structure of images. Biological cybernetics *50*, 363-370.
10. Maeda, K., Utsu, M., and Kihaile, P.E. (1998). Quantification of sonographic echogenicity with grey-level histogram width: a clinical tissue characterization. Ultrasound in medicine & biology *24*, 225-234.
11. Cohen, L.D., and Cohen, I. (1993). Finite-element methods for active contour models and balloons for 2-D and 3-D images. Pattern Analysis and Machine Intelligence, IEEE Transactions on *15*, 1131-1147.
12. Cootes, T.F., Taylor, C.J., Cooper, D.H., and Graham, J. (1995). Active shape models-their training and application. Computer vision and image understanding *61*, 38-59.
13. Osher, S., and Sethian, J.A. (1988). Fronts propagating with curvature-dependent speed: algorithms based on Hamilton-Jacobi formulations. Journal of computational physics *79*, 12-49.
14. Withey, D., and Koles, Z. (2007). Medical image segmentation: Methods and software. In Noninvasive Functional Source Imaging of the Brain and Heart and the International Conference on Functional Biomedical Imaging, 2007. NFSI-ICFBI 2007.

Joint Meeting of the 6th International Symposium on. (IEEE), pp. 140-143.
15. Iacobellis, G., Pistilli, D., Gucciardo, M., Leonetti, F., Miraldi, F., Brancaccio, G., Gallo, P., and di Gioia, C.R. (2005). Adiponectin expression in human epicardial adipose tissue in vivo is lower in patients with coronary artery disease. Cytokine *29*, 251-255.
16. Dey, D., Nakazato, R., Li, D., and Berman, D.S. (2012). Epicardial and thoracic fat-Noninvasive measurement and clinical implications. Cardiovascular Diagnosis and Therapy *2*, 85-93.
17. van den Borst, B., Gosker, H.R., and Schols, A.M. (2013). Central fat and peripheral muscle: partners in crime in chronic obstructive pulmonary disease. American journal of respiratory and critical care medicine *187*, 8-13.
18. Dey, D., Wong, N.D., Tamarappoo, B., Nakazato, R., Gransar, H., Cheng, V.Y., Ramesh, A., Kakadiaris, I., Germano, G., Slomka, P.J., et al. (2010). Computer-aided non-contrast CT-based quantification of pericardial and thoracic fat and their associations with coronary calcium and Metabolic Syndrome. Atherosclerosis *209*, 136-141.
19. Rosenquist, K.J., Pedley, A., Massaro, J.M., Therkelsen, K.E., Murabito, J.M., Hoffmann, U., and Fox, C.S. (2013). Visceral and subcutaneous fat quality and cardiometabolic risk. JACC. Cardiovascular imaging *6*, 762-771.
20. Furutate, R., Ishii, T., Wakabayashi, R., Motegi, T., Yamada, K., Gemma, A., and Kida, K. (2011). Excessive visceral fat accumulation in advanced chronic obstructive pulmonary disease. International journal of chronic obstructive pulmonary disease *6*, 423-430.
21. Vaes, A.W., Franssen, F.M., Meijer, K., Cuijpers, M.W., Wouters, E.F., Rutten, E.P., and Spruit, M.A. (2012). Effects of body mass index on task-related oxygen uptake and dyspnea during activities of daily life in COPD. PloS one *7*, e41078.
22. van den Borst, B., Gosker, H.R., Koster, A., Yu, B., Kritchevsky, S.B., Liu, Y., Meibohm, B., Rice, T.B., Shlipak, M., Yende, S., et al. (2012). The influence of abdominal visceral fat on inflammatory pathways and mortality risk in obstructive lung disease. The American journal of clinical nutrition *96*, 516-526.
23. Zhang, J., He, Z., and Huang, X. (2011). Automatic 3D Anatomy-based Mediastinum Segmentation Method in CT Images. JDCTA *5*, 266~274.
24. Chittajallu, D., Balanca, P., and Kakadiaris, I. (2009). Automatic delineation of the inner thoracic region in non-contrast CT data. Engineering in Medicine and Biology Society, 2009. EMBC 2009. Annual International Conference of the IEEE, 3569-3572.

25. Zhou, X., Ninomiya, H., Hara, T., Fujita, H., Yokoyama, R., Chen, H., Kiryu, T., and Hoshi, H. (2008). Automated estimation of the upper surface of the diaphragm in 3-D CT images. Ieee T Bio-Med Eng *55*, 351-353.
26. Yalamanchili, R., Chittajallu, D., Balanca, P., Tamarappoo, B., Berman, D., Dey, D., and Kakadiaris, I. (2010). Automatic segmentation of the diaphragm in non-contrast CT images. Biomedical Imaging: From Nano to Macro, 2010 IEEE International Symposium on, 900-903.
27. Rangayyan, R.M., Vu, R.H., and Boag, G.S. (2008). Automatic Delineation of the Diaphragm in Computed Tomographic Images. J Digit Imaging *21*, S134-S147.
28. Li, K., Wu, X.D., Chen, D.Z., and Sonka, M. (2006). Optimal surface segmentation in volumetric images - A graph-theoretic approach. Ieee T Pattern Anal *28*, 119-134.
29. Zheng, Y.F., Barbu, A., Georgescu, B., Scheuering, M., and Comaniciu, D. (2008). Four-Chamber Heart Modeling and Automatic Segmentation for 3-D Cardiac CT Volumes Using Marginal Space Learning and Steerable Features. Ieee T Med Imaging *27*, 1668-1681.
30. Funka-Lea, G., Boykov, Y., Florin, C., Jolly, M.-P., Moreau-Gobard, R., Ramaraj, R., and Rinck, D. (2006). Automatic heart isolation for CT coronary visualization using graph-cuts. Biomedical Imaging: Nano to Macro, 2006. 3rd IEEE International Symposium on, 614-617.
31. Zheng, Y., Vega-Higuera, F., Zhou, S.K., and Comaniciu, D. (2010). Fast and automatic heart isolation in 3D CT volumes: Optimal shape initialization. In Machine Learning in Medical Imaging. (Springer), pp. 84-91.
32. Leventon, M.E., Grimson, W.E.L., and Faugeras, O. (2000). Statistical shape influence in geodesic active contours. Computer Vision and Pattern Recognition, 2000. Proceedings. IEEE Conference on *1*, 316-323.
33. Kiraly, A.P., Higgins, W.E., McLennan, G., Hoffman, E.A., and Reinhardt, J.M. (2002). Three-dimensional human airway segmentation methods for clinical virtual bronchoscopy. Academic radiology *9*, 1153-1168.
34. Mori, K., Hasegawa, J., Toriwaki, J., Anno, H., and Katada, K. (1996). Recognition of bronchus in three-dimensional X-ray CT images with applications to virtualized bronchoscopy system. Pattern Recognition, 1996., Proceedings of the 13th International Conference on *3*, 528-532.
35. Hedlund, L., Anderson, R., Goulding, P., Beck, J., Effmann, E., and Putman, C. (1982). Two methods for isolating the lung area of a CT scan for density information. Radiology *144*, 353-357.

36. Kalender, W.A., Fichte, H., Bautz, W., and Skalej, M. (1991). Semiautomatic evaluation procedures for quantitative CT of the lung. Journal of computer assisted tomography *15*, 248.
37. Lee, Y.J., Lee, M., Kim, N., Seo, J.B., and Park, J.Y. (2013). Automatic Left and Right Lung Separation Using Free-formed Surface Fitting on Volumetric CT. submitted, .
38. Xie, H., McDonnell, T., and Qin, H. (2004). Surface reconstruction of noisy and defective data sets. In Visualization, 2004. IEEE. (IEEE), pp. 259-266.
39. D'Errico, J. Surface Fitting using gridfit - File Exchange - MATLAB Central. ([Online] Available: http://www.mathworks.com/matlabcentral/fileexchange/8998 [Accessed: 14-Oct-2013]).
40. Lay, D.C. Linear Algebra and its Applications. 2000. (Addison-Wesley/Longman, New York/London).
41. Bae, J.P., Kim, N., Kim, J.-E., Chang, Y., Lee, S.M., Seo, J.B., Lee, J., and Kim, H.C. (2013). Automatic Lung Segmentation for High-Resolution Computed Tomography of Patients with Diffuse Interstitial Lung Disease Using a Rib Detection and Inverse Level Set Algorithm. Submitted, .
42. Fabbri, R., Costa, L.D.F., Torelli, J.C., and Bruno, O.M. (2008). 2D Euclidean distance transform algorithms: A comparative survey. ACM Computing Surveys (CSUR) *40*, 2.
43. Bailey, D. (2005). An efficient euclidean distance transform. Combinatorial Image Analysis, 394-408.
44. Lorensen, W.E., and Cline, H.E. (1987). Marching cubes: A high resolution 3D surface construction algorithm. ACM Siggraph Computer Graphics *21*, 163-169.
45. Sethian, J.A. (1999). Level set methods and fast marching methods: evolving interfaces in computational geometry, fluid mechanics, computer vision, and materials science, Volume 3, (Cambridge university press).
46. Malladi, R., Sethian, J.A., and Vemuri, B.C. (1995). Shape Modeling with Front Propagation - a Level Set Approach. Ieee T Pattern Anal *17*, 158-175.
47. Byrd, R.H., Lu, P.H., Nocedal, J., and Zhu, C.Y. (1995). A Limited Memory Algorithm for Bound Constrained Optimization. Siam J Sci Comput *16*, 1190-1208.
48. Mount, D.M., and Arya, S. ANN: A Library for Approximate Nearest Neighbor Searching ([Online] Available: http://www.cs.umd.edu/~mount/ANN/ [Accessed: 14-Oct-2013]).
49. Van Ginneken, B., Heimann, T., and Styner, M. (2007). 3D segmentation in the clinic: A grand challenge. 3D segmentation in the clinic: a grand challenge, 7-15.

50. Palagyi, K., Tschirren, J., and Sonka, M. (2003). Quantitative analysis of three-dimensional tubular tree structures. In Proceedings of the International Conference on Information Processing in Medical Imaging (IPMI), C. Taylor and J.A. Noble, eds. (Ambleside, UK: Springer Verlag), pp. 222-233.
51. Estépar, R.S.J., Ross, J.C., Russian, K., Schultz, T., Washko, G.R., and Kindlmann, G.L. (2012). Computational vascular morphometry for the assessment of pulmonary vascular disease based on scale-space particles. Proceedings / IEEE International Symposium on Biomedical Imaging: from nano to macro. IEEE International Symposium on Biomedical Imaging, 1479-1482.
52. Park, S., Lee, S.M., Kim, N.K., Seo, J.B., and Shin, H. (2013). Automatic reconstruction of the arterial and venous trees on volumetric chest CT. Med. Phys. *40*, 071906.
53. Matsuoka, S., Washko, G.R., Dransfield, M.T., Yamashiro, T., San Jose Estepar, R., Diaz, A., Silverman, E.K., Patz, S., and Hatabu, H. (2010). Quantitative CT measurement of cross-sectional area of small pulmonary vessel in COPD: correlations with emphysema and airflow limitation. Acad. Radiol. *17*, 93-99.
54. Uejima, I., Matsuoka, S., Yamashiro, T., Yagihashi, K., Kurihara, Y., and Nakajima, Y. (2011). Quantitative computed tomographic measurement of a cross-sectional area of a small pulmonary vessel in nonsmokers without airflow limitation. Jpn J Radiol *29*, 251-255.
55. Estepar, R.S., Kinney, G.L., Black-Shinn, J.L., Bowler, R.P., Kindlmann, G.L., Ross, J.C., Kikinis, R., Han, M.K., Come, C.E., Diaz, A.A., et al. (2013). Computed tomographic measures of pulmonary vascular morphology in smokers and their clinical implications. Am. J. Respir. Crit. Care Med. *188*, 231-239.
56. Park, S.Y., Lee, S.M., Kim, N.K., Seo, J.B., and Choi, J.H. (2013). Quantification of the Distribution and Extent of Automatically Classified Small Pulmonary Arteries and Veins on Volumetric Chest CT In 2013 Radiological Society of North America 99th Scientific Assembly and Annual Meeting. (McCormick Place, Chicago, USA).
57. Prim, R.C. (1957). Shortest connection networks and some generalizations. Bell Syst. Technical J. *36*, 1389-1401.
58. Cormen, T.H., Leiserson, C.E., Rivest, R.L., and Stein, C. (2003). Introduction to Algorithms, 3rd Edition, (Cambridge, MA: MIT Press).
59. Dijkstra, E.W. (1959). A note on two problems in connexion with graphs. Numer. Math. *1*, 269-271.
60. Livny, Y., Yan, F., Olson, M., Chen, B., Zhang, H., and El-Sana, J. (2010). Automatic reconstruction of tree skeletal structures

from point clouds. ACM Transactions on Graphics (TOG) *29*, 151.
61. Buelow, T., Wiemker, R., Blaffert, T., Lorenz, C., and Renisch, S. (2005). Automatic extraction of the pulmonary artery tree from multi-slice CT data. Med. Imaging *5746*, 730-740.
62. Yonekura, T., Matsuhiro, M., Saita, S., Kubo, M., Kawata, Y., Niki, N., Nishitani, H., Ohmatsu, H., Kakinuma, R., and Moriyama, N. (2007). Classification algorithm of pulmonary vein and artery based on multi-slice CT image. Med. Imaging *6514*, 65142E-65142E-65148.
63. Lei, T., Udupa, J.K., Saha, P.K., and Odhner, D. (2001). Artery-vein separation via MRA-an image processing approach. Medical Imaging, IEEE Transactions on *20*, 689-703.
64. Saha, P.K., Gao, Z., Alford, S.K., Sonka, M., and Hoffman, E.A. (2010). Topomorphologic separation of fused isointensity objects via multiscale opening: separating arteries and veins in 3-D pulmonary CT. IEEE Trans. Med. Imaging *29*, 840-851.
65. Gao, Z., Grout, R.W., Holtze, C., Hoffman, E.A., and Saha, P.K. (2012). A New Paradigm of Interactive Artery/Vein Separation in Noncontrast Pulmonary CT Imaging Using Multiscale Topomorphologic Opening. Biomedical Engineering, IEEE Transactions on *59*, 3016-3027.
66. van Bemmel, C.M., Spreeuwers, L.J., Viergever, M.A., and Niessen, W.J. (2003). Level-set-based artery-vein separation in blood pool agent CE-MR angiograms. IEEE Trans. Med. Imaging *22*, 1224-1234.
67. Chowriappa, A., Seo, Y., Salunke, S., Mokin, M., Kan, P., and Scott, P. (2014). 3-D Vascular Skeleton Extraction and Decomposition. Biomedical and Health Informatics, IEEE Journal of *18*, 139-147.
68. Chowriappa, A., Salunke, S., Mokin, M., Kan, P., and Scott, P.D. (2013). 3D Vascular Decomposition and Classification for Computer-Aided Detection. Biomedical Engineering, IEEE Transactions on *60*, 3514-3523.
69. Bouix, S., Siddiqi, K., and Tannenbaum, A. (2005). Flux driven automatic centerline extraction. Med. Image Anal. *9*, 209-221.
70. Lee, T.C., Kashyap, R.L., and Chu, C.N. (1994). Building Skeleton Models Via 3-D Medial Surface Axis Thinning Algorithms. Cvgip-Graphical Models and Image Processing *56*, 462-478.
71. Szymczak, A., Stillman, A., Tannenbaum, A., and Mischaikow, K. (2006). Coronary vessel trees from 3D imagery: a topological approach. Med. Image Anal. *10*, 548-559.
72. De Figueiredo, L.H., and de Miranda Gomes, J. (1994). Computational morphology of curves. Vis Comput *11*, 105-112.

73. Black, M.J., and Rangarajan, A. (1996). On the unification of line processes, outlier rejection, and robust statistics with applications in early vision. Int J Comput Vis *19*, 57–91.
74. Kennedy, J. (2010). Particle swarm optimization. In Encyclopedia of Machine Learning, C. Sammut and G.I. Webb, eds. (New York: Springer), pp. 760–766.
75. Werneck, R.F. (2006). Design and analysis of data structures for dynamic trees. Volume PhD. (Princeton University).
76. Antiga, L. (2002). Patient-specific modeling of geometry and blood flow in large arteries. In Politecnico di Milano, Volume PhD. (Politecnico di Milano).

# 국문 초록

흉곽에 대한 컴퓨터 단층촬영 영상을 이용하여 흉강 분할 알고리즘과 폐 동맥 정맥 분리 알고리즘을 개발하고 그 성능을 평가하였다. 해당 연구는 흉곽 컴퓨터 단층 영상에서 임상적으로 의미 있는 장기를 분할하는 일을 자동화 했다는 점에서 중요하다. 장기 분할 정확성을 높이기 위해서 문턱값 방법을 기반한 형태적인 방법이나 연결성을 이용한 물체 선택 등의 기본적인 방법이 아닌, 좀 더 향상된 컴퓨터 공학적인 방법인 수치적인 방법과 그래프 이론을 이용한 방법을 처음으로 적용하였다. 본 논문에서는 위와 같이 제안된 새로운 연구 방법을 다음과 같은 두 가지 실례를 통해 시도하고 그 결과를 평가하였다.

첫번째 연구에서는 흉강을 분할 대상으로 하고 있다. 흉강은 흉강 벽과 횡경막에 의해 둘러 싸여 있는 장기를 말한다. 현재 본 연구가 대상으로 하고 있는 흉강의 경우 경계 부분에 변화가 큰 형태의 장기가 아니고 횡경막의 경우 얇은 두께의 막이기 때문에 그 형태가 컴퓨터 단층 영상 내에서 손실된 형태로 표현되어져 있는 경우가 많다. 종격동을 2 차원으로 찾는 것이라든지, 흉강벽과 횡경막을 따로 찾는 연구는 여러 연구에서 제시되어 있다. 하지만 흉강의 볼륨을 영상분할 하는 일에 대한 연구는 본 연구가 처음으로 제안을 하였다. 흉강 부피 관점에서 측정되는, 부피

겹치는 비율과 허위 양성 비율과 허위 음성 비율이 제안 방법은 98.17±0.84%, 0.49±0.23%, 1.34±0.83% 의 값이 도출되었다. 제안된 반자동화된 흉강 영상 분할 방법은 갈비뼈와 흉강벽, 횡경막, 그리고 심장 등의 여러 기관을 분할 방식을 기반으로 수행되고, 이는 임상적인 목적에서 높은 정확성과 유용성을 보여 주었다.

두번째 연구는 폐의 동맥 정맥 분리를 위해서 폐의 혈관을 부분혈관으로 자르는 방법을 제시하고 있다. 폐 동맥 정맥 분리의 경우에, 폐 암 수술 시뮬레이션 시의 기초자료로 쓰일 수 있다. 의료진이 머리 속으로 분리를 하거나 수작업으로 분리를 할 수 있으나, 자동화된 방법을 사용하는 것이 더 향상된 방법이다. 기존 방법의 경우에 수동으로 폐 혈관 뿌리쪽을 2D 슬라이스를 기반하여 혈관을 하나씩 따라가며 30~40 점을 찍어주는 과정이 필요하다. 그리고 이를 실행하는데 1 시간 30 분 정도의 시간이 필요하다. 특징값의 최적화 후에, 자동화된 동맥 정맥 분리 정확도는 정답과 비교했을 때 89.71±3.76%이었다. 이 분리 알고리즘은 폐 동맥 정맥의 자동화된 분류를 위해서 미래에 임상적으로 유용하게 사용될 수 있을 것이다.

---

**주요어 : 만성 폐색성 폐질환,컴퓨터 단층 촬영, 다기관 영상분할, 흉곽, 폐 동맥 정맥 분리, 이단계 최소신장트리 구축**

**학 번 : 2010-30263**

공학박사 학위논문

# Advanced segmentation algorithms using numerical model and graph theory

– Application to the lung images–

# 수치 모델과 그래프 이론을 이용한 향상된 영상 분할 연구

–폐 영상에 응용–

2016 년 2 월

서울대학교 대학원

협동과정 바이오엔지니어링 전공

배장표

A thesis of the Degree of Doctor of Philosophy

# 수치 모델과 그래프 이론을 이용한 향상된 영상 분할 연구

– 폐 영상에 응용–

# Advanced segmentation algorithms using numerical model and graph theory

– Application to the lung images–

February 2016

Interdisciplinary Program for Bioengineering
Graduate School,
Seoul National University
Jang PyoBae

# Advanced segmentation algorithms using numerical model and graph theory

by
Jang PyoBae

This Dissertation is approved for the Degree of Doctor Philosophy in Interdisciplinary Program for Bioengineering Graduate School at Seoul National University

February 2016

Approved by Thesis Committee:

Professor Jin Mo Goo Chairman
Professor Hee Chan Kim Vice chairman
Professor Namkug Kim
Professor Jaesoon Choi
Professor Jung Chan Lee

# ABSTRACT

This dissertation presents a thoracic cavity segmentation algorithm and a method of pulmonary artery and vein decomposition from volumetric chest CT, and evaluates their performances. The main contribution of this research is to develop an automated algorithm for segmentation of the clinically meaningful organ. Although there are several methods to improve the organ segmentation accuracy such as the morphological method based on threshold algorithm or the object selection method based on the connectivity information our novel algorithm uses numerical algorithms and graph theory which came from the computer engineering field. This dissertation presents a new method through the following two examples and evaluates the results of the method.

The first study aimed at the thoracic cavity segmentation. The thoracic cavity is the organ enclosed by the thoracic wall and the diaphragm surface. The thoracic wall has no clear boundary. Moreover since the diaphragm is the thin surface, this organ might have lost parts of its surface in the chest CT. As the previous researches, a method which found

the mediastinum on the 2D axial view was reported, and a thoracic wall extraction method and several diaphragm segmentation methods were also informed independently. But the thoracic cavity volume segmentation method was proposed in this thesis for the first time. In terms of thoracic cavity volumetry, the mean±SD volumetric overlap ratio (VOR), false positive ratio on VOR (FPRV), and false negative ratio on VOR (FNRV) of the proposed method were 98.17±0.84%, 0.49±0.23%, and 1.34±0.83%, respectively. The proposed semi-automatic thoracic cavity segmentation method, which extracts multiple organs (namely, the rib, thoracic wall, diaphragm, and heart), performed with high accuracy and may be useful for clinical purposes.

The second study proposed a method to decompose the pulmonary vessel into vessel subtrees for separation of the artery and vein. The volume images of the separated artery and vein could be used for a simulation support data in the lung cancer. Although a clinician could perform the separation in his imagination, and separate the vessel into the artery and vein in the manual, an automatic separation method is the better method than other methods. In the previous semi-automatic

method, root marking of 30 to 40 points was needed while tracing vessels under 2D slice view, and this procedure needed approximately an hour and a half. After optimization of the feature value set, the accuracy of the arterial and venous decomposition was 89.71 ± 3.76% in comparison with the gold standard. This framework could be clinically useful for studies on the effects of the pulmonary arteries and veins on lung diseases.

---

**Keywords:** chronic obstructive pulmonary disease (COPD), computed tomography, multi-organ segmentation, thoracic cavity, pulmonary artery and vein decomposition, two level minimum spanning tree constructions

**Student number:** 2010-30263

# CONTENTS

# LIST OF TABLES

## Chapter 1



## Chapter 2



## Chapter 3

# LIST OF FIGURES

## Chapter 2



## Chapter 3

# CHAPTER 1

# General Introduction

## 1.1 Image Informatics using Open Source

The concept of Open Source software (OSS) promotes the development and sharing of software source code under special licensing agreements that protects author's copyrights while maintaining the distribution of free and open derivative work based on the original code. The most successful example is Linux operating system.

Numerous Open Source initiatives in medicine leading to innovate and cost effective information systems supporting electronic patient record applications and medical imaging and PACS have emerged in the recent years. Recent reports showed that adoption of computerized medical records and medical informatics in medicine have significantly lagged behind expectations due to three major barriers: excessive cost, the transience of vendors, and the lack of command standards and adequate models many authors suggested. However Open Source software reduces these barriers by reducing ownership and development costs and facilitating the adaptation of customized tools for clinical practice[1].

The impact of open source is even greater in specialized areas of medicine such medical imaging[2]. The Visualization Toolkit or VTK[3] is well recognized and widely adopted software library that runs on multiple platforms and has been used for numerous scientific and medical applications so far[4]. The recent adjunction of the Insight Toolkit or ITK[5], mostly funded by the US National Library of Medicine as part of the Visible Human Project, adds a wealth of additional rendering and image processing tools for medical applications.

Quantitative assessment of lung structure along with indices of parenchymal pathology are taking on increased roles in the detection and tracking of pulmonary disease. To date the focus has largely been on airway morphometry and indices of parenchymal destruction, and air trapping. The parenchymal analysis has, in large part, focused on the use of the density histogram within the lung field to identify voxels falling below a given density threshold to define volumes of emphysema-like lung or air trapping. Some work has shown that texture measures can provide more accurate detection and quantification of pathology not limited to enlargement of peripheral air spaces[6]. Based on ITK and self-built in

libraries, MIRL of Asan medical center developed AView solution as quantitative tools for the assessment of the lung parenchyma, and used this solution in a number of large multi-center studies.

## 1.2 History of the segmentation algorithm

In Pre-1980 to 1984, the term "medical image analysis" was not yet in common use. However, a variety of meetings had included work related to the analysis of medical and biomedical images. A particular characteristic of most of the work during these years was that researchers were primarily thinking in terms of analyzing two-dimensional image datasets[7].

In mid-to-late 1980s, to some extent, research in the classic problems of boundary finding, 2D image matching, and ideas related to pattern recognition-driven, and computer-aided diagnosis continued. It is important to note that during the later part of this time frame, deformable models were discovered and then introduced into the field[8]. The concept of scale space theory to the problem was applied in negotiating the segmentation of complex medical image data by the type of scale-space hierarchies of intensity extrema[9]. Image texture

also was pursued as a feature useful for grouping and measurement in image analysis during this period, especially with respect to ultrasound image data[10].

In 1992 to 1998, the analysis of fully 3D images became a key goal and more mathematical-model-driven approaches became computationally feasible. Especially, deformable model methods were now coming into their own for medical applications, as different groups developed fully 3D "snakes" that could be run on volumetric image datasets[11]. In addition, approaches that incorporated shape priors were also extended into 3D, and another line of research pursued by Cootes et al. reported novel ways of introducing priors using point sets[12]. An interesting alternative to objective function-based deformable contours also emerged in this time frame in the name of level set algorithm[13]. Despite the successes noted above, it is fair to say that, as the 1990s draw to a close, no one algorithm can robustly segment a variety of relevant structure in medical images over a range of datasets.

Currently, methods for segmentation of medical images are divided into three generations, where each generation adds an additional level of algorithmic complexity[14]. The first

generation is composed of the simplest forms of image analysis such as the use of intensity thresholds and region growing. The second generation is characterized by the application of uncertainty models and optimization methods, and the third generation incorporates knowledge into the segmentation process. There are so much algorithms of variety technology for segmentation work where specific classification of segmentation algorithms is needed. Table 1-1 shows the classification summary of segmentation algorithms.

TABLE 1-1. Classification model summary

| Generation | Region-based | Boundary Following | Pixel Classification |
|---|---|---|---|
| 1st | •Region growing | •Edge tracing | •Intensity threshold |
| 2nd | •Deformable models<br>•Graph search | •Minimal path<br>•Target tracking<br>•Graph search<br>•Neural networks<br>•Multiresolution | •Statistical pattern recognition<br>•C-means clustering<br>•Neural networks<br>•Multiresolution |
| 3rd | •Shape models<br>•Appearance models | | •Atlas<br>•Rule-based |

| | | | |
|---|---|---|---|
| | •Rule-based<br>•Coupled surfaces | | |

The proposed method for thoracic cavity segmentation corresponds to the Rule-based method of 3rd and region-based method. This method extracts the special surface from the rib information. This extraction comes from the rule that the rib is in the boundary of the thoracic cavity. The pulmonary vascular segmentation and classification of arteries and veins matches to Graph search of 2nd and Region based. As separation using the shortest path algorithm is based on the graph theory, this algorithm corresponds to this category. But since the pulmonary vascular decomposition method uses the graph theory for the application of the interactive program, this algorithm must also be classified as interactive segmentation algorithm.

## 1.3 Goal of Thesis Work

Image segmentation is one of the most interesting and challenging problems in computer vision generally and medical imaging applications specifically. Segmentation partitions an

image area or volume into nonoverlapping, connected regions, which are homogeneous with respect to some signal characteristics. Medical image segmentation is of considerable importance in providing noninvasive information about human body structures that helps radiologists to visualize and study the anatomy of the structures, localize pathologies, track the progress of diseases, and evaluate the need for radiotherapy or surgeries. For these reasons, segmentation is an essential part of any computer-aided diagnosis (CAD) system, and functionality of the system depends heavily on segmentation accuracy. Moreover, this thesis has a further application in the improved imaging biomarker development through the segmentation software development specified on the thoracic region and pulmonary vessels.

Chapter 2 proposed the advanced segmentation algorithm for the thoracic cavity, and Chapter 3 argues the semi-automatic algorithm for decomposition of the artery and vein. These two segmentation methods were based on the volumetric chest CT.

# CHAPTER 2

# Thoracic cavity segmentation algorithm using multi-organ extraction and surface fitting in volumetric CT

## 2.1 INTRODUCTION

The thoracic cavity is the chamber of the human body that is protected by the thoracic wall and includes important organs such as the heart and lung. Quantification of the volumes of various features of the thoracic cavity, especially the amount of regional thoracic fat (fat within the inner thoracic cavity), would be of high clinical value because research over the past two decades shows that this fat may contribute to an unfavorable metabolic and cardiovascular risk profile[15, 16] and chronic obstructive pulmonary disease (COPD)[17]. For example, the levels of thoracic fat, which includes both epicardial and extra-pericardial fat, correlate strongly with pericardial fat levels (typically $r > 0.85$)[18]. Since subcutaneous fat and visceral fat associate with different metabolic risks, this means that the amount of fat in the thoracic cavity may be an important risk factor for heart disease[19]. In addition, muscle amount in the thoracic cavity could be important index for some cardiovascular diseases, because they represent volume of major vessels and heart[1]. In lung disease, the amount of visceral fat associates with low-

grade systemic inflammation, the severity and changes in emphysema and task-related metabolic demands[3,] [20-22]. In patients of COPD, the amount of visceral fat, muscle and calcification together may be a more accurate risk factor than the amount of visceral fat, as only the tissue close to the heart and the lung can be considered. These observations indicate that intra-thoracic tissue composition assessments in patients with COPD may be clinically useful. The presence of calcified plaque in vessel also associates with heart disease and COPD, and inflammation.

However, the fact that the thoracic cavity contains various organs significantly complicates its segmentation. As a result, manual thoracic cavity segmentation is a labor intensive and time-consuming task and inter-observer reliability cannot be guaranteed, especially for longitudinal studies and large-scale screening. To reduce the manual burden and improve reliability, automated computerized methods for segmenting the thoracic cavity region are needed. The present study describes the semi-computerized method that we developed for this purpose. This method involves a multi-organ extraction approach. To ensure that all the tissue inside the inner thoracic

cavity is included in the segmentation, the inner thoracic cavity is modeled by using the inner surface of the ribs. To segment the diaphragm, the diaphragm surface is modeled by using the bottom surfaces of the lung. To further improve the accuracy of diaphragm segmentation, additional segmentations of the heart and its surrounding tissue are performed. In addition, since the accurate extraction of mediastinum tissue is one of our clinical goals, the lung is subtracted from the thoracic cavity for clinical evaluation. In the present study, this proposed thoracic cavity segmentation method was tested in patients with COPD against the gold standard, namely, manual segmentation by two experts that was verified by an expert thoracic radiologist. It was also compared to three state-of-the-art thoracic cavity organ segmentation methods.

## 2.2 RELATED STUDIES

The organs in the thoracic cavity are the rib, lung, heart, and diaphragm. Most of previous studies on thoracic cavity segmentation focus on segmentation of only one of these organs. Moreover, few focus on the volumetric accuracy of the

segmentation. The studies on thoracic cavity segmentation include that by Zhang *et al.*, who proposed a segmentation algorithm of the mediastinum region that involved calculating four marginal points that constructed the mediastinum contour. However, this method did not accurately consider the diaphragm surface[23]. Chittajallu *et al.* proposed an optimal surface-detection method to identify the inner thoracic cavity and the inner points of the rib for the surfaces[24]. Many studies have sought to extract the diaphragm in chest CT[25-27], including the study by Xiangrong *et al.*, who proposed a method to extract the upper surface of the diaphragm[25]. They estimated the position of the diaphragm by deforming a thin-plate model that matched the bottom surface of the lung. Li *et al.* proposed a graphcut-cut method with a multi-column structure that allowed terrain-like surface estimation[28]. Yalamanchili *et al.* used this method to segment the diaphragmand adopted the cost function calculated on the basis of prior conditions to guide the surface into the target location[26]. Rangayyan*et al.* proposed a method for automatically delineating the diaphragm by modeling using the linear least-squares procedure, which extracted the initial

diaphragm model from the voxels of the base of the lungs. In addition, each dome of the diaphragm was modeled as a quadratic surface.

Although most previous studies on heart segmentation focused on segmenting the heart chambers[29], several also studied volumetric whole heart segmentation[30, 31]. Funka-Lea *et al.* proposed an isolation algorithm of the heart that used a particular means of initiating and constraining the graph-cut technique[30]. In the initiating step, an ellipsoid is grown progressively from the entry point to the heart wall. In the energy equation of the graph-cut, the blob constraint is added to make cuts that look like spheres[30]. Zheng *et al.* proposed a heart segmentation method that uses optimal shape initialization. In this method, the optimal mean shape is initialized in the location of the heart. The mean shape is then aligned with the detected pose, followed by boundary refinement using a learning-based boundary detector. That paper insisted that this algorithm is more accurate and faster than the graph-cut based method[31].

Our proposed method is a shape prior level set-based the heart segmentation method. This method uses a sphere as

the shape prior. The initial shape grows while maintaining the shape prior until this shape meets the stopping condition[32].

## 2.3 THE PROPOSED THORACIC CAVITY SEGMENTATION METHOD

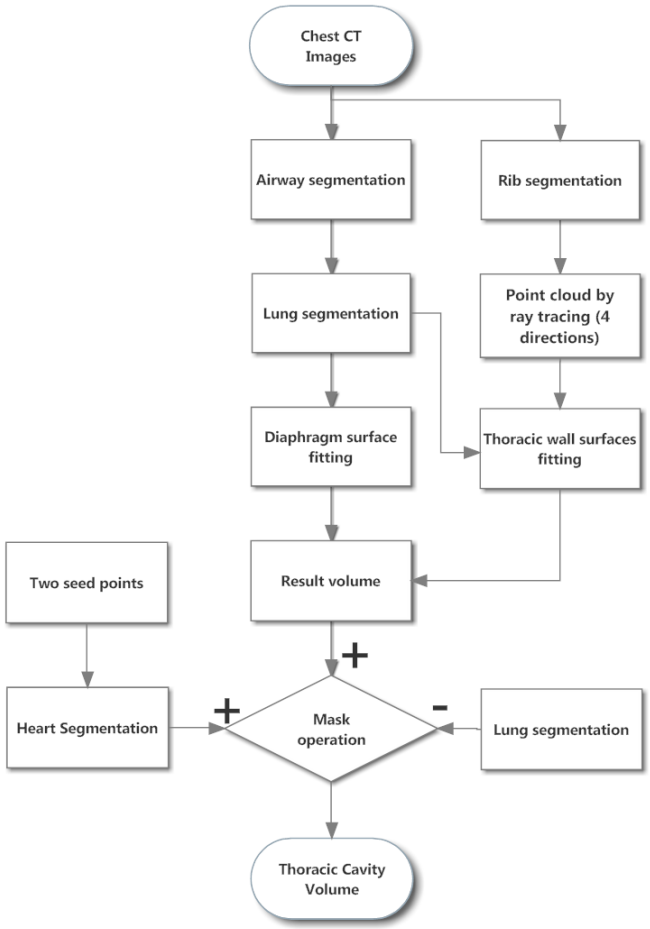


Figure 2-1. Schematic depiction of the steps in the proposed

thoracic cavity segmentation method.

In our method, airway segmentation, lung and heart segmentations and rib detection are performed first. After this, the thoracic cavity region is segmented by finding the five surfaces that enclose the thoracic cavity. The inner thoracic cavity is modeled by four surfaces along different directions from the inner points of the ribs. In addition, the diaphragm surface is approximated by the base voxels of the lung. These five terrain-like surfaces are approximated by a 3-dimensional (3D) surface-fitting method. Supplementary segmentations of the heart and its surrounding tissue are performed to improve the accuracy of diaphragm segmentation. For heart segmentation, two seed points are needed. Figure 2-1 shows a flow chart that schematically depicts our method.

### 2.3.1 Airway and lung segmentation

In our method, airway and lung segmentation are performed by using a thresholding method. The airway region is removed from the lung segment to differentiate the left and right lungs. From the seed point ($SP_1$) that is automatically

marked on the top of the airway region, a seeded region-growing method is performed to search for 3D connected regions below −924 Hounsfield Units (HU). This value was selected empirically on the basis that air is at approximately −1000 HU while soft tissues range of −100 to 200 HU[33]. The $SP_1$ in the airway can be at any point in the airway. Therefore, moving from the top slice to the bottom slice, we search the first slice for exactly three connected components with a specific size. $SP_1$ is determined by the center of inertia of the third largest connected component, because two other connected components would be the left and right lungs. As leakage may have occurred during region growing in airway segmentation, explosion-controlled region growing was performed[34].

In our method, to segment the lung, initial lung segmentation using a threshold value of −474 HU is performed. Previous studies have selected predetermined thresholds that range from −450 to −550 HU[35, 36]. In the present study, −474HU was chosen empirically to be the threshold value on the basis of the characteristics of our chest CT scans. The final lung is generated by subtracting the airway from the initial lung.

To differentiate the right and left lungs, connected components analysis on the final lung region is performed by selecting the two largest connected components. If the lung is not split after removing the airway region, the lung-split algorithm is performed[37]. This algorithm performs iterative eroding until the lung is split. Finally to smooth the lung boundary, the rolling-ball filter implemented by the ITK Toolkit[38] is applied; for this, the radius of the kernel is set to 4.

### 2.3.2 Surface-fitting method

The *gridfit* function, which was developed by using MATLAB R2012a (Mathworks Inc., Natick, MA, USA), is a surface modeling tool that fits a terrain surface (x,y,z) from scattered data[39]. Since the *gridfit* function is an approximant, not an interpolant, it uses the least-squares approximation to calculate the ill-conditioned solution in a linear algebra problem. The problem is described in the following equation:

$$Ax = y \quad (2-1)$$

where the number of data points is *t*, the number of the grid nodes is *s,* A is a $t \times s$ matrix, x is a $s \times 1$ matrix, and y is a $t \times 1$ matrix. x and y are point arrays, and x is an unkown

quantity. Matrix 'A' represents geometric relations between x and y. Four grid nodes constitute a rectangle where the approximation of the z value can be evaluated by a triangle interpolation. However, since the input data points are not evenly distributed, there are only a limited number of rectangles for calculating the z value. To determine the relationship between neighboring grid nodes, the regulator was suggested. In the gradient regulator, the following relationship must be satisfied at an arbitrary rectangle vertex V(x, y):

$$V(x-1,y)-2V(x,y)+V(x+1,\mathrm{y})=0 \quad (2-2)$$

$$V(x,y-1)-2V(x,\mathrm{y})+\mathrm{V}(\mathrm{x},\mathrm{y}-1)=0 \quad (2-3)$$

This relation is expressed by the following equations.

$$Bx=0 \quad (2-4)$$

where B is a $2s\times s$ matrix. Equations (2-1) and (2-4) are combined as follows:

$$\begin{pmatrix} A \\ \lambda B \end{pmatrix} x = Cx = \begin{pmatrix} y \\ 0 \end{pmatrix} \quad (2-5)$$

where $\lambda$ controlls the smoothness of the surface and C is a $(\mathrm{t}+2\mathrm{s})\times \mathrm{s}$ matrix. The solution could be provided by following equation[40].

$$x = \left(C^T C\right)^{-1} C^T \begin{pmatrix} y \\ 0 \end{pmatrix} \quad (2-6)$$

The equation was solved in the meaning of the minimum mean square root method[40].

### 2.3.3 Inner thoracic cavity surfaces

Inner wall of thoracic cavity are modeled by four partial surfaces. These surfaces are fitted by terrain-like surfaces from the point cloud of inner rib voxels. First, ribs were extracted as regions where the pixel intensities were larger than the value of 120 HU. Among the segmented regions, only a largest connected component was selected as the rib region. The sternum or breastbone is a flat bone that lies in the middle front part of the rib cage. As the inaccurate segmentation of the sternum could make the curved horizontal fitting surface in the sternum region, the selection of the threshold was important. In general, HU value of the sternum is slightly lower than the other bone. There was a trade-off between the inclusion of the sternum and the occurrence of the noise in determining HU value.

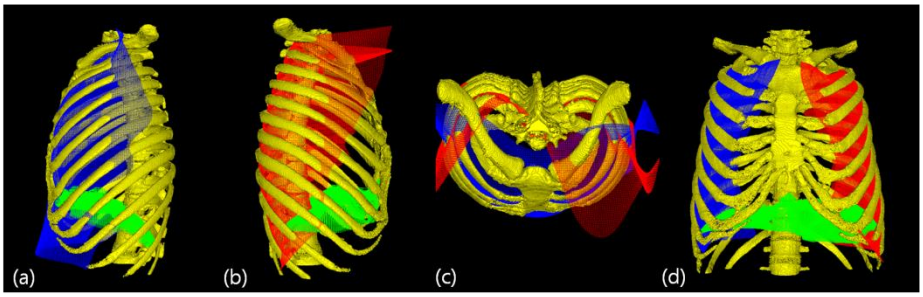


Figure 2-2. Five fitted surfaces. (a) The anterior left thoracic surface (blue), (b) The posterior right thoracic surface (red) (c) The dorsal view of the surfaces of (a) and (b) without the diaphragm (d) The left and right thoracic surfaces (red and blue, respectively) with the diaphragm surface (green)

The inner wall of thoracic cavity is found by anterior-posterior(AP) on the upper and lower ribs and radial ray projection on the left and right ribs[41]. AP rays are projected from the line crossing the centers of the left and right lungs while radial rays are projected from the centers of each half lung. The 3D surface-fitting are the points where the projection rays first touch the rib. To exclude points belonging to different bones such as scapular, the Euclidean distance field from the boundary of the lungs is generated by a volume-based method[42, 43] and the point cloud outside the 20 distance offset is removed.

Four point clouds are converted into terrain-like

surfaces by the *gridfit* algorithm. As described in section III.B, this algorithm approximates the 3D grid points by solving a linear algebra equation with a gradient regulator[39]. The resulting four surfaces are shown in Figure. 2-2. The*gridfit* function with 3mm by 3mm cells is performed and the fitting result is interpolated into the original volume spacing.

### 2.3.4 Diaphragm surface modeling

The diaphragm is a thin and double-domed muscle that separates between the thoracic and abdominal cavities. It is located below the lungs and forms the floor of the thoracic cavity on which the heart and lungs rest[26]. The similar appearance of the organs surrounding the diaphragm and the poor resolution of non-contrast CT scans makes the automatic segmentation of the diaphragm less accurate than inner thoracic cavity surface segmentation.

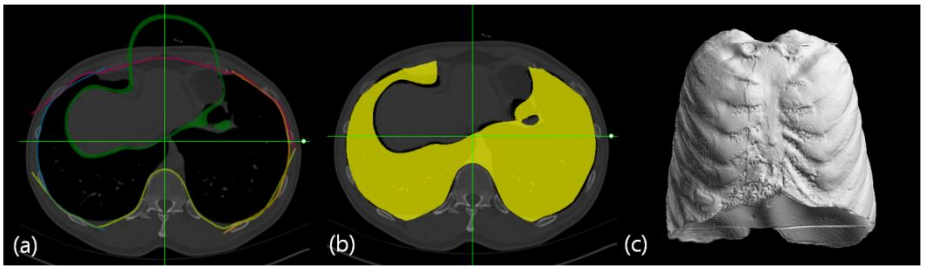


Figure 2-3. Extracting the thoracic cavity volume. (a) Five thoracic surfaces. The surfaces are depicted in red, magenta, light green, and blue, and the diaphragm is depicted in dark green as shown in the legend to FIG. 2-2. (b) Thoracic cavity volume (yellow) (c) Three-Dimensional display of the tissue inside the final thoracic cavity

The lower parts of the lung surfaces could be the initial left and right diaphragmatic surfaces. Zhou *et al.* extracted these diaphragm surfaces by considering the surface normal direction[25]. To calculate the surface normal direction, we must convert the volume into the surface composed of meshes by a marching cube algorithm[44]. Therefore, 3D ray projection from the lower position is easier than extracting the surface normal direction. In our method, the diaphragm surfaces are extracted by the 3D ray projection method from the two centers of the bottom of each lung along the half-sphere direction. The x and y positions of the starting point of ray

projection are calculated from the mass center of each half lung in the axial slice of the lung containing the liver dome. In addition, the z position is selected from the bottom slice containing the lung. The ray projection is performed along the half-sphere. To remove the noise voxels that are not the diaphragm, only the voxels below the liver dome are selected and the connected components whose voxel counts are below 1000 voxels are removed by labeling operator.

The diaphragm surface is located below the heart and above the liver in the central region. Therefore, for 3D surface fitting, the initial left and right diaphragmatic lung surfaces are input point cloud. The *gridfit* function is used for this fitting. Figure 2-3a shows the axial view that contains the inner thoracic cavity surfaces and the diaphragm surface.

In the present study, three state-of-art methods for modeling the thoracic cavity were implemented and compared with our proposed method. The Thin plate spline (TPS) method was developed on the basis of the TPS deformation method of Zhou *et al.*[25]. The base surface of each lung was considered as the diaphragm candidate with which the plate was deformed by using TPS deformation. To find the optimal surface of the

diaphragm segment, Li *et al.* and Yalamanchili *et al.* applied the graph-cut algorithm to the diaphragm segmentation[12, 28]. Finally, the *gridfit* method, as explained in section III.B, approximates the surface between the base surfaces of each lung by using the *gridfit* function. Comparison of the *gridfit* method to our proposed method will show the effect of adding the heart and its surrounding tissue. Since the *gridfit* method yields a similar diaphragm shape as the TPS method, the addition of the heart and its surrounding tissue to the TPS result should improve the segmentation.

### 2.3.5 Heart segmentation

We performed two-stage level set method to extract the heart and the pericardial fat from volumetric chest CT. In the first stage, the heart segmentation was performed by the level set method with a sphere as a shape prior. In the second stage, the surrounding pericardial fat was segmented with shape of the heart as a shape prior which was the segmentation result of the first stage. As pericardial fat is located around the heart, we performed the pericardial segmentation with the boundary of the heart as the starting position. Because the

diaphragm exists between the heart and the liver, the segmentation of the heart and its pericardial fat is needed to enhance diaphragm segmentation result.

In our method, the operator places two manual points on the heart, namely, on the upper and lower points of the heart on the sagittal plane that crosses near the center of the heart. From these seed points, the center ($c_h$) and the estimated radius ($r_e$) of the heart are calculated as follows:

$$c_h = \frac{1}{2}(p_1 + p_2), r_e = \frac{1}{2}(p_1 - p_2) \quad (2-7)$$

where $p_1$ and $p_2$ are the manually selected points. The level set method using a sphere as the shape prior is used to segment the heart. The initial shape for the level set is the sphere that uses the manually predetermined $c_h$ as its center and 0.6* $r_e$ as its radius; it is located on the sagittal plane of the center of the heart. The speed function is based on an edge potential map with user-defined masking to prevent leaking in the following equation[45, 46]:

$$k_I(x, y, z) = \begin{cases} \dfrac{1}{1 + |\nabla G * I(x, y, z)|} & \text{if } I(x, y, z) \geq u \\ 0 \text{ if } I(x, y, z) < u \end{cases} \quad (2-8)$$

where u is set by 0 HU, $k_I$ is a voxel of speed image, and I(x,y,z) is an image voxel. Generally, the user-defined value is set to prevent leakage across the edges.

This shape prior level set method is implemented by modifying the GeodesicActiveContourShapePriorLevelSetImageFilter in ITK Toolkit[38]. This filter adopted the level set method using a shape prior from Leventon *et al.*'s paper[32]. In this algorithm, the function of a shape prior was used to restrict the evolution of the level set surface considering the shape prior. The reason for heart segmentation is enhancement of diaphragm segmentation which would be hard to delineate correct especially below the heart. Compared with original filter implementation, shape and pose prior terms are changed for optimization purpose[32]. The shape prior term was replaced by using a Limited memory Broyden Fletcher Goldfarb Shannon (LBFPS) optimizer. This optimizer can restrict the search space. The pose prior was not used because the shape prior is a sphere[47]. This optimizer had four parameters: the radius, and the x, y and z positions from the center of the heart. The restricted search ranges of the optimizer are as follows: radius

($0.4*r_e$ ~ $1.4*r_e$), and the x, y and z positions from the center of the heart (−10 ~ 10 mm).

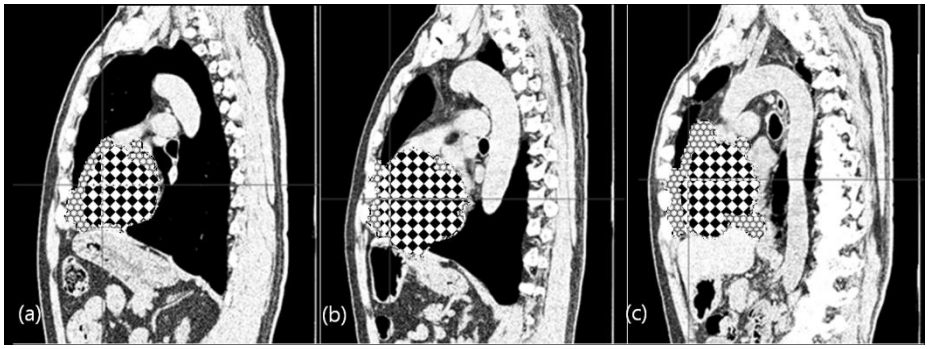


Figure 2−4. Segmentation of the heart and its surrounding tissue. (a−c) The result of segmentation of the heart and the surrounding tissue in three adjacent three sagittal planes. The heart is red and the surrounding tissue is blue.

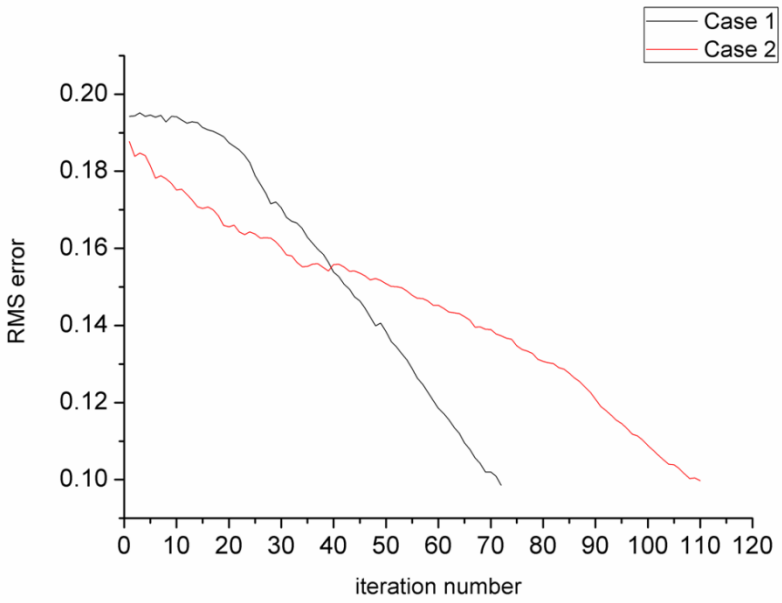


Figure 2−5. The convergence rate graph of the heart

segmentation of two cases (max RMS error : 0.1, max iteration : 250).

After heart segmentation, the surrounding region of the heart is also segmented by a level set method. The initial shape is the result of the previous heart segmentation. To calculate the speed function of $k_I$, u is set as 0 where the voxel value is between −400 and 0HU, while the other region is set as described by the equation (2−8). This level set method is implemented by using the ShapeDetectionLevelSetImageFilter in ITK Toolkit [38]. The segmentation of the heart and its surrounding tissue segmentations are performed on resampled volume with 2−mm iso−cubic voxels to improve the execution speed. The results of segmentation of the heart and its surrounding tissue are shown in Figure 2−4a−c. Figure 2−5 shows the convergence rate and termination conditions of level set algorithms using two example cases.

### 2.3.6 Extraction of thoracic cavity volume

The volume of the thoracic cavity can be evaluated on the basis of the five thoracic cavity surfaces by using Algorithm

2-1. The result of thoracic cavity segmentation is shown in Figure 2-3b. The final thoracic cavity volume is modified by adding the segmentation result of the heart and its surrounding tissue to decrease the false negatives. This method was used for the evaluations described in the Results section. The 3D view of the final thoracic cavity volume is shown in Figure 2-3c. In addition, the modified diaphragm surface can be extracted from the final thoracic cavity volume by boundary extraction and surface selection of the diaphragm surface. As described in section III.C, four surfaces are extracted to model the inner thoracic wall surface. These surfaces construct the point cloud designated as PC. PC is converted into a k-d tree for nearest neighbor searching by using Approximate Nearest Neighbor (ANN) Library[48]. The boundary point whose distance from PC is shorter than 10 mm is considered to be the inner thoracic wall, while the point that is more than 10mm from PC is considered to be the diaphragm surface. This method can divide the boundary surface into the thoracic wall and the diaphragm surface in Section III.F. However, the upper part of the thoracic cavity remains undelineated, especially because the four fitted surfaces do not provide the exact boundary line of the

mediastinum in the upper part. Therefore, in the apex of the lung, we interpolate the region of the left lung, right lung and airway with the rolling ball algorithm using a 40 mm−sized kernel. The result volume is used to extract the upper boundary of the thoracic cavity. In addition, to quantify the fat levels only, the pulmonary vessel structure is excluded from the mediastinum region by using morphological closing after deleting the lung region from the thoracic cavity region.

Algorithm 2−1. Pseudo algorithm for extracting thoracic cavity volume mask.

**Function** Thoracic cavity volume mask extraction

**Input**: lung mask $L_v$, the z range (a, b) of $L_v$, surfaces $S_i$, i = 1,2,⋯,5

**Output**: thoracic cavity mask $T_V$

Set an empty mask $M_1$.

Convert surfaces to volume mask and add them to $M_1$.

$M_2 = \sim M_1$

**for** $k$ = a +0.05*( b− a ) to b

Perform connected component analysis on $M_2(\cdot,\cdot,k)$

Calculate the overlapping area (OA) of each connected component with $L_V$.

Find the connected components of OA to remove the small size component.

Add these connected components to $T_V$.

**end for**

## 2.3.7 EVALUATION METRICS AND STATISTICAL ANALYSES

To evaluate the performance of our thoracic cavity

segmentation algorithm, it was compared to three conventional methods, namely, the TPS, graphcut, and *gridfit* methods. The manually segmented results of two expert radiographers and a thoracic radiologist were regarded as the gold standard. The gold standard of thoracic cavity segmentation includes the heart, the lung, the diaphragm, the pulmonary trunk, major vessels, and the esophagus in the mediastinum region. An expert manually delineated the diaphragm surface with −150 to 50 HU WWL, with which the diaphragm could be seen directly. The thoracic cavity segmentation was performed by finding the five surfaces enclosing thoracic cavity. The three conventional methods can extract the only diaphragm surface among the five enclosing surfaces. To test the three conventional methods correctly, we used the same four surfaces with the proposed method for thoracic wall. Six evaluation metrics were calculated: volumetric overlap ratio (VOR), the false positive ratio in VOR (FPRV), the false negative ratio in VOR (FNRV), average symmetric absolute surface distance (ASASD), average symmetric squared surface distance (ASSSD), and maximum symmetric surface distance (MSSD) [49]. In the present study, the boundary surface of the result volume mask was segmented

into two surfaces by the procedure described in Section III.F. In addition, three surface distance metrics ASASD, ASSSD, and MSSSD were calculated for both the inner thoracic wall and the diaphragm surface. To compare our algorithm to the three conventional algorithms, SPSS 17.0 (Armonk, New York, USA) was used to generate descriptive statistics and perform paired t-tests. The significance levels were set to 0.05, 0.01, and 0.001.

## 2.4 EXPERIMENTAL RESULTS

### 2.4.1 Subjects

In total, 50 patients with COPD underwent volumetric CT scans in the department of radiology, Asan Medical Center, South Korea. The CT scans were obtained by using a 16-multi detector row CT scanner (Siemens Sensation 16, Erlangen, Germany) with 0.75mm collimation, a smooth kernel (B30f), and 0.75mm slice thickness. The two radiographers with more than 5 years of experience delineated the rib cavity boundary by modifying the result of the proposed segmentation method.

An expert thoracic radiologist with more than 10 years of experience further modified these result and confirmed their validity as gold standard results.

## 2.4.2 Results

TABLE 2-1. Accuracy of the four thoracic cavity segmentation algorithms relative to the gold standard

| | TPS method | Graph-cut method | Gridfit method | Proposed method |
|---|---|---|---|---|
| VOR (%) | 97.28±1.41*** | 96.41±0.29*** | 97.40±1.48*** | 98.17±0.84 |
| FPRV (%) | 0.28±0.15 | 2.76±2.10*** | 0.28±0.16 | 0.49±0.23 |
| FNRV (%) | 2.45±1.41*** | 0.82±0.47 | 2.32±1.49*** | 1.34±0.83 |
| ASASD for thoracic wall (mm) | 0.33±0.17*** | 0.57±0.35*** | 0.33±0.19*** | 0.28±0.12 |
| ASSSD for thoracic wall (mm) | 1.59±0.86*** | 2.82±1.66*** | 1.65±0.96*** | 1.28±0.53 |
| MSSD for thoracic wall (mm) | 27.33±9.68*** | 39.38±14.54*** | 27.11±10.12** | 23.91±7.64 |
| ASASD for | 3.15±1.72*** | 4.25±3.29*** | 2.98±1.78*** | 1.73±0.91 |

| | | | | |
|---|---|---|---|---|
| diaphragm (mm) | | | | |
| ASSSD for diaphragm (mm) | 6.16±2.80*** | 7.16±4.83*** | 6.16±2.95*** | 3.92±1.68 |
| MSSD for diaphragm (mm) | 32.64±11.35*** | 36.15±15.38** | 30.95±10.68*** | 27.80±10.63 |

All p values derive from paired t-tests comparing our method with each of the three conventional methods. * $p< 0.05$, ** p<0.01, *** p<0.001.
VOR: volumetric overlap ratio; FPRV: false positive ratio in VOR; FNRV: false negative ratio in VOR; ASASD: average symmetric absolute surface distance; ASSSD: average symmetric squared surface distance; MSSD: maximum symmetric surface distance

Every metric of volumetry accuracy was evaluated using the result of each method and the gold standard. Evaluation results of these metrics were shown in Table 2-1 and pair-wisely compared among our proposed method and three other state-of-art methods including TPS, graphcut and *gridfit* methods described in Section III.D. As the accuracy of inner thoracic surface was higher than that of the diaphragm surface, we focused on the accuracy of diaphragm segmentation and compared the performances of our method and other diaphragm segmentation methods with the same inner thoracic

surface extraction algorithm. In the evaluation, the lung volume of thoracic cavity was not excluded to reduce ambiguity in the pulmonary vessel region.

Relative to the gold standard, our proposed method was significantly more accurate than the three conventional methods, in terms of most metrics, especially the surface distance metrics. The TPS and *gridfit* methods had significantly lower FPRV values than our method ($p<0.001$). While the graph-cut method yielded a significantly better FPRV than our method, it was associated with a significantly lower FNRV ($p<0.001$). As shown by the ASASD and ASSSD values, three methods and our method all modeled the inner thoracic surface markedly better than the diaphragm surface ($p<0.001$).

The *gridfit* method approximates the surface by using a gradient regulator. This regulator makes a curved surface in the upper direction between the bases of the left and right lungs. Therefore, the *gridfit* method yielded a relatively high rate of false negatives and a low rate of false positives. If the regulator were the spring, the approximated surface would be similar to a flat surface. Since addition of the heart and its surrounding tissue increases the resulting volume of the thoracic cavity, the

addition of the heart and its surrounding tissue could increase VOR by reducing the false negatives.


Figure 2-6. The segmentation results of two cases by the gold standard method (a-c and g-i) and the proposed algorithm (d-f and j-l). The columns show the axial, sagittal, and coronal images of the cases from left to right. For the first case (a-f), the thoracic cavity volumetry metrics VOR, FPRV, and FNRV of our method relative to the gold standard were 99.37%, 0.22%, and 0.41%, respectively. The ASASD, ASSSD, and MSSD for the

thoracic wall were 0.10 mm, 0.51 mm, and 11.13 mm, respectively while the ASASD, ASSSD, and MSSD for the diaphragm surfaces were 0.49 mm, 1.33 mm, and 16.02 mm, respectively. For the second case (g-l), the VOR, FPRV, and FNRV were 94.27%, 0.31%, and 5.43%, respectively. The ASASD, ASSSD, and MSSD for the thoracic wall were 0.75 mm, 3.44 mm, and 50mm, respectively while the ASASD, ASSSD, and MSSD for the diaphragm surfaces were 6.12 mm, 11.45 mm, and 56.38 mm, respectively.

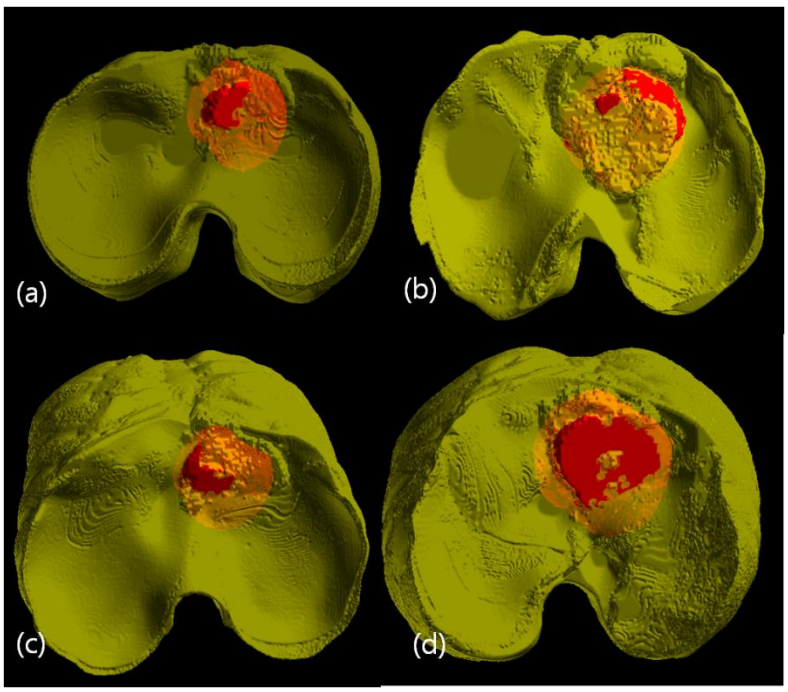


Figure 2-7. The 3d display of segmentation results of four cases (yellow : thoracic cavity, red : heart) (a)~(b) The 3d display for two cases of Figure 6 (c)~(d) The 3d display for two additional cases

The segmentation result of two cases was shown in Figure 2-6 in Multi-Planar Rendering view. The gold standard, convergence graph of the heart segmentation (Fig. 2-5), and the 3D display of the diaphragm (Fig. 2-7a and b) were also provided. To present more information about the diaphragm segmentation, we added the diaphragm segmentation result figures of two additional cases (Fig. 2-7c and d).

## 2.5 DISCUSSION

There could be a gap between the surface of the lung and the thoracic cavity surface. To evaluate the total fat composition of the thoracic cavity, the tissue in this gap should be included in thoracic cavity segmentation. Therefore, we used the inner surface of the ribs to model the thoracic cavity surface. This could be a more robust method for measurements in patients with various lung diseases.

Since the heart is sometimes attached to the liver, its boundaries are not clear in volumetric CT. Therefore, there could be leakage into the liver in this attached region. To prevent severe leakage, level set segmentation using a sphere as the shape prior was used for the heart segmentation in our

method.

As mentioned in the introduction, measuring the intra-thoracic tissue composition of patients with COPD could be useful for risk stratification. When making the mask for the fat quantification, we exclude the lung from the thoracic cavity region. In this case, the thoracic cavity region for a tissue composition analysis can be ambiguous, especially in the upper part of lung and around the airway. Moreover, it is difficult to determine how to consistently exclude the pulmonary vessel structure. Therefore, a systematic method of thoracic cavity definition and segmentation that permits reliable and accurate fat quantification is needed. The present paper proposed such a method. This method could also be used to evaluate the tissue outside the thoracic cavity, and the heart segmentation component could be used to automatically differentiate and measure epicardial fat. As far as we know, this is the first study on thoracic cavity segmentation in volumetric CT.

The present study showed that our method delineated the thoracic wall more accurately than the diaphragm surface. This reflects the fact that it is very difficult to identify the diaphragm surface accurately, especially around the backbone,

because of the fat between the diaphragm and the lung (Fig. 2-5h and k). Supporting this is two studies that reported DICE similarity coefficients of the inner thoracic wall and diaphragm surfaces of 0.985±0.005 and 0.942±0.010, respectively[24, 26].

When our method was compared to the conventional TPS, *gridfit*, and graph-cut methods, The TPS and *gridfit* methods had a significantly lower FPRV ($p<0.001$). The TPS and *gridfit* methods also missed significant amounts of inter thoracic tissue, which explains why their FNRV values were significantly higher than that of our proposed method ($p<0.001$). The graph-cut method did not accurately detect the thin diaphragm surface around the sternum, which resulted in a significantly higher FPRV compared to our method ($p<0.001$). The graph-cut method did not use the regulator but limit the difference between the z positions of grids by the inclined edge of the graph. Therefore the divergence sometimes occurred in a different direction, when information from the image could not guide the surface accurately.

This study had several limitations. It was based on a limited number of CT scans, only studied patients with COPD,

and used the same CT parameters. In addition, our method did not segment the diaphragm and heart with sufficient accuracy. The heart segmentation could be leaked into the liver through the vague boundary between the heart and the liver, although the shape prior information restricts this leakage. In addition, the segmentation result does not guarantee the smooth diaphragm surface due to discontinuity between the added region and the original thoracic volume. Moreover, our method needs two manual seeds on the heart, which means that fully automated thoracic cavity segmentation is still not possible. Additional studies will be performed to improve the heart segmentation method. For this, the method of Funka-Lea *et al.* will be used[30]. His method is more robust with regard to the location inside the heart in which the seed point should be placed. We will also improve the robustness of our proposed method with regard to CT reconstruction using various parameters. In addition, the diaphragm segmentation should be improved by using the upper boundary of diaphragm muscle, not the lower boundary of the lung. Finally, we will use our method to quantify the fat inside and outside the thoracic cavity, and determine the ratio between these quantities, in different

clinically important conditions, including diffuse interstitial lung disease, pulmonary tuberculosis, diabetes mellitus, sleep apnea, angina pectoris.

## 2.6 CONCLUSION

The composition of the tissue in the thoracic cavity region is regarded as being clinically important. However, it remains difficult to accurately segment the thoracic cavity region in volumetric CT because this region involves many organs and the diaphragm surface is unclear. In this paper, we proposed a semi-automated thoracic cavity segmentation method in which multiple organs, namely, the rib, lung, heart and diaphragm, are extracted, thus permitting delineation of the five surfaces that enclose the thoracic cavity. Our method was significantly more accurate relative to manual segmentation and delineation than three state-of-art methods. This study could be used as a framework to analyze the tissue composition of the thoracic cavity in various diseases.

# CHAPTER 3

# Semi-automatic decomposition method of pulmonary artery and vein using 2-level minimum spanning tree constructions in nonenhanced volumetric CT

# 3.1 INTRODUCTION

Quantitative assessments of the pulmonary vascular tree structures are important for analyzing vascular morphology and the effects on lung diseases [50]. Exact structural analyses of the pulmonary vasculature are difficult because each vascular tree contains a mixture of arterial and venous trees [51]. Moreover, partial volume effects and motion artifacts can make such analyses particularly problematic[52].

Especially for patients with chronic obstructive pulmonary disease (COPD), this quantification is becoming more and more important [53-55]. Matsuoka *et al.* recently reported a correlation between small pulmonary vessel areas and pulmonary function test (PFT) results [53]. Uejima *et al.* reported a correlation between vascular alterations (measured using cross-sectional area and airflow impairment) and normal pulmonary function in nonsmokers [54]. Estepar *et al.* also evaluated small-vessel volumes that were normalized to the total blood-vessel or nonvascular-tissue volumes in smokers [55]. The small-vessel volume was calculated using lobe-specific measurements, and vessels < 5 $mm^2$ were considered

small. In our group, the distributions of the pulmonary arteries and veins were separately evaluated in order to clarify the effects on lung diseases with inner offset surfaces at 5-mm intervals from the distal pulmonary structures [56].

In general, the automated extraction of accurate 3D pulmonary vascular structures from non-contrast CT images is difficult. Furthermore, explicit classification of the pulmonary arterial and venous subtrees is typically unsuccessful, although satisfactory segmentation can be performed. To solve this problem, the automatic decomposition of the pulmonary arteries and veins needs to be developed. Park *et al.* tried to perform this decomposition by constructing minimum spanning trees (MST) with 3 vertex weights and edge weights on whole-vessel volumes [52]. However, this method was based on manually placing the seeds with the label and, moreover, must be performed on whole-vessel voxels, which increases the running time for MST construction.

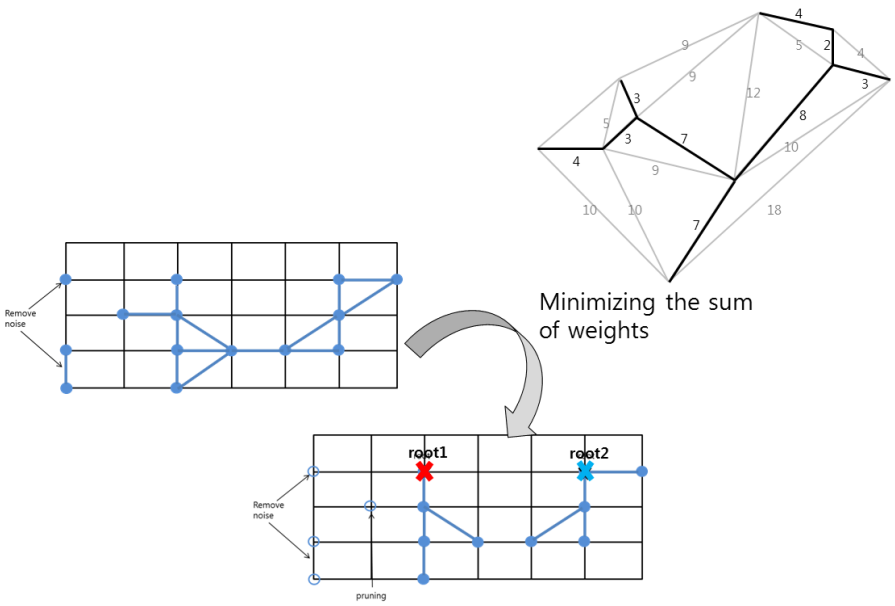


Figure 3-1. Multi-root minimum spanning tree construction theory.

The Dijkstra algorithm is a well-known, shortest path-finding algorithm used for constructing MSTs [57-59]. The Dijkstra algorithm is extended to construct MSTs by adapting multiple source inputs, which are defined as MDijkstra (Multi-root Dijkstra algorithm) [38, 60] (Figure 3-1). Since the execution time for MST construction under the whole-vessel voxels is long, 1 MST construction was divided into 2-level MST constructions. The MST construction for the first level was made in the preprocessing step, and in the interactive

decomposition processing time only the second-level MST construction was performed to reduce execution time. Since manually placing the seeds of the arterial and venous trees is time-consuming work, an automatic method of finding roots is an important part for automating vessel decomposition, especially for the second-level MST construction. Herein, we propose a method for automatically finding roots by filtering the morphological and spatial features of the vesselsand detecting important subsets of vessel skeleton-subtrees. Automatic root-finding will be combined with 2-level MST constructions in order to make an interactive program. This framework was designed to maximally reduce additional manual operations for split and merge operations.

In our present report, related studies are summarized in Section 2, the arterial and venous decomposition method is presented in Section 3, the statistical analysis method for the feature value set and efficient manual editing method are described in Section 4, decomposition evaluations are proposed in Section 5, and conclusions are presented in Section 6.

## 3.2 RELATED STUDIES

There are several studies on the separation of pulmonary arterial and venous subtrees on CT. Buelow *et al.* and Yonekura *et al.* previously proposed arterial and venous separation algorithms based on airway segmentation that used the specific anatomical features of the pulmonary arterial and venous trees [61, 62]. However, if the attachments between the artery and vein trees were severe, these methods could yield inaccurate separation. Lei *et al.* developed a separation method for arterial and venous trees based on magnetic resonance angiographic imaging data with fuzzy connectedness [63]. Although the use of fuzzy connectedness with given seeds is valid, that study was restricted to just the single separation of arterial and venous trees. Saha *et al.* proposed that multiscale topomorphological openings could be used to separate arteries and veins using 2 sets of seeds for arterial and venous trees, along with fuzzy distance transformation and fuzzy connectivity [64]. This research modified the fuzzy connectedness idea into a multiscale concept. In that approach, the user had to spend 2–3 minutes performing 1 separation. Although this group developed a local, updated procedure to improve the execution

time [65], the fundamental solution was not provided.

Park *et al.* proposed an automatic classification method for pulmonary arteries and veins that uses MDijkstra and weights to construct MSTs [52]. However, this method requires the conversion from volume data to a 3D point set, manual seed points by an expert, and a long operating time. Bemmel *et al.* suggested a level set-based arterial and venous separation method [66]. In this approach, the voxels are labeled as arterial or venous based on the arrival time at their respective surface. Propagation is governed by external forces related to the feature images and internal forces related to the geometry of the level sets. This evolution was initialized by the central arterial axes and central venous axes of the 2 surfaces, and this initialization is similar to our proposed method because our method uses the skeleton and mapping table to extract the whole-vessel volume. Chowriappa *et al.* proposed a 3-dimensional vascular skeleton extraction and decomposition method [67]. The decomposed structures were classified to identify aneurysm sacs for computer-aided detection [68]. They differentiated the vascular tree based on convex decomposition with approximate weights and a 3D shape index

analysis that was invariant under the natural deformations, which were composed of rigid and non-rigid deformations without a topology change.

Several methods have been proposed for vessel skeletonization. In medial axis transformation, a maximally inscribed sphere is used to track the centerline, which can be used for skeletonization. Although this method is an advanced skeleton extraction method that uses the average outward flux [69], for small vessels with < 2 voxels it is not possible to exactly extract the thin centerline. In this study, the 3D thinning algorithm was used to extract the vessel skeleton, especially including small-diameter vessels with topology preserving aspect and simple gradual peeling. [70].

To reconstruct the vascular trees, Szymczak *et al.* proposed a forest to connect the persistent maxima with the short edges and improve the forest by applying simple geometric filters that trim short branches, fill gaps in blood vessels, and remove spurious branches from the vascular tree [71]. The simple geometry method filters and trims short branches based on Kruskal's MST algorithm. That method constructed the minimum forest that uses the edges to connect

the points in a 3D point set that are shorter than the given threshold. Figueiredo *et al.* performed geometrical reconstructions using points, especially curved reconstructions for planar cases [72]. The point set can be separated into clusters by removing atypically long edges from the MSTs. This paper proposes 2 heuristic criteria for determining when an edge is too long. One is a global criterion, which removes the edges in order of decreasing length. The other is a local criterion, which removes edges that are much longer than the average length of the neighboring edges.

## 3.3 ARTERY AND VEIN DECOMPOSITION

### 3.3.1 Overall workflow

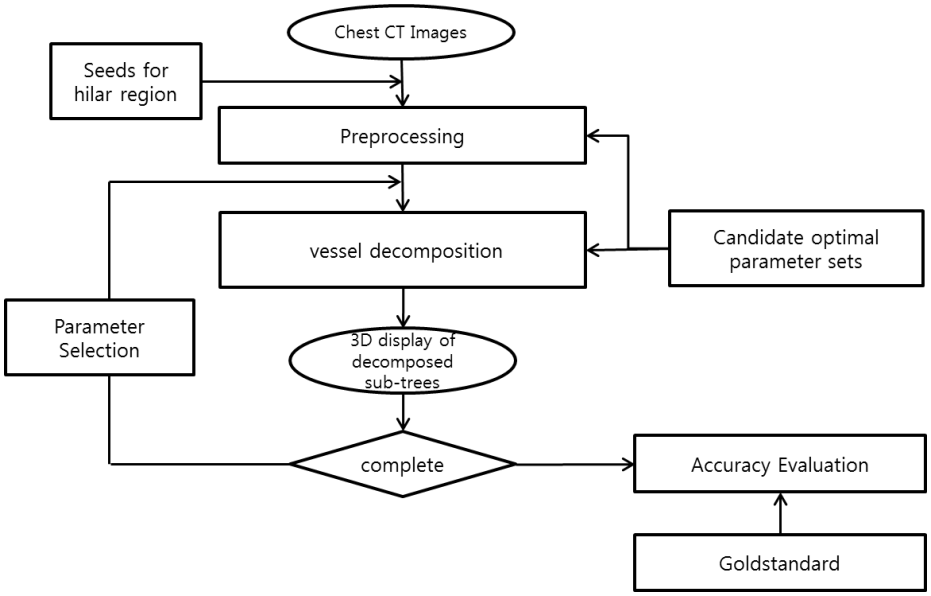


Figure 3-2. Flow chart of the overall procedure.

The overall procedure is shown in Figure 3-2, which included following parts: preprocessing, automatic vessel decomposition with roots automatically found for MST construction, accuracy evaluation on decomposed result by automatic classification through volumetric overlap with goldstandard. If the decomposed sub-trees were not complete, the vessel decomposition procedure was tried again with new parameter set. Although the hilar region could be detected

automatically, the detection of rough boundary of the hilar region frequently needs four or five candidate points around hilar region manually selected in 2D view.

### 3.3.2 Preprocessing

For pulmonary artery and vein decomposition, the preprocessing procedure included the following 4 major steps: 1) vessel segmentation; 2) initial tree construction; 3) statistical evaluation of the trees; and 4) construction of the first-level MST.

#### 3.3.2.1 Vessel segmentation

The vessel segmentation method was explained in a previous study [52]. Since the purpose of vessel decomposition is to quantify the separated arterial and venous subtrees, the simple threshold method was used to preserve the geometric features of the CT images.

The vessel structure was separately assessed for the left and right half-lungs. Airway segmentation and left-vs-right lung splits were performed using a previously described method [73-75]. Each half-lung was eroded in 3D with 2 pixels in

order to efficiently remove lung boundary noise because the intersecting objects between the lung mask and the vessel mask near the lung boundary could be included as noise under a given threshold. To segment the pulmonary vessels, an efficient approach that uses a threshold-based method with −750 Hounsfield Units (HU) on non-enhanced CT was used for the eroded lung region.

### 3.3.2.2 Initial tree construction

The vessel skeleton was extracted using the 3D thinning method. The vessel skeleton was created based on the spacing of the original image in order to prevent data loss. Since the threshold for the vessel segmentation was −750 HU, 3D thinning could be performed on the binary mask to extract the skeleton. In a later experiment, the skeleton threshold (SKTh) for extracting the subset from the vessel mask was selected based on the decomposition accuracy. After the skeleton was constructed using 26 connected neighborhoods, an undirected graph with nonnegative edge weights was constructed to evaluate their connectivity. Edges with 26 connectivity—composed of the center voxel and the neighboring voxels with a

distance weight—were linked if the vertexes of the edge were included in the skeleton mask. This edge construction was also computed on whole-vessel voxels. Edges were linked if the vertexes of the edge were included in the vessel mask. Two kinds of initial undirected graphs were used for statistical calculation and 2-level MST constructions.

The vertex weights of the initial undirected graph were calculated based on the previous study [52]. The weight is the average of 3 kinds of different weights: the attenuation intensity, the distance from the boundaries, and the Laplacian of the distance field. The normalization method was also performed on each weight in order to make the resulting value reside between 0 and 1. In this study, 2 types of MSTs were made for the skeleton vertexes and the whole-vessel voxels, which were compared with only 1 type of MST that was constructed using whole-vessel voxels in the previous study [52].

### 3.3.2.3 Subtree statistics

The radius was estimated by identifying the nearest neighboring boundary points of the vessel surface from the

skeleton, which could include ≥ 1 nearest points [76]. Therefore, a distance transformation was performed to estimate the vessel radius. The direction of each skeleton vertex was calculated based on the difference vector between the parent and current vertex. Estimating the radius and direction of each skeleton vertex is an error-prone process due to the discreteness of each skeleton vertex, so a smoothing procedure along each branch was performed to yield a more robust evaluation of the radius and directional data.

To distinguish each branch, a breadth-first search (BFS) was performed on each constructed skeleton MST. This search allowed the skeleton-subtrees to be divided into separate branches. In addition, the initial skeleton MST was constructed from the initial graph, and BFS was executed on this skeleton MST and the average values of the radius and direction of each skeleton vertex were calculated. After extracting the branch ID of each skeleton vertexes, the average values of radius and direction could be calculated.

### 3.3.2.4 The first level MST construction

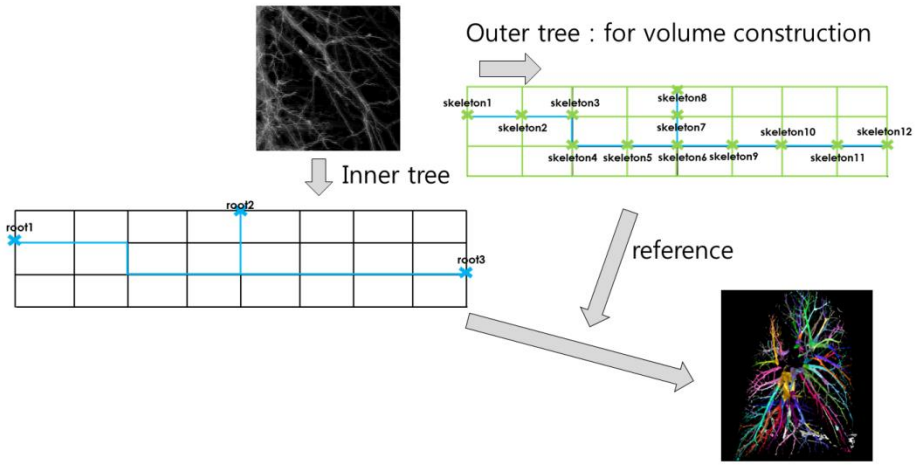


Figure 3-3. Two level minimum spanning tree constructions

Decomposition of the vessel subtrees was performed by 2-level construction of the MSTs. The construction of the MST with the skeleton vertexes as the target roots decomposed the vessel voxels into small fragments in the first level. In the second level, after constructing the MST on the skeleton graph with the automatically found roots, the decomposed small fragments of each skeleton vertex were combined based on the constructed second skeleton MSTs (Figure 3-3). The mapping table from the skeleton vertexes to either the surface or volume composed of the 3D points linked the skeleton vertexes to the small decomposed fragment of volume or surface.

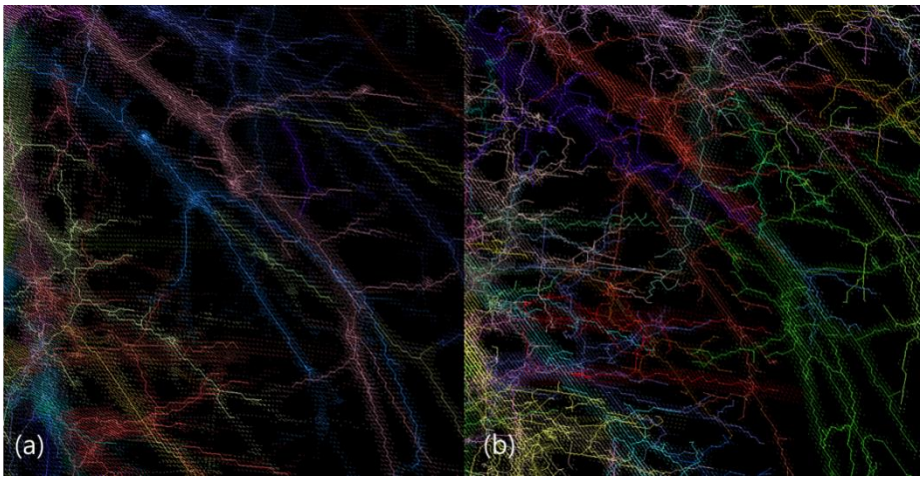


Figure 3-4. The skeleton graph and surface points mapped to that skeleton vertexes. (a) A part of pulmonary vessel region in the skeleton threshold of -550HU (b) The same vessel region with left figure in the skeleton threshold of -750HU.

When such data were available, a colored, textured vessel surface could be drawn. The surface points are shown in Figure 3-4, and the points of several colors represent points that were mapped using this procedure. The vertexes of the skeleton tree illustrated in Figure3-4 have corresponding surface points or volume points that were identified using this procedure. By identifying the voxels attached to a specific skeleton vertex, this map could be used for display, vessel selection, and the reconstruction of the vessels of selected

group IDs.

Cylinder construction around a vessel skeleton with a proper radius could be used to map the skeleton vertexes and vessel volume points. However, it can be difficult to identify the appropriate group for those voxels around a surface with a complex topology or bifurcating points. Importantly, the mapping table was made using MDijkstra, and this algorithm has strong characteristics for constructing the maps with such complex geometry. In addition, to determine the edges attached to a specific vertex, an incidence table was also used.

### 3.3.3 Root finding

The root-finding algorithm is important because the generation of the second-level MST would depend on the number and locations of the roots. To automatically identify roots in a given graph, the criteria to divide the graph must be considered. First, the connectivity of the graph could be used as a deciding factor for identifying root locations. This is, however, not enough because there could be unwanted connections. Among the pulmonary vessels, several vessels exist in 1

connected voxel object, while generally the vessel can be perceived from the morphology of the vessel’s structure. Therefore, a method for controlling this connectivity was proposed by filtering the edges. Unwanted roots can be removed using the proper filters with the optimal feature value set. The characteristics of the filter were made by considering vessel geometry and morphology, including vessel radius range, erosion number (ER) of the vessel mask, and additional thresholding on the vessel mask, which need to be optimized to control the connectivity of the graph and produce the proper roots. Additional size filtering of the connected object was performed to remove small objects using the total branch length (TBL). The number of the optimized feature value set in terms of filters, therefore, was 4.

The root-finding procedure includes edge filtering, size filtering of the connected object, and finding the roots from the connected object. To run this algorithm, a sequence of updated functions was performed as follows: 1) create an initial graph from the skeleton data; 2) filter the edges of the initial graph according to the selected features; 3) find the group; 4) filter the connected object based on TBL; 5) find the roots from the

important subset of vessel skeleton subtrees identified by filtering; and 6) run MDijkstra using the selected roots.

Size filtering worked in a different way in comparison with filtering the other features using the root-finding procedure. Figure 3-5 (e) shows skeleton trees that were filtered by size filtering. Figure 3-5(d) are the result of applying edge filtering with 3 selected features. Between procedures (2) and (4), there is "find group" procedure. After edge filtering for selected features, the groups for each skeleton-subtree were identified according to connectivity information. Figure 3-5(f) shows skeleton trees filtered by TBL. From these skeleton trees, the roots were calculated from the root candidate points, which were manually given.

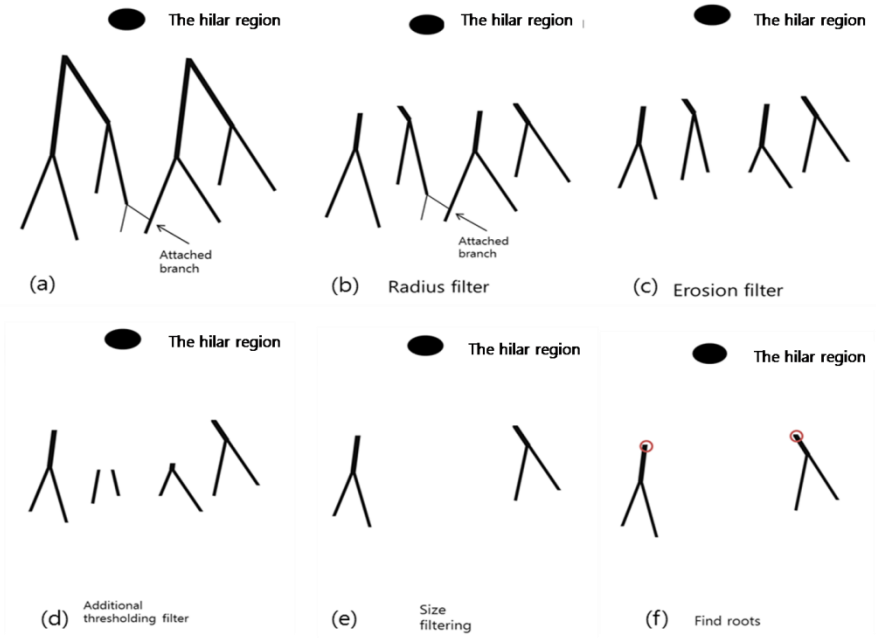


Figure 3-5. Sub-trees with distal branch attachment and automatic root finding procedure (a) Initial skeleton tree (b) skeleton trees after radius filter (c) skeleton trees after erosion filter (d) skeleton trees after additional thresholding filter (e) skeleton trees after size filtering (f) Root finding from the important subsets

The connected components of the dense voxels that label the resulting vessels are represented as $S_R = \{R_1, R_2, R_3, \ldots, R_{nR}\}$, and the root candidate points are represented as $RC = \{PC_1, PC_2, \cdots, PC_{nc}\}$. The distances between the point $R_x$ and the RC set were calculated by identifying the minimum point from the RC

point set. The point with the shortest distance from the RC point set among points $R_x$ was considered to be the root of the resulting vessel (Figure 3-5(c)). Basically, the root candidate points could be set as the hilar region points since the roots of the trees reside near the hilar region. But, especially, by using the manual split procedure, the root candidate points were set as the dividing skeleton vertexes since the split trees were made from the dividing points.

To more effectively tune the feature value set, an empirically selected feature value set could be given and a specific feature value set might be preferred based on the decomposition strategy.

### 3.3.4 Multi-root Dijkstra algorithm

The Dijkatra algorithm finds the MST for a weighted undirected graph [59]. Dijkstra algorithm's object grows from 1 source vertex into a tree of any size by adding vertices that are extracted from the priority queue, which can be used to divide the region into several parts based on the arrival timing of spanning tree construction under the given weight.

The connected objects of different groups could meet at 1

vertex. When this happened, MDijkstra removed the collided opposite edges to stop the growth of the opposite group object. The MDijkstra algorithm includes the collision detection algorithm by adding a line code (* in Figure 3-6) to solve this issue. This collision detection algorithm was brought from the mono-oriented group-growing algorithm[38]. This code searches for edges, including endpoints, and removes the identified edges from the maxHeap. Because the edges attached to the 1 vertex could be found by the incidence table, this line code could be executed without sequential searches. Since the binomial heap could perform combinations of insert, pop, and erase operations in O(nlogn) time ( 'n' is the object number) [58], the execution time of MDijkstra was bound to 3-4 minutes for the entire volume.

```
function MultiRootDijkstraAlgorithm(graph, source array,
 graph')
        group : -1 data array on each v
        parent : -1 data array on each v

        add sources to maxHeap.

        while maxHeap is not empty:
                pop edge e1 from maxHeap
                parent of e1.startpoint = e1.endpoint
                group[e1.endpoint] = group[e1.startpoint]
                add e1 to graph'

                remove edges including e1.endpoint from maxHeap *
                add unvisited neighbor e2 of e1.endpoint to maxHeap

        end while
        return graph'
end function
```

Figure 3-6. Multi-root Dijkstra algorithm. The input parameter *graph* is the initial graph of the vessels constructed using 26 connectivity. The input parameter *graph'* shows the vertexes structure without edges. NOTE * : code for considering multi-root.

The construction formula for MST can be found in Park *et al.*' s paper. In this paper, we redefined the construction formula for MST as a minimization problem in order to obtain a tree structure, T' = (V, E), that connects all of the vertices in V and whose construction energy (or cost) is minimized as Equation (3-1).

$$T' = \min_{T} C(T) \quad (3-1)$$

Because the set of vertices V is already given in this case, the construction energy is only affected by the connections of the edges. C(T) is then defined as the summation of the connecting energies of the edges, as shown as Equation (3-2).

$$C(T) = \sum_{(i,j)\in E} C(i,j) \qquad (3-2)$$

The construction energy of each edge connecting the *i-th* and *j-th* vertices is defined by Equation (3-3).

$$C(i,j) = \frac{\left\| v_j - v_i \right\|}{\alpha + \beta w_j + \gamma e_{ij} + \eta p_j} \qquad (3-3)$$

where, C(i,j) is the construction energy of each edge connecting the *i-th* and *j-th* vertices, $v_i$ and $v_j$ are the vertex position vectors, $w_j$ is the weight of vertex j, and $e_{ij}$ is the direction weight of edge(i,j) to a local orientation vector of vertex j. $p_j$ is the penalty weight of vertex j. $\alpha, \beta, \gamma, \eta$ (> 0) are positive real-value constants defined by the user, especially $\alpha$ must have a denominator $\neq 0$, and we set $\alpha = 1/5$, $\beta = 3/5$, $\gamma = 1/5$, and $\eta = 3/5$ for the skeleton vertexes used in the second level MST construction. In the first level MST construction case, we set $\alpha = 1/5$, $\beta = 3/5$, $\gamma = 0$, and $\eta = 0$.

The weight of the edge’s direction and the penalty weight were additionally adapted for the skeleton MST construction. The weight of the edge’s direction was calculated by the dot product of the average direction and the local edge direction. The penalty weight was calculated as the distance of the current vertex from the nearest points of the important subsets. This weight was made by MAX(0,1−dist/30 mm). This weight was the penalty that prevented a far point from the important subsets from being reached earlier by MDijkstra than a near point. The weight of the edge’s direction and the penalty weight were combined with the total weight by multiplication with the proper constants in Equation (3−3).

## 3.4 AN EFFICIENT DECOMPOSITION METHOD

For skeleton generation and a root−finding method, the candidate optimal feature value set could reduce the time and yield a more consistent feature value set.

### 3.4.1 Finding a candidate optimal feature value set

The automatic vessel decomposition procedure shown in Figure 3-2 was performed using a root-finding method and 2-level MST constructions. The vessel decomposition required 5 features and, since the lower radius limit (LR) was fixed at 0, the 5 optimal values of the 5features—including the upper radius limit (UR) for the vessel radius, TBL to remove small tree off, ER of the vessel mask, the additional threshold (ATh), and skeleton threshold (SKTh)—were tried by the grid-search method. Two features of the vessel, radius range and TBL, are related to the global shape of the skeleton of the vessel. Since the radius of the vessel tree decreases from the root to the distal branch, the radius range with LR of 0 value is an effective feature for tree decomposition. ER and ATh are the local shape features of the vessel skeleton since these features are not directly related to the change in the length of the vessel tree.

The optimal value was searched with LR, UR, TBL, ER and ATh under SKTh of -550HU by a particle swarm optimizer[74] of 10 particles and 10 iterations. For the prior knowledge, experiments were performed to find initial variables and a

search order. In these experiments, the optimal value for the optimizer to find was [0±0 mm, 1.70±0.55 mm, 13.83±10.80 mm, 1.1±0.85, and −176.42±151.17 HU for LR, UR, TBL, ER, and ATh respectively]. The optimal accuracy and decomposed vessel number of the pulmonary vessels were 89.34 ± 5.55% and 130 ± 107.42, respectively. In this experiment, the mean and standard deviation values of the decomposed vessel number were high. In addition, the local shape features showed large variance values compared with the global features. If the search-dimension of the particle swarm optimizer were large, the optimality of the search would be decreased.

In the field experiment, TBL and ATh were initially assumed to be 10 mm and −550 HU, respectively. To flexibly determine the feature values, a particle swarm optimizer with 10 particles and an iteration number of 10—which imitated interactive selection by the program operator—was used. If the grid number of the found axis were defined as *gn*, and the particle swarm optimizer was executed by the number of 10 x 10 x *gn* since the particle was 10 and the iteration was 10. The total test number of proposed grid search per each half-lung was 1908 times. This value could be calculated by summation

of 5x100(step 1), 6x100(step2), 5x100(step3), 3x100(step4), and 8(step5).This grid search proceeded in the following order: UR(step1), SKTh(step2), TBL(step3), ER(step4), and ATh(step5). For the optimizer's operation, the range of the feature values of ER and ATh were restricted between 0 and −750HU, and 2 and −100HU, respectively. Two local feature values could be varied at the same time, or only ATh could be varied by the optimizer for the grid−search time of ER.

A deterministic optimizer, such as the quasi−Newton method, could not be used to calculate the stable optimal value because the gradient value was not useful for evaluating the vessel decomposition algorithm. Therefore, a stochastic algorithm, which simulates the social behavior of a "flock of birds" or "school of fish", was used. The cost function of this optimizer minimizes the error value of arterial and venous decomposition.

### 3.4.2 Comparison with previous method

Park *et al*'s method was executed with the proposed automatic root−finding method to compare performance. The decomposition accuracies of Park *et al*'s method and this

proposed method were compared. These 2 methods have the same vertex weights. For comparison, SPSS 17.0 (Armonk, New York) was used to generate descriptive statistics and perform paired *t* tests with 2 tails.

## 3.5 EVALUATION

### 3.5.1 Accuracy evaluation

Let $T_a$ and $T_v$ denote the true segmentations of the arterial and venous subtrees, respectively, in the 20 half-lungs of the 10 patients with COPD. $S_a$ and $S_v$ denote the segmentations of the arteries and veins, respectively, that were computed using the current method. Since the decomposition results of the proposed method contain no classification information for the separated subtrees, the subtree was automatically classified as the arterial or venous subtree using the gold standard in order to calculate the decomposition accuracy. The automatic classification criterion is the area that overlaps with $T_a$ and $T_v$ in each subtree. After that, $S_a$ and $S_v$ can be calculated (Figure 3-7).

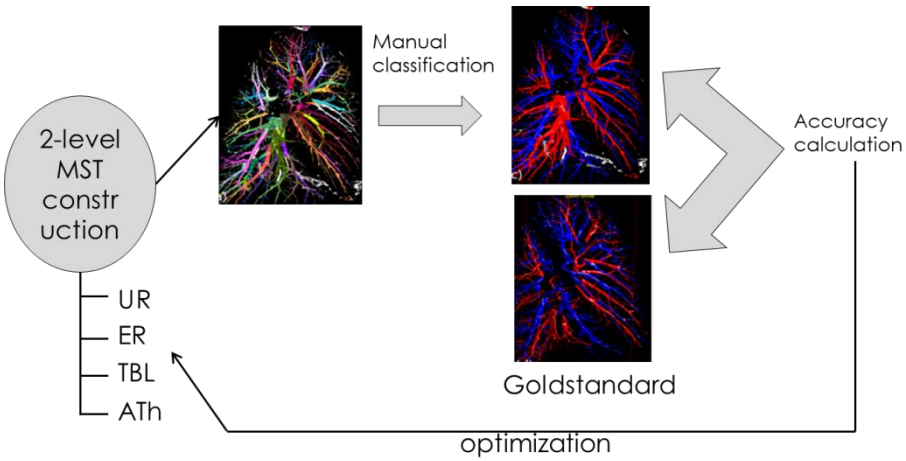


Figure 3-7. Accuracy evaluation of decomposition under optimization procedure

The gold standard mask used in our current report was generated using a sub-millimeter-thick, non-contrast, volumetric chest CT (the patient's breath was held at full inspiration) for the 10 patients with COPD. The hilar region was manually removed to separate the arteries and veins. An expert with > 10 years of experience generated the gold standards for the arterial and venous vessels for these 10 patients. Descriptive statistics of the arteries and veins of the gold standards were as follows: the mean and standard deviations of the lower radius, upper radius, lower distance, and upper distance were 0.33 ± 0.01 mm, 3.13 ± 0.55 mm, 14.59 ±

3.00 mm, and 180.75 ± 17.96 mm, respectively. The upper range value of the radius was relatively low because the gold standard did not contain the hilar region.

The accuracy and error of the computerized decomposition of the artery and vein were defined as follows.

$$Accuracy = \frac{(T_a \cap S_a) \cup (T_v \cap S_v)}{T_a \cup T_v} \qquad (3-4)$$

and

$$Error = \frac{(T_a \cap S_v) \cup (T_v \cap S_a)}{T_a \cup T_v} \qquad (3-5)$$

Since the gold standard was made by removing the hilar region, the resulting vessel mask is different from the gold standard, and the hilar region also was excluded from the accuracy calculation.

### 3.5.2 Determining the pseudo-optimal feature value set

In Table 3-1, step 1 shows the averaged decomposition results of the 20 half-lungs under the optimal UR searched by varying the UR value from 1 mm to 3 mm in 0.5-mm steps. In each half-lung case, after the optimal value and its

corresponding error (or accuracy) value were recorded, the recorded values were averaged over 20 half-lungs. The grid-search results show that when the upper radius value was low, the accuracy was high but the decomposed vessel number was high. In the grid-search experiment, we found that the value between 1.5 mm and 2.0 mm was optimal. Therefore, in the next grid-search step, 1.75 mm was used as the UR. In step 2, the optimal SKTh value was searched by varying a value from -500 HU to -750 HU in 50-HU steps. SKTh was used to determine the length of the vessel skeleton. With a high threshold value, the constructed vessel skeleton is shorter and contains the core part of the vessel. Figures 3-4 (a) and (b) compare the skeletons made with thresholds of -550 HU and -750HU. In the grid-search experiment, -550 HU was determined as the best SKTh value. For step 3, the optimal TBL was found by varying TBL from 10 mm to 30 mm in 5-mm steps with the grid search. If TBL increases, the decomposed vessel number decreases. Fifteen millimeters was used as the optimal TBL value. Step 4 is to find the optimal ER by varying it from 0 to 2 in 1 step. In this experiment, 1 was the optimal parameter. Finally, in step 5, the optimal ATh was

searched by varying ATh between −100 HU and −750 HU. The optimal parameter set was [0 mm, 1.75 mm, 15 mm, 1, −100HU, and −550HU for LR, UR, TBL, ER, ATh, and SKTh, respectively]. In this optimal set, the optimal accuracy and decomposed vessel number of the pulmonary vessels were 89.71 ± 3.76% and 75.1 ± 15.12, respectively. This value could be compared with the methods of the other steps (Table 3−1). The other methods, except the second method of step 1, were significantly more accurate ($p< 0.001$) in comparison with the optimal method in terms of accuracy and error terms. However, all other methods demonstrated significantly larger vessel numbers ($p< 0.05$) in comparison with the optimal method.

TABLE 3−1. Sequential grid search results from steps 1-5. The determined optimal values for each step are underlined. Each row shows the averaged decomposition results of the 20 half−lungs of 10 CT scans for the given 6 feature values. One or 2 of the possible values for the erosion

number and the additional threshold have flexibility to vary by an optimizer from steps 1–4.

| **Step** | **$N_{sep}$** | **Accu (%)** | **Error (%)** | **LR (mm)** | **UR (mm)** | **TBL (mm)** | **ER** | **ATh (HU)** | **SKTh (HU)** |
|---|---|---|---|---|---|---|---|---|---|
| **1** | 140.60±44.50*** | 93.36±2.49*** | 6.64±2.49*** | 0 | **1.5** | 10 | 0.65±0.67 | -241.12±119.46 | -550 |
| **1** | 98.20±31.29*** | 90.79±4.00 | 9.21±4.00 | 0 | **2** | 10 | 1.65±0.59 | -210.04±137.05 | -550 |
| **2** | 116.5±43.64*** | 92.34±2.88*** | 7.66±2.88*** | 0 | 1.75 | 10 | 1.84±1.03 | -221.74±134.14 | **-550** |
| **3** | 89.3±32.43* | 91.26±3.28*** | 8.74±3.28 | 0 | 1.75 | **15** | 0.85±0.75 | -214.76±135.73 | -550 |
| **4** | 93.1±32.49** | 91.25±3.22*** | 8.75±3.22*** | 0 | 1.75 | 15 | **1** | -217.31±144.02 | -550 |
| **5** | 75.1±15.12 | 89.71±3.76 | 10.29±3.76 | 0 | 1.75 | 15 | 1 | **-100** | -550 |

Note: $N_{sep}$, separated vessel number; Accu, accuracy; LR, lower radius; UR, upper radius; TBL, total branch length; ER, erosion number; ATh, the additional threshold; SKTh, the skeleton threshold

All $p$ values are derived from paired $t$ tests comparing the method of step 5 with the methods of the other steps.

*$p < 0.05$, **$p < 0.01$, ***$p < 0.001$.

The execution time of the second-level MST construction with the automatic root-finding procedure was found to be 3.58 ± 0.65 seconds using native voxel spacing. Additionally, the creation time for the mapping table between the skeleton vertexes and volume voxels was 234.55 ± 90.87 seconds with native voxel spacing. This was the execution time for the first level MST construction. This program was executed using an Intel Core i7 computer with 16-GB memory on a 64-bit Microsoft Windows 7 operating system.

### 3.5.3 Comparison with previous method

For the feature value set of [0 mm, 1.75 mm, 15 mm, 1, -100 HU, -550 HU], the decomposition accuracy and decomposed vessel number of pulmonary vessels of Park *et al*'s method were 83.77 ± 5.22% and 75.1 ± 15.12, respectively (Table 3-2), in comparison with 89.71 ± 3.76% and 75.1 ± 15.12 using the proposed method, thereby demonstrating significantly better accuracy ($p < 0.001$).

Table 3-2. Average decomposition results of the 20 half-lungs of 10 CT scans between the proposed method and the previous method

| Var (HU) | $N_{sep}$ | Accu (%) | error (%) | LR (mm) | UR (mm) | TBL (mm) | ER | ATh (HU) | SKTh (HU) |
|---|---|---|---|---|---|---|---|---|---|
| **Proposed** | 75.1±15.12 | 89.71±3.76 | 10.29±3.76 | 0 | 1.75 | 15 | 1 | -100 | -550 |
| **Previous** | 75.1±15.12 | 83.77±5.22*** | 16.23±5.22*** | 0 | 1.75 | 15 | 1 | -100 | -550 |

Note: $N_{sep}$, separated vessel number; Accu, accuracy; LR, lower radius; UR, upper radius; TBL, total branch length; ER, erosion number; ATh, the additional threshold; SKTh, the skeleton threshold

All $p$ values were derived from paired $t$ tests comparing the previous method with the proposed method.

*$p$ < 0.05, **$p$< 0.01, ***$p$< 0.001.

## 3.5.4 Four half-lung cases

Figures 3-8 and 3-9 show decomposition examples of 4 half-lungs. These results came from the feature value set [0 mm, 1.75 mm, 15 mm, 1, -100 HU, -550 HU]. This optimal value set did not need interactive adjustment and could be

applied directly for vessel decomposition. The second column of both figures shows the classified results from the decomposition results. The comparison between the second and third columns could give the perception of this algorithm's accuracy. The second half-lung of Figure 3-9 shows the worst case among 20 decomposed half-lungs.

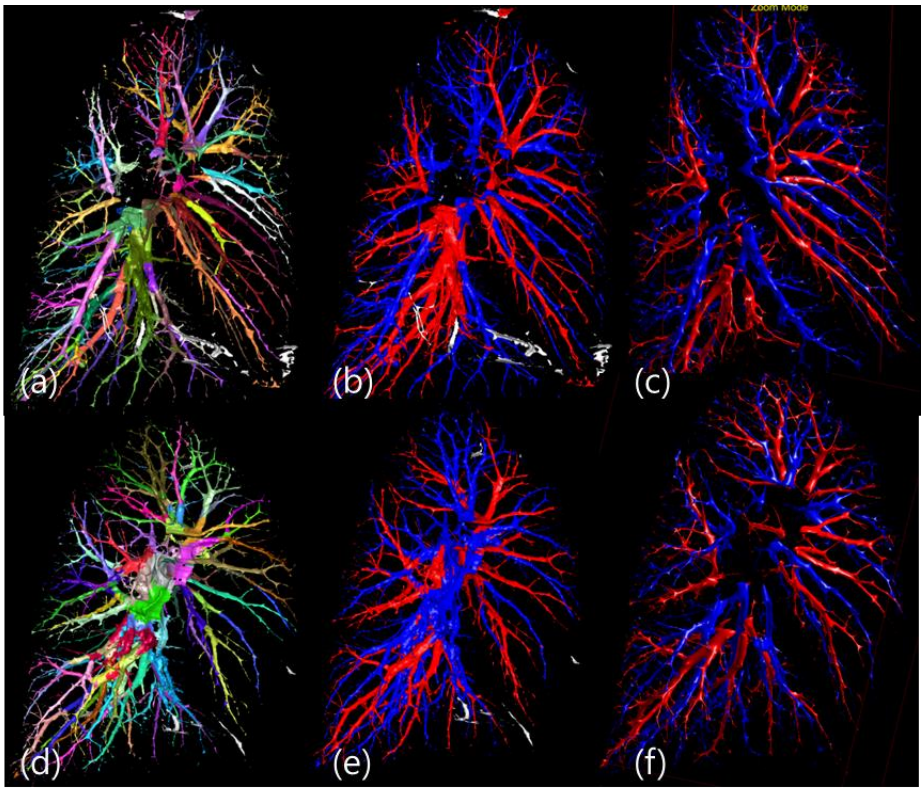


Figure 3-8. Two examples of decomposition of two half-lungs. Arteries are shown in blue and veins are shown in red. (a) Decomposition result of the first half-lung (b) The classified artery and vein result after classification of decomposition result

with goldstandard (Accuracy = 96.16%) (c) Goldstandard (d) Decomposition result of the second half-lung (e) The classified artery and vein (Accuracy = 93.89%) (f) Goldstandard

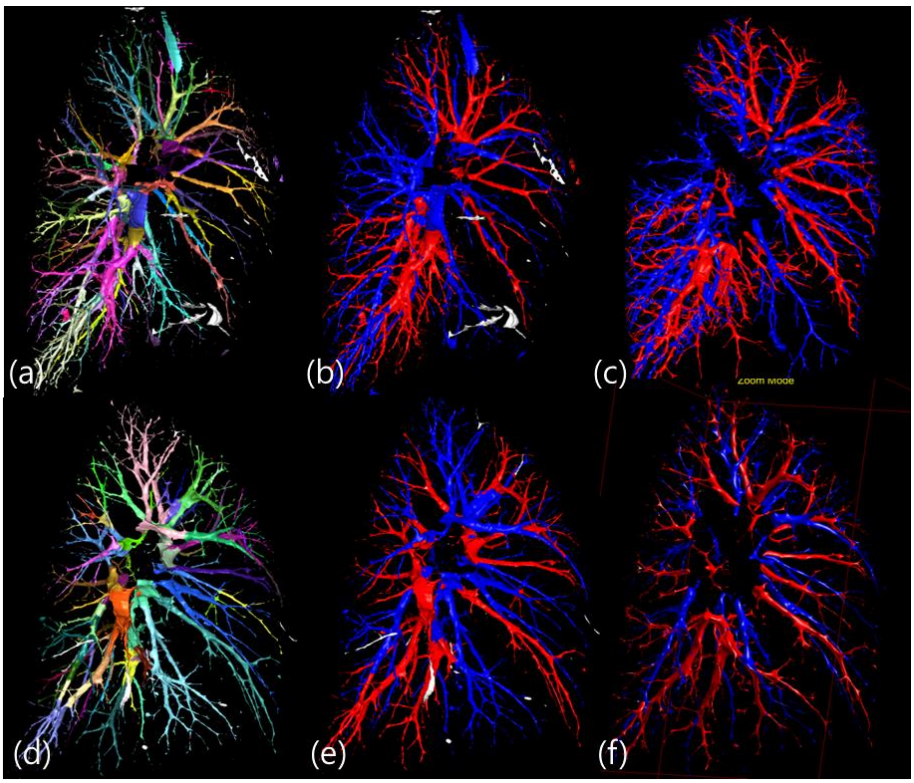


Figure 3-9. Two examples of decomposition of two half-lungs. Arteries are shown in blue and veins are shown in red. (a) Decomposition result of the first half-lung (b) The classified artery and vein result after classification of decomposition result with goldstandard (Accuracy = 92.03%) (c) Goldstandard (d) Decomposition result of the second half-lung (e) The classified artery and vein (Accuracy = 79.54%) (f) Goldstandard.

## 3.6 DISCUSSION AND CONCLUSION

We developed and validated the semiautomatic decomposition framework based on 2-level MST constructions for non-enhanced volumetric chest CT. This decomposition framework adapted the automatic root-finding method through 2 filters composed of edge filtering and size filtering. Through the experimental analysis of 5 features, the pseudo-optimal feature value set was determined for the automatic execution of decomposition. This decomposition framework could be used to differentiate the pulmonary arterial and venous subtrees with high accuracy and efficiency.

Quantification based on the classification of the arteries and veins could give us a tool for the development of imaging biomarkers for lung disease, which would be more important due to its noninvasiveness and relatively low economic cost. In addition, using this method, automatic differentiation of the pulmonary arteries and veins could be developed based on various features of the morphological and topological analyses of the pulmonary skeleton-subtrees.

It was challenging to determine the degree of invasion by

any branch into another tree and quantify the decomposition accuracy of the vessels, if it was dealt without the automatic classification under the artery and vein gold standards. However, it was also difficult to make gold standards only for decomposition. Saha *et al.* quantified the classification accuracy using the same strategy as our method [64]. However, their method put the seed with the label of the artery and vein. Therefore, the method did not need the classification procedure. In contrast, because our method adapted the automatic root-finding procedure, there was no information about the arterial or venous label. Therefore, automatic classification under the gold standards needed to be performed to calculate the decomposition accuracy. We quantitatively evaluated the decomposition accuracies of the vessels based on the gold standards, which would be useful for the further development of arterial and venous differentiation algorithms.

Although it yielded a satisfactory results, with an accuracy of around 90%. By interactively selecting feature value sets, our method could provide better results. The accuracy of 89.71% could be significantly increased if 2 local features were optimized for each half-lung. In the specific case of feature

value set optimization, the worst accuracy of the half-lung case with the final feature value set was 79.54% with a decomposed vessel number of 53 (the second case of Figure 3-9). But this half-lung case's accuracy could be increased to 89.14% with a decomposed vessel number of 113 when the feature value set was changed from [0 mm, 1.5 mm, 10 mm, 1, -100 HU, -550 HU] to [0 mm, 1.5 mm, 10 mm, 1, -285 HU, -550 HU]. Therefore, we need to develop a more robust optimization scheme.

In addition, extending the feature settings to the other features of the pulmonary vessel morphology and topology could improve the accuracy of the decomposition. Furthermore, we need more quantitative criteria to validate the decomposition results.

In conclusion, our proposed semiautomatic decomposition framework based on 2-level MST constructions could differentiate the arterial and venous subtrees with high efficiency. In the future, this algorithm could be clinically useful for the automated classification of the pulmonary arteries and veins.

# REFERENCES


1. Caban, J.J., Joshi, A., and Nagy, P. (2007). Rapid development of medical imaging tools with open-source libraries. Journal of Digital Imaging *20*, 83-93.
2. Erickson, B.J., Langer, S., and Nagy, P. (2005). The role of open-source software in innovation and standardization in radiology. Journal of the american college of radiology *2*, 927-931.
3. (2015). The Visualization Toolkit (VTK). (http://pulbic.kitware.com/VTK/(url)).
4. Bitter, I., Van Uitert, R., Wolf, I., Ibanez, L., and Kuhnigk, J.-M. (2007). Comparison of four freely available frameworks for image processing and visualization that use ITK. Visualization and Computer Graphics, IEEE Transactions on *13*, 483-493.
5. (2015). The Insight Toolkit (ITK). (http://www.itk.org).
6. Xu, Y., Sonka, M., McLennan, G., Guo, J., and Hoffman, E. (2006). MDCT-based 3-D texture classification of emphysema and early smoking related lung pathologies. Medical Imaging, IEEE Transactions on *25*, 464-475.
7. (1982). Medical Imaging and Interpretation (ISMII). In Proc. Int'l Symp. pp. 1-607.
8. Kass, M., Witkin, A., and Terzopoulos, D. (1988). Snakes: Active contour models. International journal of computer vision *1*, 321-331.
9. Koenderink, J.J. (1984). The structure of images. Biological cybernetics *50*, 363-370.
10. Maeda, K., Utsu, M., and Kihaile, P.E. (1998). Quantification of sonographic echogenicity with grey-level histogram width: a clinical tissue characterization. Ultrasound in medicine & biology *24*, 225-234.
11. Cohen, L.D., and Cohen, I. (1993). Finite-element methods for active contour models and balloons for 2-D and 3-D images. Pattern Analysis and Machine Intelligence, IEEE Transactions on *15*, 1131-1147.
12. Cootes, T.F., Taylor, C.J., Cooper, D.H., and Graham, J. (1995). Active shape models-their training and application. Computer vision and image understanding *61*, 38-59.
13. Osher, S., and Sethian, J.A. (1988). Fronts propagating with curvature-dependent speed: algorithms based on Hamilton-Jacobi formulations. Journal of computational physics *79*, 12-49.
14. Withey, D., and Koles, Z. (2007). Medical image segmentation: Methods and software. In Noninvasive Functional Source Imaging of the Brain and Heart and the International Conference on Functional Biomedical Imaging, 2007. NFSI-ICFBI 2007.

Joint Meeting of the 6th International Symposium on. (IEEE), pp. 140-143.
15. Iacobellis, G., Pistilli, D., Gucciardo, M., Leonetti, F., Miraldi, F., Brancaccio, G., Gallo, P., and di Gioia, C.R. (2005). Adiponectin expression in human epicardial adipose tissue in vivo is lower in patients with coronary artery disease. Cytokine *29*, 251-255.
16. Dey, D., Nakazato, R., Li, D., and Berman, D.S. (2012). Epicardial and thoracic fat-Noninvasive measurement and clinical implications. Cardiovascular Diagnosis and Therapy *2*, 85-93.
17. van den Borst, B., Gosker, H.R., and Schols, A.M. (2013). Central fat and peripheral muscle: partners in crime in chronic obstructive pulmonary disease. American journal of respiratory and critical care medicine *187*, 8-13.
18. Dey, D., Wong, N.D., Tamarappoo, B., Nakazato, R., Gransar, H., Cheng, V.Y., Ramesh, A., Kakadiaris, I., Germano, G., Slomka, P.J., et al. (2010). Computer-aided non-contrast CT-based quantification of pericardial and thoracic fat and their associations with coronary calcium and Metabolic Syndrome. Atherosclerosis *209*, 136-141.
19. Rosenquist, K.J., Pedley, A., Massaro, J.M., Therkelsen, K.E., Murabito, J.M., Hoffmann, U., and Fox, C.S. (2013). Visceral and subcutaneous fat quality and cardiometabolic risk. JACC. Cardiovascular imaging *6*, 762-771.
20. Furutate, R., Ishii, T., Wakabayashi, R., Motegi, T., Yamada, K., Gemma, A., and Kida, K. (2011). Excessive visceral fat accumulation in advanced chronic obstructive pulmonary disease. International journal of chronic obstructive pulmonary disease *6*, 423-430.
21. Vaes, A.W., Franssen, F.M., Meijer, K., Cuijpers, M.W., Wouters, E.F., Rutten, E.P., and Spruit, M.A. (2012). Effects of body mass index on task-related oxygen uptake and dyspnea during activities of daily life in COPD. PloS one *7*, e41078.
22. van den Borst, B., Gosker, H.R., Koster, A., Yu, B., Kritchevsky, S.B., Liu, Y., Meibohm, B., Rice, T.B., Shlipak, M., Yende, S., et al. (2012). The influence of abdominal visceral fat on inflammatory pathways and mortality risk in obstructive lung disease. The American journal of clinical nutrition *96*, 516-526.
23. Zhang, J., He, Z., and Huang, X. (2011). Automatic 3D Anatomy-based Mediastinum Segmentation Method in CT Images. JDCTA *5*, 266~274.
24. Chittajallu, D., Balanca, P., and Kakadiaris, I. (2009). Automatic delineation of the inner thoracic region in non-contrast CT data. Engineering in Medicine and Biology Society, 2009. EMBC 2009. Annual International Conference of the IEEE, 3569-3572.

25. Zhou, X., Ninomiya, H., Hara, T., Fujita, H., Yokoyama, R., Chen, H., Kiryu, T., and Hoshi, H. (2008). Automated estimation of the upper surface of the diaphragm in 3-D CT images. Ieee T Bio-Med Eng *55*, 351-353.
26. Yalamanchili, R., Chittajallu, D., Balanca, P., Tamarappoo, B., Berman, D., Dey, D., and Kakadiaris, I. (2010). Automatic segmentation of the diaphragm in non-contrast CT images. Biomedical Imaging: From Nano to Macro, 2010 IEEE International Symposium on, 900-903.
27. Rangayyan, R.M., Vu, R.H., and Boag, G.S. (2008). Automatic Delineation of the Diaphragm in Computed Tomographic Images. J Digit Imaging *21*, S134-S147.
28. Li, K., Wu, X.D., Chen, D.Z., and Sonka, M. (2006). Optimal surface segmentation in volumetric images - A graph-theoretic approach. Ieee T Pattern Anal *28*, 119-134.
29. Zheng, Y.F., Barbu, A., Georgescu, B., Scheuering, M., and Comaniciu, D. (2008). Four-Chamber Heart Modeling and Automatic Segmentation for 3-D Cardiac CT Volumes Using Marginal Space Learning and Steerable Features. Ieee T Med Imaging *27*, 1668-1681.
30. Funka-Lea, G., Boykov, Y., Florin, C., Jolly, M.-P., Moreau-Gobard, R., Ramaraj, R., and Rinck, D. (2006). Automatic heart isolation for CT coronary visualization using graph-cuts. Biomedical Imaging: Nano to Macro, 2006. 3rd IEEE International Symposium on, 614-617.
31. Zheng, Y., Vega-Higuera, F., Zhou, S.K., and Comaniciu, D. (2010). Fast and automatic heart isolation in 3D CT volumes: Optimal shape initialization. In Machine Learning in Medical Imaging. (Springer), pp. 84-91.
32. Leventon, M.E., Grimson, W.E.L., and Faugeras, O. (2000). Statistical shape influence in geodesic active contours. Computer Vision and Pattern Recognition, 2000. Proceedings. IEEE Conference on *1*, 316-323.
33. Kiraly, A.P., Higgins, W.E., McLennan, G., Hoffman, E.A., and Reinhardt, J.M. (2002). Three-dimensional human airway segmentation methods for clinical virtual bronchoscopy. Academic radiology *9*, 1153-1168.
34. Mori, K., Hasegawa, J., Toriwaki, J., Anno, H., and Katada, K. (1996). Recognition of bronchus in three-dimensional X-ray CT images with applications to virtualized bronchoscopy system. Pattern Recognition, 1996., Proceedings of the 13th International Conference on *3*, 528-532.
35. Hedlund, L., Anderson, R., Goulding, P., Beck, J., Effmann, E., and Putman, C. (1982). Two methods for isolating the lung area of a CT scan for density information. Radiology *144*, 353-357.

36. Kalender, W.A., Fichte, H., Bautz, W., and Skalej, M. (1991). Semiautomatic evaluation procedures for quantitative CT of the lung. Journal of computer assisted tomography *15*, 248.
37. Lee, Y.J., Lee, M., Kim, N., Seo, J.B., and Park, J.Y. (2013). Automatic Left and Right Lung Separation Using Free-formed Surface Fitting on Volumetric CT. submitted, .
38. Xie, H., McDonnell, T., and Qin, H. (2004). Surface reconstruction of noisy and defective data sets. In Visualization, 2004. IEEE. (IEEE), pp. 259-266.
39. D'Errico, J. Surface Fitting using gridfit - File Exchange - MATLAB Central. ([Online] Available: http://www.mathworks.com/matlabcentral/fileexchange/8998 [Accessed: 14-Oct-2013]).
40. Lay, D.C. Linear Algebra and its Applications. 2000. (Addison-Wesley/Longman, New York/London).
41. Bae, J.P., Kim, N., Kim, J.-E., Chang, Y., Lee, S.M., Seo, J.B., Lee, J., and Kim, H.C. (2013). Automatic Lung Segmentation for High-Resolution Computed Tomography of Patients with Diffuse Interstitial Lung Disease Using a Rib Detection and Inverse Level Set Algorithm. Submitted, .
42. Fabbri, R., Costa, L.D.F., Torelli, J.C., and Bruno, O.M. (2008). 2D Euclidean distance transform algorithms: A comparative survey. ACM Computing Surveys (CSUR) *40*, 2.
43. Bailey, D. (2005). An efficient euclidean distance transform. Combinatorial Image Analysis, 394-408.
44. Lorensen, W.E., and Cline, H.E. (1987). Marching cubes: A high resolution 3D surface construction algorithm. ACM Siggraph Computer Graphics *21*, 163-169.
45. Sethian, J.A. (1999). Level set methods and fast marching methods: evolving interfaces in computational geometry, fluid mechanics, computer vision, and materials science, Volume 3, (Cambridge university press).
46. Malladi, R., Sethian, J.A., and Vemuri, B.C. (1995). Shape Modeling with Front Propagation - a Level Set Approach. Ieee T Pattern Anal *17*, 158-175.
47. Byrd, R.H., Lu, P.H., Nocedal, J., and Zhu, C.Y. (1995). A Limited Memory Algorithm for Bound Constrained Optimization. Siam J Sci Comput *16*, 1190-1208.
48. Mount, D.M., and Arya, S. ANN: A Library for Approximate Nearest Neighbor Searching ([Online] Available: http://www.cs.umd.edu/~mount/ANN/ [Accessed: 14-Oct-2013]).
49. Van Ginneken, B., Heimann, T., and Styner, M. (2007). 3D segmentation in the clinic: A grand challenge. 3D segmentation in the clinic: a grand challenge, 7-15.

50. Palagyi, K., Tschirren, J., and Sonka, M. (2003). Quantitative analysis of three-dimensional tubular tree structures. In Proceedings of the International Conference on Information Processing in Medical Imaging (IPMI), C. Taylor and J.A. Noble, eds. (Ambleside, UK: Springer Verlag), pp. 222-233.
51. Estépar, R.S.J., Ross, J.C., Russian, K., Schultz, T., Washko, G.R., and Kindlmann, G.L. (2012). Computational vascular morphometry for the assessment of pulmonary vascular disease based on scale-space particles. Proceedings / IEEE International Symposium on Biomedical Imaging: from nano to macro. IEEE International Symposium on Biomedical Imaging, 1479-1482.
52. Park, S., Lee, S.M., Kim, N.K., Seo, J.B., and Shin, H. (2013). Automatic reconstruction of the arterial and venous trees on volumetric chest CT. Med. Phys. *40*, 071906.
53. Matsuoka, S., Washko, G.R., Dransfield, M.T., Yamashiro, T., San Jose Estepar, R., Diaz, A., Silverman, E.K., Patz, S., and Hatabu, H. (2010). Quantitative CT measurement of cross-sectional area of small pulmonary vessel in COPD: correlations with emphysema and airflow limitation. Acad. Radiol. *17*, 93-99.
54. Uejima, I., Matsuoka, S., Yamashiro, T., Yagihashi, K., Kurihara, Y., and Nakajima, Y. (2011). Quantitative computed tomographic measurement of a cross-sectional area of a small pulmonary vessel in nonsmokers without airflow limitation. Jpn J Radiol *29*, 251-255.
55. Estepar, R.S., Kinney, G.L., Black-Shinn, J.L., Bowler, R.P., Kindlmann, G.L., Ross, J.C., Kikinis, R., Han, M.K., Come, C.E., Diaz, A.A., et al. (2013). Computed tomographic measures of pulmonary vascular morphology in smokers and their clinical implications. Am. J. Respir. Crit. Care Med. *188*, 231-239.
56. Park, S.Y., Lee, S.M., Kim, N.K., Seo, J.B., and Choi, J.H. (2013). Quantification of the Distribution and Extent of Automatically Classified Small Pulmonary Arteries and Veins on Volumetric Chest CT In 2013 Radiological Society of North America 99th Scientific Assembly and Annual Meeting. (McCormick Place, Chicago, USA).
57. Prim, R.C. (1957). Shortest connection networks and some generalizations. Bell Syst. Technical J. *36*, 1389-1401.
58. Cormen, T.H., Leiserson, C.E., Rivest, R.L., and Stein, C. (2003). Introduction to Algorithms, 3rd Edition, (Cambridge, MA: MIT Press).
59. Dijkstra, E.W. (1959). A note on two problems in connexion with graphs. Numer. Math. *1*, 269-271.
60. Livny, Y., Yan, F., Olson, M., Chen, B., Zhang, H., and El-Sana, J. (2010). Automatic reconstruction of tree skeletal structures

from point clouds. ACM Transactions on Graphics (TOG) *29*, 151.
61. Buelow, T., Wiemker, R., Blaffert, T., Lorenz, C., and Renisch, S. (2005). Automatic extraction of the pulmonary artery tree from multi-slice CT data. Med. Imaging *5746*, 730-740.
62. Yonekura, T., Matsuhiro, M., Saita, S., Kubo, M., Kawata, Y., Niki, N., Nishitani, H., Ohmatsu, H., Kakinuma, R., and Moriyama, N. (2007). Classification algorithm of pulmonary vein and artery based on multi-slice CT image. Med. Imaging *6514*, 65142E-65142E-65148.
63. Lei, T., Udupa, J.K., Saha, P.K., and Odhner, D. (2001). Artery-vein separation via MRA-an image processing approach. Medical Imaging, IEEE Transactions on *20*, 689-703.
64. Saha, P.K., Gao, Z., Alford, S.K., Sonka, M., and Hoffman, E.A. (2010). Topomorphologic separation of fused isointensity objects via multiscale opening: separating arteries and veins in 3-D pulmonary CT. IEEE Trans. Med. Imaging *29*, 840-851.
65. Gao, Z., Grout, R.W., Holtze, C., Hoffman, E.A., and Saha, P.K. (2012). A New Paradigm of Interactive Artery/Vein Separation in Noncontrast Pulmonary CT Imaging Using Multiscale Topomorphologic Opening. Biomedical Engineering, IEEE Transactions on *59*, 3016-3027.
66. van Bemmel, C.M., Spreeuwers, L.J., Viergever, M.A., and Niessen, W.J. (2003). Level-set-based artery-vein separation in blood pool agent CE-MR angiograms. IEEE Trans. Med. Imaging *22*, 1224-1234.
67. Chowriappa, A., Seo, Y., Salunke, S., Mokin, M., Kan, P., and Scott, P. (2014). 3-D Vascular Skeleton Extraction and Decomposition. Biomedical and Health Informatics, IEEE Journal of *18*, 139-147.
68. Chowriappa, A., Salunke, S., Mokin, M., Kan, P., and Scott, P.D. (2013). 3D Vascular Decomposition and Classification for Computer-Aided Detection. Biomedical Engineering, IEEE Transactions on *60*, 3514-3523.
69. Bouix, S., Siddiqi, K., and Tannenbaum, A. (2005). Flux driven automatic centerline extraction. Med. Image Anal. *9*, 209-221.
70. Lee, T.C., Kashyap, R.L., and Chu, C.N. (1994). Building Skeleton Models Via 3-D Medial Surface Axis Thinning Algorithms. Cvgip-Graphical Models and Image Processing *56*, 462-478.
71. Szymczak, A., Stillman, A., Tannenbaum, A., and Mischaikow, K. (2006). Coronary vessel trees from 3D imagery: a topological approach. Med. Image Anal. *10*, 548-559.
72. De Figueiredo, L.H., and de Miranda Gomes, J. (1994). Computational morphology of curves. Vis Comput *11*, 105-112.

73. Black, M.J., and Rangarajan, A. (1996). On the unification of line processes, outlier rejection, and robust statistics with applications in early vision. Int J Comput Vis *19*, 57–91.
74. Kennedy, J. (2010). Particle swarm optimization. In Encyclopedia of Machine Learning, C. Sammut and G.I. Webb, eds. (New York: Springer), pp. 760–766.
75. Werneck, R.F. (2006). Design and analysis of data structures for dynamic trees. Volume PhD. (Princeton University).
76. Antiga, L. (2002). Patient-specific modeling of geometry and blood flow in large arteries. In Politecnico di Milano, Volume PhD. (Politecnico di Milano).

# 국문 초록

흉곽에 대한 컴퓨터 단층촬영 영상을 이용하여 흉강 분할 알고리즘과 폐 동맥 정맥 분리 알고리즘을 개발하고 그 성능을 평가하였다. 해당 연구는 흉곽 컴퓨터 단층 영상에서 임상적으로 의미 있는 장기를 분할하는 일을 자동화 했다는 점에서 중요하다. 장기 분할 정확성을 높이기 위해서 문턱값 방법을 기반한 형태적인 방법이나 연결성을 이용한 물체 선택 등의 기본적인 방법이 아닌, 좀 더 향상된 컴퓨터 공학적인 방법인 수치적인 방법과 그래프 이론을 이용한 방법을 처음으로 적용하였다. 본 논문에서는 위와 같이 제안된 새로운 연구 방법을 다음과 같은 두 가지 실례를 통해 시도하고 그 결과를 평가하였다.

첫번째 연구에서는 흉강을 분할 대상으로 하고 있다. 흉강은 흉강 벽과 횡경막에 의해 둘러 싸여 있는 장기를 말한다. 현재 본 연구가 대상으로 하고 있는 흉강의 경우 경계 부분에 변화가 큰 형태의 장기가 아니고 횡경막의 경우 얇은 두께의 막이기 때문에 그 형태가 컴퓨터 단층 영상 내에서 손실된 형태로 표현되어져 있는 경우가 많다. 종격동을 2 차원으로 찾는 것이라든지, 흉강벽과 횡경막을 따로 찾는 연구는 여러 연구에서 제시되어 있다. 하지만 흉강의 볼륨을 영상분할 하는 일에 대한 연구는 본 연구가 처음으로 제안을 하였다. 흉강 부피 관점에서 측정되는, 부피

겹치는 비율과 허위 양성 비율과 허위 음성 비율이 제안 방법은 98.17±0.84%, 0.49±0.23%, 1.34±0.83% 의 값이 도출되었다. 제안된 반자동화된 흉강 영상 분할 방법은 갈비뼈와 흉강벽, 횡경막, 그리고 심장 등의 여러 기관을 분할 방식을 기반으로 수행되고, 이는 임상적인 목적에서 높은 정확성과 유용성을 보여 주었다.

두번째 연구는 폐의 동맥 정맥 분리를 위해서 폐의 혈관을 부분혈관으로 자르는 방법을 제시하고 있다. 폐 동맥 정맥 분리의 경우에, 폐 암 수술 시뮬레이션 시의 기초자료로 쓰일 수 있다. 의료진이 머리 속으로 분리를 하거나 수작업으로 분리를 할 수 있으나, 자동화된 방법을 사용하는 것이 더 향상된 방법이다. 기존 방법의 경우에 수동으로 폐 혈관 뿌리쪽을 2D 슬라이스를 기반하여 혈관을 하나씩 따라가며 30~40 점을 찍어주는 과정이 필요하다. 그리고 이를 실행하는데 1 시간 30 분 정도의 시간이 필요하다. 특징값의 최적화 후에, 자동화된 동맥 정맥 분리 정확도는 정답과 비교했을 때 89.71±3.76%이었다. 이 분리 알고리즘은 폐 동맥 정맥의 자동화된 분류를 위해서 미래에 임상적으로 유용하게 사용될 수 있을 것이다.

---

**주요어 : 만성 폐색성 폐질환,컴퓨터 단층 촬영, 다기관 영상분할, 흉곽, 폐 동맥 정맥 분리, 이단계 최소신장트리 구축**

**학 번 : 2010-30263**